

**JPRS-CST-84-025**

**10 September 1984**

# **China Report**

**SCIENCE AND TECHNOLOGY**

**FBIS** FOREIGN BROADCAST INFORMATION SERVICE

RADIOGRAPHIC INSPECTION OF BUTT WELDS DESCRIBED

Shanghai WUSUN JIANCE [NONDESTRUCTIVE TESTING] in Chinese No 2, 1984 pp 16-19

[Article by Zhang Junzhe [1728 0193 0772]: "Radiographic Inspection of Butt Welds in Small Spherical Thick-Wall Vessels"]

[Text] Introduction

Fig. 1 shows a small spherical thick-wall vessel with 100-200 mm outer diameter and 6-10 mm wall thickness; it is made of 1Cr18Ni9Ti austenitic stainless steel, and is constructed by welding together two forged hemispherical shells. It is difficult to use ultrasonic techniques to inspect the welds because signals from material defects cannot be identified due to interference of reflected waves from coarse crystals and stop joints. Therefore, radiographic techniques with sensitivity no less than 2 percent must be used.

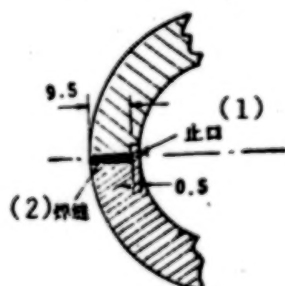


Fig. 1 Schematic Diagram of the Butt Weld and Stop Joint of a Small Spherical Thick-Wall Vessel

KEY: (1) Stop joint  
(2) Butt weld

Clearly, to apply X-ray inspection for this type of butt welds, only the double-wall transillumination, double-image technique can be used. But the image quality is affected by the curvature and wall thickness of the inspected object and the scattered rays. Therefore, to achieve satisfactory results, it is necessary to give careful consideration to the selection of focal

distance, angle of incidence, radiation hardness, intensifying screen and film; it is also necessary to take appropriate measures to improve the shield for scattered radiation and the design of penetrometer.

### Selection of Focal Distance

In general, to obtain sharp images require the focal distance to be as large as possible. Also, due to the conical scattering pattern and continuous spectrum of X-rays and the effect of curvature and wall thickness of the inspected object, the penetration distance and surface intensity of the X-rays will vary from one part of the object to another. In Fig. 2, if  $f_1 > f_2$ , then  $t_2 > t_1 > t$ ; let  $k$  denote the thickness ratio,  $k_1 = t_1/t$ ,  $k_2 = t_2/t$ , then  $k_1 < k_2$ . From the law of X-ray attenuation  $I = I_0 \exp(-\mu t)$ , and the fact that  $t < t_1 < t_2$ , it follows that  $I > I_1 > I_2$ . This effect is even more pronounced under the condition of double-wall transillumination. It can be seen that the thickness ratio  $k$  decreases with increasing focal distance, which ensures the uniformity of film blackness and the sensitivity of detecting defects along the edges of the inspected object. From this point of view, the focal distance clearly should as large as possible.

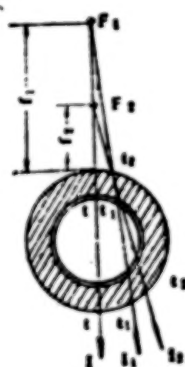


Fig. 2 Comparison of Focal Distances

However, with larger focal distance, the tube voltage and exposure time must be increased in order to ensure sufficient amount of light exposure; as a result, the degree of foginess will increase and the degree of contrast will decrease. In addition, the increase in scattered rays caused by higher tube voltage will have a serious effect on the clarity of image. If the tube voltage remains unchanged while the focal distance is increased, then the exposure time must be increased significantly to achieve the same amount of exposure, again resulting in increased scattered rays and reduced clarity.<sup>[1]</sup> Test results showed that in order to meet the technical requirements of geometric lack of clarity, the focal distance should be as small as possible. The focal distance selected for our application was 1 meter.

### X-Ray Angle of Incidence

In applying the double-wall transillumination technique to inspect the butt welds of spherical thick-wall vessel, the beam center of the X-ray should be offset from the plane of the butt weld in order to achieve a small-opening elliptical image of the butt weld. For a small-diameter, thick-wall vessel, the upper layer of the butt weld image cannot satisfy the sensitivity requirement; only the lower layer can be diagnosed. The X-ray angle of incidence should be determined such that the upper and lower images are as close to each other as possible without overlapping in order to avoid overamplification of the images of the lower butt weld and the defects, and possible mis-inspection due to the low degree of contrast.

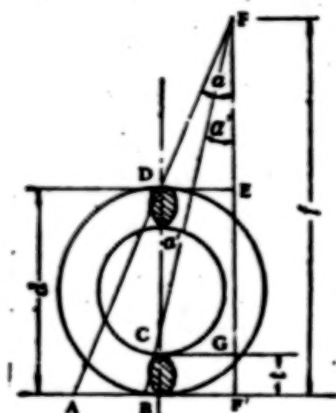


Fig. 3 Selection of Angle of Incidence

In Fig. 3, the outer diameter of the vessel is denoted by  $d$ ,  $F$  is the focal point,  $f$  is the focal distance,  $t$  is the wall thickness, and  $\alpha$  is the angle of incidence. The ray is projected from the focal point  $F$  to the center of the butt weld, through two layers of wall and onto the film at point  $A$ ; the base of the lower butt weld surface is projected onto the point  $B$ , whose angle of incidence is  $\alpha'$ . Then, in  $\triangle FAF'$  and  $\triangle FBF'$ :<sup>[3]</sup>

$$\begin{aligned} AF' &= f \cdot \tan \alpha \\ BF' &= f \cdot \tan \alpha' \\ \therefore AB &= f(\tan \alpha - \tan \alpha') \end{aligned} \quad (1)$$

In  $\triangle FDC$ ,  $\angle FCD = \alpha'$ ,  $\angle FDC = 180^\circ - \alpha$ .

$$FD = \frac{f-d}{\cos \alpha}, \quad FC = \frac{f-t}{\cos \alpha'}$$



From the law of sines:

$$\begin{aligned} \frac{FD}{\sin \alpha'} &= \frac{FC}{\sin(180^\circ - \alpha)} \\ \text{i.e.,} \quad \frac{(f-d)/\cos \alpha}{\sin \alpha'} &= \frac{(f-t)/\cos \alpha'}{\sin(180^\circ - \alpha)} \\ \therefore \frac{(f-d)/\cos \alpha}{\sin \alpha'} &= \frac{(f-t)/\cos \alpha'}{\sin \alpha} \end{aligned}$$

then,

$$\begin{aligned} \tan \alpha (f-d) &= \tan \alpha' (f-t) \\ \therefore \tan \alpha' &= \frac{f-d}{f-t} \cdot \tan \alpha \end{aligned} \quad (2)$$

By substituting equation (2) into (1), one obtains the following:

$$\begin{aligned} AB &= f \left( \tan \alpha - \frac{f-d}{f-t} \cdot \tan \alpha \right) = \tan \alpha \cdot f \left( \frac{d-t}{f-t} \right) \\ \therefore \tan \alpha &= \frac{AB(f-t)}{f(d-t)} \\ \alpha_{\max} &\leq \tan^{-1} \left[ \frac{AB(f-t)}{f(d-t)} \right] \end{aligned} \quad (3)$$

In equation (3), AB is the elliptical opening of the X-ray image center of the butt weld, which can be determined from the required width of the image; the value of  $\alpha$  then can be determined accordingly. For example, suppose  $AB=20$  mm for a vessel with  $d=200$  mm,  $t=10$  mm, and  $f=1000$  mm, then  $\alpha$  is calculated to be  $\leq 6^\circ$ ; if  $AB=30$  mm, then  $\alpha \leq 9^\circ$ ; if  $AB=40$  mm, then  $\alpha = 12^\circ$ . For a vessel with  $d=100$  mm,  $t=10$  mm, and assume  $AB=20$  mm, then  $\alpha \leq 12^\circ$ ; if  $AB=30$  mm, then  $\alpha \leq 18^\circ$ . In actual inspection, the angle of incidence for a 200 mm-diameter vessel is chosen to be around  $10^\circ$ ; for a 100 mm-diameter vessel, the angle of incidence is chosen to be around  $15^\circ$ .

#### Radiation Hardness, Film and Intensifying Screen

For a given focal distance and rated tube current, the exposure condition is determined by the tube voltage and exposure time. By selecting a relatively low tube voltage, the average wavelength of X-ray is longer, or the radiation quality is said to be softer. As a result, the attenuation of rays through the material is more pronounced, thus increasing the contrast ratio and improving the sharpness of X-ray photography. The attenuation coefficient is given by  $\mu \approx C Z^3 \lambda^3$  ( $Z$  is the atomic coefficient of the material,  $\lambda$  is the wavelength of the incident ray,  $C$  is the speed of light); thus, the longer the wavelength, the larger  $\mu$  becomes, the better the contrast ratio and the higher the sensitivity in revealing material defects. Conversely, if a higher voltage is used, the X-ray generated will be harder, and the contrast ratio will be reduced; as a result, level of scattered rays will increase, and the quality of X-ray photography will be adversely affected. In applying the

technique of double-wall transillumination to inspect thick-wall vessels, if the tube voltage is too low, the exposure time becomes excessive, and penetration may be impossible. Therefore, in selecting radiation hardness, we must first ensure penetration (at the thickest part of transillumination) and select as low a tube voltage as possible without excessive exposure time. Test results showed that when using the Model 2515 X-ray inspection unit on a vessel with 6 mm wall thickness (i.e., penetrating a double wall thickness of 12 mm), satisfactory transillumination results were obtained by selecting the tube voltage to be 180 KVP, the tube current to be 18 mA, and the exposure time to be 4 minutes; for a 10 mm-thick vessel (penetrating a double wall thickness of 20 mm), a tube voltage of 200 KVP, tube current of 18 mA and exposure time of 5 minutes were selected.

Under the condition of the focal distance and exposure time as indicated above, penetration can only be achieved by using an intensifying screen. While fluorescent intensifying screen would allow penetration, the resulting image quality was so poor that diagnosis of the negative may not be possible. Later, satisfactory results were obtained by using 0.1 mm lead-foil intensifying screens (the front and back screens had the same thickness). Such screens not only provided intensification and reduced exposure time, they could also absorb scattered rays to improve the clarity of the negatives.

Test results also showed that even with lead-foil intensifying screens, the contrast ratio and clarity of certain films were still very poor. To achieve satisfactory results, we used the Belgium Gevoert D4 type film, which was a medium-speed film with high contrast ratio and very fine particles. The higher speed Gevoert D7 film was also satisfactory.

#### Shielding of Scattered Rays

Although we took various technical measures such as careful selection of the technical parameters, and the use of lead-foil intensifying screens and D4 type films, it is still difficult to obtain high-quality X-ray pictures without taking special measures in shielding the scattered rays. A small spherical thick-wall vessel is different from ordinary small-diameter thick tubes. Since the film cannot be bent into a sphere, the contact surface between the lower butt weld of the vessel and the film is very small. On the other hand, the effective region of the image obtained from transillumination must have a finite length; also, due to the large double-wall transillumination thickness, the high tube voltage, and the long exposure time, scattered rays pose a serious problem and must be carefully shielded.

To achieve more effective shielding, we took the following measures: (1) we used a lead-foil intensifying screen to absorb a large amount of scattered rays during the period of exposure; (2) we used a large 5 mm-thick lead-foil screen backing to absorb scattered rays arriving from the rear; (3) we built a special frame to perform shielded photography, as shown in Fig. 4. The thickness of the shield plate was 5 mm, and the opening at the bottom was used for inserting and retrieving the negatives. It is our experience that the shielding of scattered rays is the most important factor in X-ray transillumination of butt welds of small spherical thick-wall vessel.

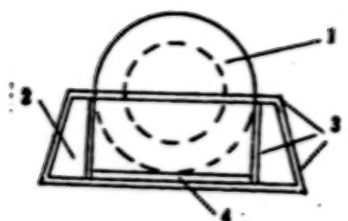


Fig. 4 Frame for Shielded Photography

KEY: (1) Vessel  
(2) Wooden box  
(3) Lead plate  
(4) Negative

#### Control of Effective Range of Transillumination and the Segmented Measurement Method

It has been pointed out in the discussion of focal distance selection that the blackness and sensitivity requirements of the midsection and boundary of the negative can be satisfied only by appropriately controlling the thickness ratio  $k$  (in the case of a flat plate, the effect of  $k$  can be ignored). Based on production experience and technical requirements on the blackness of negatives to comply with radiographic inspection standards for butt welds, we have specified a standard blackness value of  $D=1.5$  (as measured by the MDX-2 black and white densitometer). Within the effective region of X-ray exposure, the blackness of negatives decreases uniformly from the center of the ray toward the two edges; when the difference in blackness reaches  $\Delta D=0.5-0.6$ , calculations using the steel-wire penetrometer (the XZQ-1 image quality indicator) show that the ray center and the edges have the same sensitivity level. It is pointed out in Ref. 2 that for materials with transillumination thickness of less than 20 mm, an appropriate value for the thickness ratio  $k$  is 1.25. Ref. 3 presents a method of calculating the length of the effective transillumination range (Fig. 5). Suppose the diameter of the vessel is  $d$ , the wall thickness is  $t$ , and the controlled thickness ratio is  $k=1.1$ , then the length  $AB$  in the figure is  $AB=1.1t$ .  $\alpha$  is the angle of the incident ray.

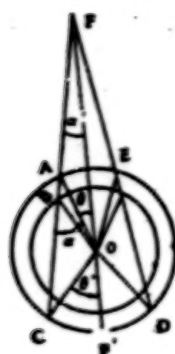


Fig. 5 Control of Effective Transillumination Range

In  $\triangle ABO$ ,  $OA=R=d/2$ ,  $OB=R-t$ ,  $AB=1.1t$ .

From the law of cosines

$$\begin{aligned} OB^2 &= OA^2 + AB^2 - 2AB \cdot OA \cdot \cos \alpha \\ \therefore (R-t)^2 &= R^2 + (1.1t)^2 - 2.2Rt \cos \alpha \end{aligned}$$

or

$$\begin{aligned} \cos \alpha &= (d + 0.21t) / 1.1d \\ \therefore \alpha &= \cos^{-1}[(d + 0.21t) / 1.1d] \end{aligned} \quad (4)$$

Also, in  $\triangle FAO$ ,

$$\begin{aligned} \therefore \alpha &= \alpha' + \theta \\ \therefore \theta &= \alpha - \alpha' \\ \therefore \angle ACO &= \angle BAO = \alpha \\ \therefore \theta' &= \alpha + \alpha' \\ \therefore \angle AFO &= \angle OFB = \alpha', \\ \angle F'OD &= \angle F'OC = \theta' \\ \therefore 2(\theta + \theta') &= 4\alpha \end{aligned} \quad (5)$$

The length of the effective transillumination range  $L$  is equal to twice the arc lengths corresponding to the central angles  $\theta$  and  $\theta'$ . Thus,

$$L = \pi d \cdot 4\alpha / 360^\circ \quad (6)$$

Substituting equation (4) into (6) gives

$$L = \pi d [\cos^{-1}(d + 0.21t) / 1.1d] \cdot (90^\circ)^{-1} \quad (7)$$

By the same token, when the controlled thickness ratio is  $k=1.2$ , then

$$L = \pi d [\cos^{-1}(d + 0.44t) / 1.2d] \cdot (\pi/90)^{-1} \quad (8)$$

If the total length of the butt weld is  $C = \pi d$ , and  $k=1.2$ , then for a vessel with  $d=200$  mm,  $t=10$  mm, the number of transilluminations can be calculated from equation (8) to be  $n=3$ , which ensures that there is certain amount of overlap at the joints. Under the same conditions, for a vessel with  $d=100$  mm,  $t=10$  mm,  $n$  is calculated to be 4.

For a vessel with small outer diameter and large wall thickness, even though the calculated number of transilluminations is still accurate, the image of the upper butt weld may not be able to meet sensitivity requirements because it is too far from the negative. In this case, the segmented measurement method must be used.

The so-called segmented measurement method consists of building a penetrometer which meets the 2 percent sensitivity requirement; it is constructed using 11 stainless steel wires which are 20 mm long and separated by 5 mm, and it is covered with foam rubber to allow easy bending. After normal exposure and dark room processing, one can calculate the length of each transillumination  $L$  and the number of transilluminations  $n = \frac{\pi C}{L}$  by measuring the distance between the metal wires at the farthest edge of the negative. In order to accommodate vessels of different thicknesses, several sets of penetrometers were constructed using wire sizes ranging from  $\phi 0.1-0.4$  mm. The penetrometers can be attached using adhesive paper. They should be attached to both the upper and lower butt welds to provide close monitoring of transillumination sensitivity. For a vessel with  $d=200$  mm,  $t=10$  mm as in the above example, the segmented method of measurement requires  $n=3$  to achieve 100 percent transillumination; for a vessel with  $d=100$  mm,  $t=10$  mm, it requires  $n=5$  to achieve 100 percent effective inspection and to ensure certain amount of overlap at the joints of the negatives. This result illustrates that the segmented measurement method is basically consistent with the calculation method. If the image of the upper butt weld cannot meet sensitivity requirement, one should use the result of the segmented measurement method.

Fig. 6 and Fig. 7 show the elliptical images of the butt welds of two vessels with different wall thicknesses. It can be seen from Fig. 7 that the butt weld has two chain-shaped air bubbles.

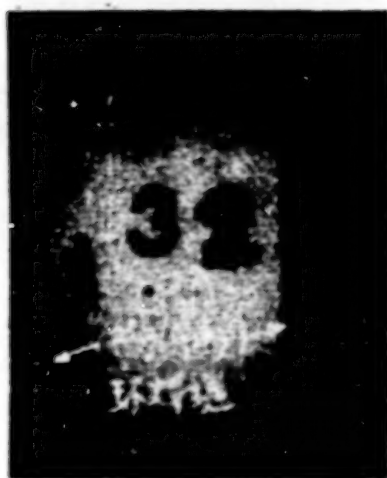


Fig. 6 Elliptical Image of the Butt Weld

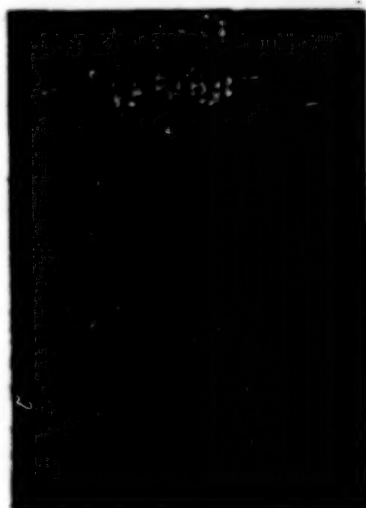


Fig. 7 Chain-Shaped Air Bubbles

Recently, we performed an experiment of inspecting the butt welds of a small spherical thick-wall vessel with the model XY-1520 X-ray machine. This machine was assembled by the Dandong Instrument Factory using the MCN161 beryllium window metal-ceramic tubes produced by the Philips Co of Holland. The experiment was conducted under the condition where the film, the intensifying screen and the X-ray angle of incidence remained unchanged. Because of the small size of the focal point of this device (typical focal point is  $3 \times 3 \text{ mm}^2$ ), it follows from the formula of geometric unclarity:  $U_g = t \cdot F / f$  ( $U_g$  is the geometric half image,  $t$  is the thickness of the article,  $F$  is the dimension of the focal point, and  $f$  is the focal distance) that when  $F$  is reduced, the focal distance  $f$  can be reduced accordingly without changing the value of  $U_g$ . The experiment



showed that for a vessel with wall thickness of 10 mm (i.e., penetrating a double wall thickness of 20 mm), tube voltage of 130 KVP, tube current of 20 mA, and focal distance of 600 mm, satisfactory transillumination results were obtained with 6 minutes of exposure time, and the inspection sensitivity was increased to approximately 1.5 percent.

3012

CSO: 4008/314



THERMOPHYSICAL PROPERTIES OF MATTER

Shanghai ZIRAN ZAZHI [NATURE JOURNAL] in Chinese No 1, 1984 pp 28-29

[Excerpt] Research on thermophysical properties in China began in the mid-1950's when room temperature thermal conductivity measurements were made in universities and research units. In the early 1960's more resources were devoted to large-scale thermophysical properties research. Due to the urgent demands of national economic construction and particularly of defense construction, the State Science and Technology Commission established some research institutes and high temperature measurement bases at participating universities. These organizations planned the research and assigned research tasks on thermophysical measurements. Scientific research resources in China were organized and measurement methods and facilities for thermal conductivity and specific heat were established for different temperature ranges. The first high temperature annual symposium was held in 1961 and made a good start for China's thermophysical properties study. In the past 20 years China has made considerable progress in thermophysical research and has formed a science and technology rank of substantial quantity and quality. One important goal was to satisfy the timely needs of thermophysical properties data and testing techniques in China's aviation, aerospace and nuclear technology development.

On the whole, however, there is still a considerable gap between China's thermophysical research level and the international standard. Many weak links need to be strengthened and many voids need to be filled. In the author's opinion, we should pay attention to problems in the following six areas:

1. In contrast to the testing technology of thermophysical properties, the breadth and depth of the research on thermophysical mechanism, variation and parameters are relatively weak. This has not only impeded the in-depth development of the thermophysical properties science but also the progress of other scientific disciplines.
2. In contrast to the thermophysical testing methods and devices for solid matter, the study of fluid media is weak and the study of the thermophysical properties of gases is almost nonexistent.

3. In contrast to the conventional or specialized measurement techniques, the serialization and particularly the standardization (including standard samples) of thermophysical measurement techniques and equipment are still in the development or planning stages. Although tentative ministry-level standards for certain thermophysical measurements have been established, a national standard has not. As a result, the thermophysical properties data in China (especially for thermal conductivity) vary from research unit to research unit and sometimes with large discrepancies.

4. Although the research units in China have accumulated a great amount of thermophysical properties data on Chinese-made materials, China still does not have her own thermophysical properties handbook encompassing all the solid materials. (The responsible unit is in the process of compiling a thermophysical properties handbook for metallic materials.) Although a thermophysical properties data center and a data bank are being established, the amount of manpower and material resources devoted to this task is inadequate and cannot quickly satisfy the urgent need.

5. If thermophysical properties research in the past is considered closely tied to the development of defense and frontier science and technology, then we still need to strengthen the connection between energy technology and other industrial departments. For example, the development and production of heat insulation material for energy conservation basically was not guided by the principles of thermal insulation and thermal design, and neither were the application parameters optimized by thermophysical properties principles.

6. We must create a conducive environment and actively establish China's research center for thermophysical parameters. China's research and application of thermophysical properties must be promoted on two fronts: experimental study based on scientific theories and measurement techniques.

9698

CSO: 4008/175

PILOT MODEL TEST FOR BITUMINIZATION OF CONCENTRATED RADIOACTIVE WASTES USING CONTINUOUS TURBULENT FILM EVAPORATOR

Beijing HE KEXUE YU GONGCHENG [CHINESE JOURNAL OF NUCLEAR SCIENCE AND ENGINEERING] in Chinese Vol 3, No 2, Jun 83 pp 142-152

[Article by Li Dongcai [2621, 2767, 2088] of Beijing Institute of Nuclear Reactor Engineering: "An Expanded Cold Pilot-Model Test for Bituminization of Concentrated Radioactive Liquid Wastes Using Turbulent Film Evaporator"; manuscript received 14 July 1982]

[Text] Abstract

The emphasis of the paper was placed on the introduction to the selection of technological parameters in the bituminization process using continuous turbulent film evaporators, the verification experiments on various medium and low level radioactive cold model waste liquids, the test of the flow process and the equipment during continuous operation, the decontamination method of the bituminization equipment and recovery of the decontaminant, and the measurement of thermal stabilities of various bituminized wastes, etc.

I. Introduction

China began the technological study of bituminization of radioactive liquid wastes from 1969; starting with small-scale hot and cold tests as well as some basic research. Expanded cold model tests for bituminization of low and medium level radioactive concentrated liquid wastes using continuous turbulent film evaporators began in 1975. The accomplishments of research have already been applied to engineering constructions.

II. Brief Introduction to Technological Process and Equipment

2.1 Brief Introduction to Technological Process

See Figure 1. A 200l barrel of No 60 asphalt is heated to melt in a furnace (at temperatures above 100°C). It is then dehydrated by flowing through a dehydration tank (temperatures around 130°C). The impurities in the asphalt

- 0- Liquid level indicator  
 0+ Resistance thermometer  
 Vacuum gauge  
 Rotameter  
 Glass thermometer  
 Glass liquid level indicator  
 Steam trap  
 1 Pipe filter  
 2 Asphalt gear pump

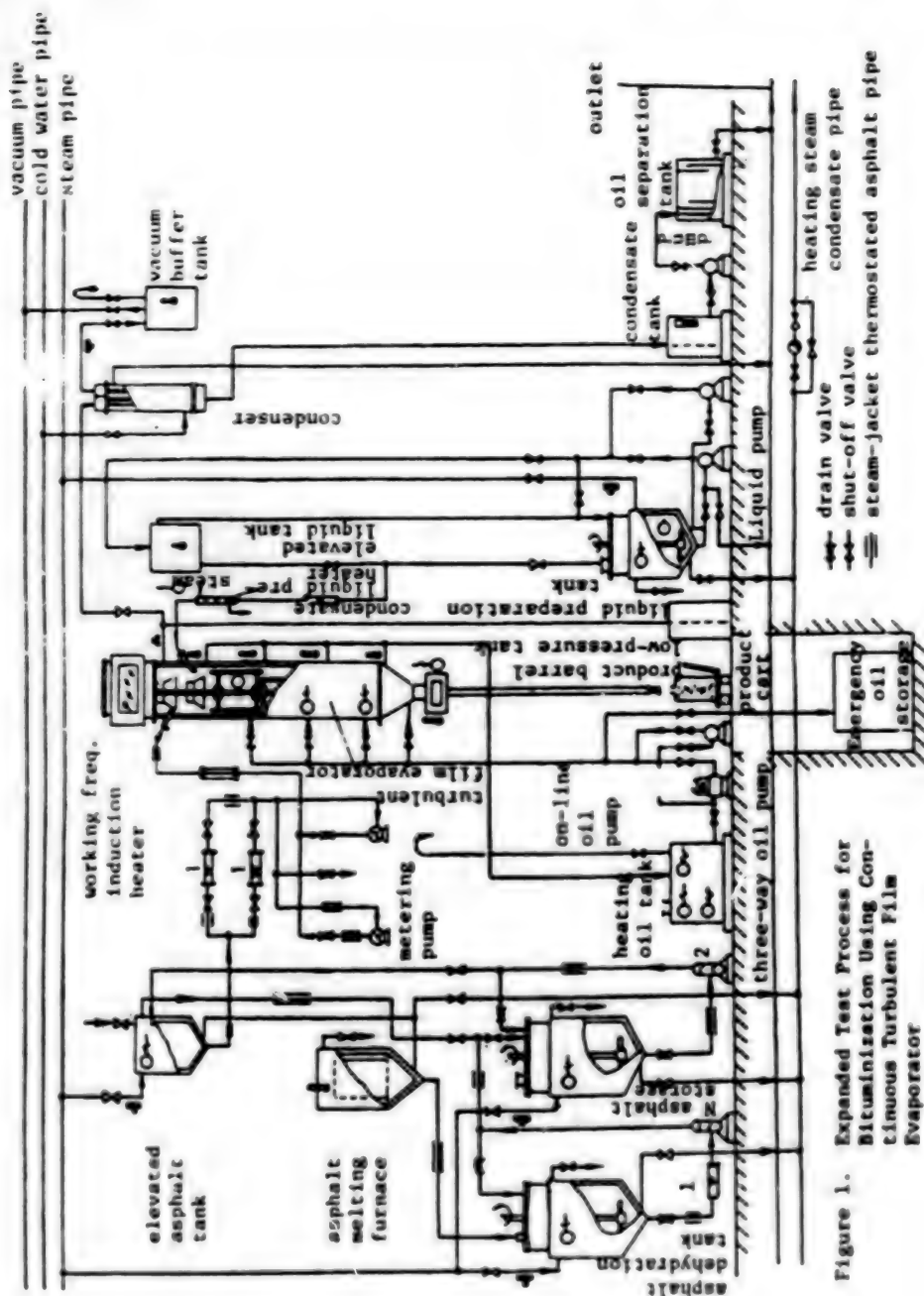


Figure 1. Expanded Test Process for Bituminization Using Continuous Turbulent Film Evaporator

are removed by a filter, and it is sent into an asphalt storage tank by a pump. The asphalt is again delivered by another pump to an elevated asphalt tank for use. When this material is fed, another filter is used to further remove the impurities. It is delivered at a fixed rate by a metering pump to an induction heater to be rapidly heated to 170-180°C. Then it flows into the distribution plate of the turbulent film evaporator. The solution is prepared in the solution preparation tank and then delivered to an elevated tank for use by a pump. Through a flowmeter, this liquid enters a pre-heater to be heated to around 95°C. Then, it enters the lower distribution plate of the turbulent evaporator.

The turbulent evaporator is pre-heated to 100°C before the scraper motor can be turned on and the rotating speed is adjusted to the specific value. Only when the wall temperature of the turbulent evaporator reaches above 200°C, then the test liquid can be added. Asphalt is first added for over 5 minutes, then the test liquid is delivered. When stopping, the liquid is stopped first before asphalt is turned off to prevent scab formation on the wall surface. When the scraper is operating, asphalt is thrown to the heated wall of the turbulent evaporator from the distribution plate by centrifugal force. A thin film less than 1.5 mm thick with a continuously renewed surface is formed by the rotating scraper. When liquid is added, it is thrown from the lower distribution plate to the asphalt film, and is thoroughly mixed with the asphalt by the vigorous stirring of the rotating scraper. The film is continuously renewed and the liquid is dehydrated by absorbing the required heat of vaporization from the heated surface. The mixture moves towards the outlet on the surface of the evaporator in a spiral by gravity. As it reaches the outlet, it becomes a qualified bituminized product. The product can flow away by itself, or it can be delivered continuously under a sealed atmosphere by a triple element rotor pump (process not shown) to ensure the continuous operation of the evaporator at a certain negative pressure.

The secondary steam generated in the turbulent evaporator is cooled to 20-30°C by a condenser. It flows automatically into a condensate tank (maintaining a 7m water column seal). Periodically, the condensate, which contains a minute amount of oil, is delivered to an oil separation tank by a water pump to remove the oil. It is then discharged into the sewer system. The turbulent evaporator is heated by using over heated No 38 engine oil. The oil is heated by 40 kW electric heating element in the heating tank. Heated oil is used to heat up the turbulent evaporator by circulating with an on-line oil pump and a three-way oil pump. The heating temperature is around 200-230°C.

## 2.2 Brief Introduction to Turbulent Evaporator

Look at Figure 2. Turbulent evaporators are suited for continuously concentrating high viscosity, heat sensitive, and easily foaming matters. Furthermore, the heat transfer efficiency is relatively high, and the duration of stay for the materials in the equipment is only a few minutes. It is appropriate to be used to treat highly viscous and heat sensitive bituminized wastes. The following problems should be noticed in the design:

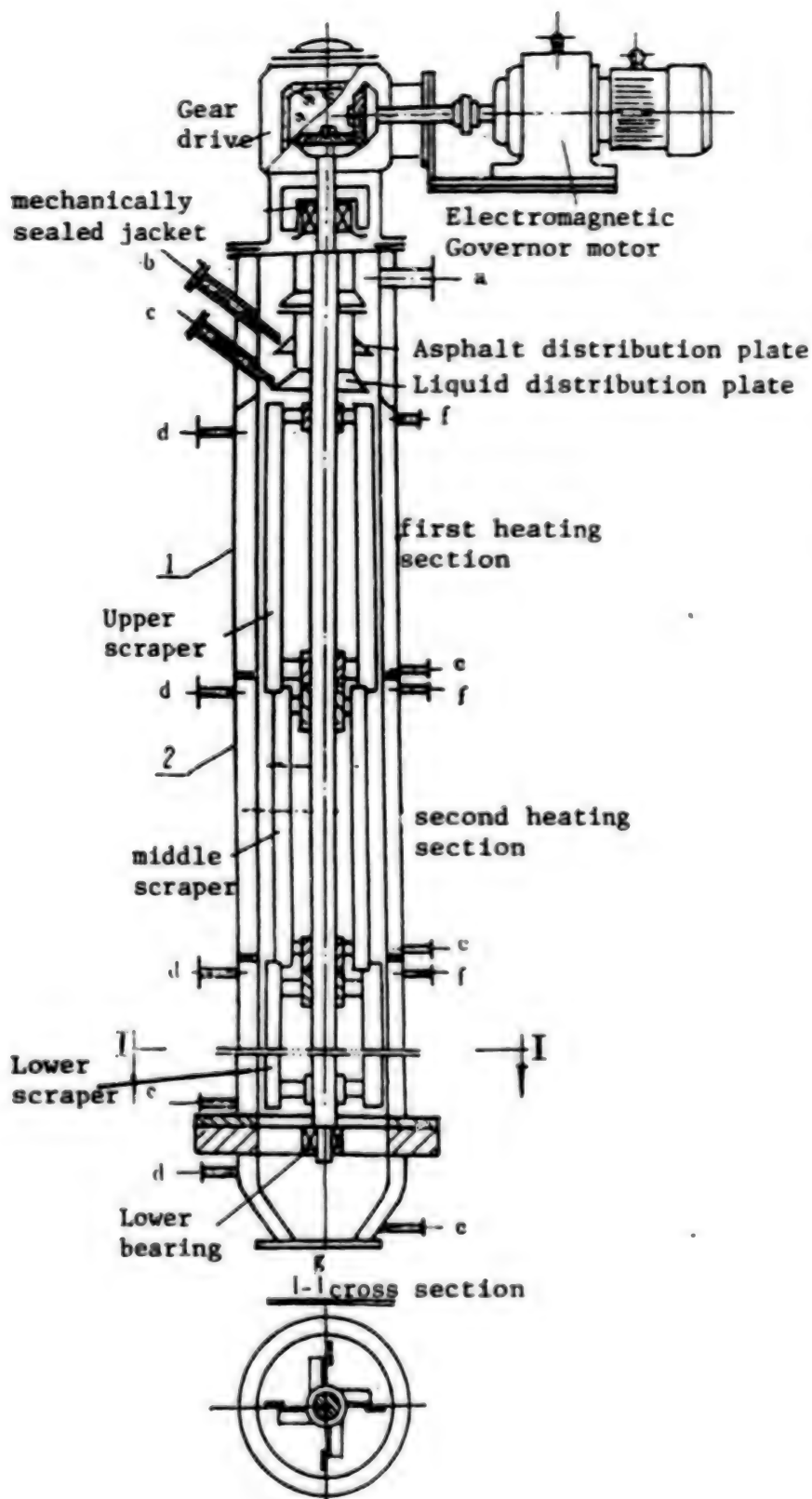


Figure 2.

Schematic Diagram of the Structure of the Turbulent Film Evaporator

- a. secondary steam outlet
- b. asphalt inlet
- c. liquid inlet
- d. oil outlet (or steam inlet)
- e. oil inlet (or cooling water outlet)
- f. uncondensed gas exhaust
- g. bituminized product outlet



1. Select a suitable aspect ratio (usually 4-6). The longer the axle is, the higher the strength requirement becomes. Requirements in material selection, processing and surface heat treatment are also more complicated. A small value should be adopted in the design, to the extent possible.
2. It is required that the scraper axle have high strength and small deformation. The surface must be heat treated in nitrogen. It must qualify both the static and dynamic tests.
3. The product outlet must be placed properly to prevent blockage. This modified turbulent evaporator (i.e., as shown in Figure 2) was stable and reliable after placed in operation. Furthermore, it had been tested under special environmental conditions.

### III. Types of Bituminized Wastes

No 60 asphalt from Nanjing Refinery was selected for use in the experiment. The types and major compositions of liquid wastes studied experimentally are shown in Table 1.

### IV. Discussion of Experimental Results

#### 4.1 Selection of Operating Parameters of Turbulent Evaporator

##### 1. Optimum Salt Content of Bituminized Material

It was proven experimentally that the optimum salt content is 40-50 percent (wt). The experimental data is shown in Table 2.

##### 2. Allowable Range of Scraper Rotating Speed

Experimental results showed that the product was mixed homogeneously at a high rotating speed. Dehydration was thorough and leaching rate was low. However, an excessively high speed can easily cause vibration of the scraper, increasing power consumption, and accelerate the wearing and tearing of the bearing. At a low speed, however, the tendency of poor dehydration increases.

##### 3. Degree of Vacuum in Turbulent Evaporator

Experiments showed that dehydration capability was low at the normal pressure, and the water content in the product was high. It is appropriate that the vacuum is not less than 50 Torr, as shown in Table 3. From the table one knows that the higher the vacuum is, the larger the amount of salts and oil in the secondary steam will remain; which lowers the purification coefficient. Therefore, a suitable vacuum must be selected for the operation.

##### 4. Product Temperature

When the product temperature is too low, the water content is too high, leaching rate is large, and fluidity is so poor that the exit may be clogged. When the product temperature is too high, energy consumption is increased.



Table 1. Chemical Compositions of Cold Model Liquid Wastes and Types of Waste Water

Liquid Number	Major Composition*	Waste Water Type
1.	30-34% (wt) $\text{NaNO}_3$ , pH = 10 - 13, salt content about 463 (prepared with industrially pure $\text{NaNO}_3$ ).	low-level radioactive waste water
2.	$\text{NaCO}_3$ : 5.25, $\text{Na}_2\text{C}_2\text{O}_4$ : 13.5, $\text{NaOH}$ : 3.38 $\text{NaNO}_3$ : 43.27, $\text{Na}_2\text{SO}_4$ : 10.5, $\text{Mg}(\text{OH})_2$ : 1.78, $\text{Ca}_3(\text{PO}_4)_2$ : 2.35, $\text{CaCO}_3$ : 11.1, petroleum sulfonic acid: 7.5, detergent: 2.3, defoaming agent (dipropanol butyl ethyl epoxy ester) = 10, and others 15. Mixture salt content at about 120, pH adjusted to 10-13.	low-level radioactive waste water (1:1 mixture of floor washing water and waste laundry water).
3.	Chemical slurry crudely prepared in a rapid settling vessel by adding reagents such as $\text{Fe}_2(\text{SO}_4)_3$ , $\text{Na}_3\text{PO}_4$ , $\text{NaOH}$ , $\text{KMnO}_4$ , $(\text{NaPO}_4)_6$ , etc into waste water No 2, total salt 20-30, total salt in concentrated slurry after freeze-pump-thaw filtering around 100, pH adjusted to = 10-13.	low-level radioactive chemical slurry
4.	$\text{NaNO}_3$ : 314, $\text{KNO}_3$ : 0.103, $\text{Fe}_2(\text{SO}_4)_3$ : 32, $\text{Nn}(\text{NO}_3)_2$ : 0.154, $\text{NHO}_3$ : 63, using $\text{NaOH}$ to adjust pH = 12, salt content in waste water around 430.	acidic medium level radioactive waste water
5.	$\text{NaAlO}_2$ : 82, $\text{NaNO}_3$ : 61.5, $\text{NaOH}$ : 31.5, $\text{Na}_2\text{O}_3$ : 0.9, waste water salt content about 235, actually measured alkalinity 2.3N.	medium-level radioactive waste liquid discharged from the shell
6.	Mixing 1# + 3#, volume ratio 1#:3# = 1:0.635 (chemical slurry with salt content 26.5), mixture liquid salt content around 337, pH adjusted to = 10-13.	low-level mixed waste water
7.	Mixing 1# + 3#, volume ratio 1#:3# = 1:0.21 (freeze-pump-thaw filtered slurry), liquid mixture salt content around 285, pH adjusted to $\approx$ 13.	low-level radioactive mixed waste water

Table 1. Continued

8.	Mixing 1# + 2#, volume ratio 1#:2# = 1:0.25 (1# salt content 450, 2# 120), mixture salt content about 380, pH adjusted to = 10-13.	low-level radioactive mixed waste water
9.	Mixing 1# + 2# + 3#, volume ratio 1#:2#:3# = 1.0:0.41 : 0.9 (1# salt content 300, 2# 120, and 3# 30), liquid mixture salt content about 145, pH adjusted to = 10-13.	low-level radioactive waste water mixed with reagents
10.	Mixing 4# + 5# + 1# (i.e., absorbed acidic and basic waste water): volume ratio 4#:5#:1# = 0.4:1:3.6 (4# salt content 422, 5# 322, and 1# 520), mixed waste water salt content 480, pH adjusted to = 10-13.	medium-level radioactive waste water mixed with reagents
11.	Mixing 17# + 4# + 1# (basic waste water neutralizing agent): volume ratio 17#:4#:1# = 1:0.255:2.3, mixed waste water salt content 480, pH adjusted to = 10-13.	medium-level radioactive waste water mixed with reagents
12.	Mixing absorbing solutions: acidic absorbing solution-citric acid 2%(wt), ammonium citrate 5%(wt), EDTA 0.5%(wt), water 92.5%(wt). Basic absorbing solution - NaOH 10%(wt), $KMnO_4$ 3%(wt), water 87%(wt). Mixing volume ratio 1:1, concentrated one time by distillation, liquid mixture salt content about 256, pH adjusted to = 9.24.	low-level radioactive mixed waste water
13.	12# = boron containing waste water (mixing $H_3BO_3$ :316 with NaOH:203), volume ratio 1:1, liquid mixture salt content about 540, pH adjusted to = 13.	low-level radioactive waste mixed with reagents
14.	Nitric acid waste water: $Mg(NO_3)_2$ :247, $Ca(NO_3)_2$ :45, $Ba(NO_3)_2$ :9.5, $HNO_3$ 13Bm after oC adhysted ti = 9- 11, liquid mixture salt content around 500.	low-level radioactive waste water

Table 1. continued

15.	Mixed acid waste water: $\text{HNO}_3$ :11N, $\text{HCl}$ :5N, pH adjusted to = 11.6, waste water salt content about 446	low-level radioactive waste water
16.	14# + 15# + chemical slurry ( $\text{Fe}_2(\text{SO}_4)_3$ : 0.8, $\text{KMnO}_4$ :0.4, using NaOH to adjust pH to = 9-11, slurry salt content about 23), volume ratio:14#:15#:chemical slurry = 1:1:4, mixed liquid salt content about 276, pH adjusted to = 9.1.	low-level radioactive waste mixed with reagents
17.	$\text{NaAlO}_2$ + $\text{Na}_2\text{CO}_3$ waste water: $\text{NaAlO}_2$ :193.7, $\text{NaOH}$ :146, $\text{Na}_2\text{CO}_3$ :85.6, pH adjusted to = 10-13, total salt 480.	medium-level radioactive mixed waste water

\*Unit of salt concentration is g/l.

(1) 固相化物平均含盐率 (%wt)	(2) 平均浸出率* (1-16天对 $\text{Na}^+$ ) (g/cm <sup>2</sup> ·d)	(3) 沥青固化物软化点 (°C)	(4) 沥青固化物平均含水量 (%wt)	(5) 备 注
44.80	$0.88 \times 10^{-4}$	63.7	0.20	(6) 产品流动性好, 表面光亮, 盐份分布均匀, 蒸发器运行平稳, 出料通畅。
48.50	$1.18 \times 10^{-4}$	68.8	0.63	
50.70	$1.16 \times 10^{-4}$	69.3	0.28	
55.85	$4.00 \times 10^{-4}$	71.4	1.40	(7) 产品流动性差, 表面粗糙, 盐粉分布不均, 蒸发器壁面有时结疤, 出料口堵塞及刮板短时震动。
57.80	$4.65 \times 10^{-4}$	78.3	1.03	
58.60	$13.68 \times 10^{-4}$	84.7	0.85	

(8)文中浸出率, 指固化物在蒸馏水中, 静态浸泡1—16天, 每天取样测定 $\text{Na}^+$ 浓度的平均值。

Table 2. Effect of Salt Content in Bituminized Material on Part of the Product Characteristics (No 1 liquid)

- average salt content in bituminized material (% wt)
- average leaching rate\* (1-16 days with respect to  $\text{Na}^+$ ) (g/cm<sup>2</sup>·d)
- softening point of bituminized material (°C)
- average water content in bituminized material (%wt)
- remarks
- good fluidity, shining surface, homogeneous salt distribution, evaporator operating stably, product moving smoothly
- poor fluidity, rough surface, uneven salt distribution, scab formation on evaporator wall surface at times, blockage of product outlet, short-term vibration of scraper

Table 2 continued:

8. \*The leaching rate given in the paper is the average  $\text{Na}^+$  concentration measured during daily sampling when the bituminized material was soaked in distilled water for 1-16 days statically.

(10) 刮板蒸发器真空度 (Torr)	(2) 物料含水量 (%wt)	(3) 平均产品温度 (°C)	(4) 物料液投加量 (l/h)	二次蒸汽冷凝液中 盐、油含量 (5) (6) 盐 (mg/l) (7) 油 (mg/l)		(8) 备注
(10)						(9)
0 (常压)	11.69	130-164	24-27	—	22.0	用1号料液试验
50	0.78	144-172	24	29.2	74.9	
87-120	0.46	140-160	24	31.2	33.6	
150	0.45	138-180	24-30	124.5	62.9	

Table 3. Effect of Vacuum Turbulent Evaporator on Water Content in Products

Key:

1. vacuum in turbulent evaporator (Torr)
2. average water content in bituminized material (%wt)
3. product exit temperature (°C)
4. liquid feeding rate (l/h)
5. salt and oil contained in secondary steam condensate
6. salt (mg/l)
7. oil (mg/l)
8. remarks
9. tested using No 1 liquid
10. normal pressure

It may even cause the dissociation of salts and lead to the danger of explosion. The appropriate product exit temperature is 160-180°C.

#### 5. Optimum Productivity of Turbulent Evaporator

The optimum productivity was obtained under the following conditions: scraper rotating speed 850 rpm, bituminized salt content 45 percent (wt) vacuum 100 Torr, liquid 40 percent  $\text{NaNO}_3$  (pH = 10-13), oil temperature 220-230°C, and water content in bituminized product < 0.5 percent (wt). It was proven experimentally that the optimum productivity of the turbulent evaporator was only 401/m<sup>2</sup>.h when heated with No 38 engine oil.

#### 4.2 Colt Test With Engineering Model Liquid and Evaluation of Continuous Operation of the Process.

Bituminization tests on the 13 waste liquids listed in Table 1 were performed separately in a turbulent evaporator. Qualified products can always be obtained as long as the operating conditions are appropriate, which indicates that a turbulent evaporator is highly adaptable to various types of waste water. Results are shown in Table 4.

No 1 liquid was used in a continuous operation for 180 hr to evaluate the reliability of the technological process. A total of 6500 l of 40 percent  $\text{NaNO}_3$  solution was treated, and 5500 l of bituminized product was obtained. Together with 300 hours of intermittent batch process tests, results indicated that the turbulent evaporator was operating normally without apparent vibration, blockage and scab formation. After the test was completed, it was observed that there was a 0.5-1. mm thick gray bituminized salt scale on the middle and lower portion of the heated wall. Because the scraper gap was 15. mm, therefore, it did not affect the operation (but affected heat transfer). The data is shown in Table 5.

#### 4.3 Decontamination Method of Bituminization

Because a bituminized salt scale will form on the solidifying surface and moving parts of the evaporator, a good decontaminant must be used to wash it away in order to ensure heat transfer and safety. Now, the results of decontamination study are summarized in the following:

1. Selection of Decontaminant. Twelve decontaminants were tested. We recommend the use of industrially pure trichloroethylene as the decontaminant after making our selection.

2. Decontamination of Turbulent Evaporator. A salt scale was first formed by nearly 20 hours of bituminization of No 9, 12, 15, 16 liquids. Trichloroethylene was then added. The decontaminant was drained after 24 hours of static soaking. The equipment surface was completely decontaminated and restored after a 10 minute static soaking by hot water at 90-100°C. The decontamination effect would be even better if it is done dynamically (i.e., with scraper revolving).

Table 4. Summary of Bituminization Tests on 13 Gold Model Liquids

液代 号	(2) 液		(3) 膏		(4) 刮板蒸发器运行参数				(5) 沥青固化物及二次蒸汽冷凝液取样分析值								
	(6) 流量 (l/h)	(7) 温度 (°C)	(8) 流量 (l/h)	(9) 温度 (°C)	(10) 加热温度 (°C)		(11) 加热油温度 (°C)	(12) 真空度 (Torr)	(13) 二次蒸汽温度 (°C)	(14) 出口温度 (°C)	(15) 沥青固化物		(16) 冷凝液 含盐量 (mg/l)	PH			
					(17) 上盘 (°C)	(18) 中盘 (°C)					(20) 含水率 (%wt)	(21) 软化点 (°C)			(22) 含盐量 (%wt)	(23) 酸值 (mg/100g)	
1	30	62~76	15.0	145~148	150~155	150~170	185~193	245~260	80~85	100~103	174~180	0.32	71.3	48.90	3.25	—	—
4	30	94~103	15.0	140~142	158~160	168~174	190~191	250~253	100	100	160~185	0.42	76.5	49.87	4.00	—	16.2
5	34	97~104	8.5	120~140	150~160	146~150	172~180	243~247	100	100	124~136	10.60	71.7	42.66	2.60	—	—
6	33	64~70	16.5	146~150	142~157	138~162	188~192	248~256	100	102	148~170	0.22	65.4	36.20	2.30	—	—
7	30	71~78	12.0	140	165~170	163~170	185~192	260~270	100	100~105	118~182	0.52	70.8	34.45	1.75	—	—
8	34	72~78	11.4	148~149	152~158	150~161	185~200	260~265	90~105	100	135~148	0.25	68.4	31.20	1.90	—	—
9	27	75~79	7.8	145~146	160	165~170	198~200	265~275	100	100	158~165	0.184	83.8	49.14	0.43	—	—
10	21	95~104	10.5	175~178	125~150	142~164	136~144	202~219	20	81~90	152~158	0.08	71.8	51.08	1.06	55.732.8	8.8
11	20	105~107	10.0	168~185	125~127	158~161	139~146	210~211	30	92~93	155~164	0.13	72.2	51.96	1.40	45.239.0	9.1
12	30	100~102	10.0	180~189	117~124	132~140	131~137	217~228	30	89~95	155~161	0.49	67.4	50.05	1.30	44.737.8	8.7
13	20	102~104	10.0	169~181	122~135	143~155	134~135	220~224	30	96	151~160	0.26	75.1	35.83	0.78	18.823.0	8.7
15	22	80	12.0	170	128	122~140	113~116	200~207	80	82~90	140	0.10	64.5	40.00	8.52	230.0	—
16	22	90	10.0	145~170	125~128	126~148	118~125	185~208	45~80	80~90	120~137	0.57	87.6	49.45	5.37	—	—

Key to table on following page.



Key to Table 4:

- |  |  |
|--|--|
| 1. liquid number   | 16. condensate   |
| 2. liquid  | 17. upper section (°C)   |
| 3. asphalt   | 18. middle section (°C)  |
| 4. operating parameters of turbulent evaporator                                | 19. lower section (°C)   |
| 5. analysis of samples of bituminized materials and secondary steam condensate | 20. average water content (% wt)                                     |
| 6. flow rate (l/h)   | 21. average softening point (°C)                                     |
| 7. incoming material temperature (°C)  | 22. average salt content (% wt)                                      |
| 8. flow rate (l/h)   | 23. average leaching rate ( $\times 10^{-4}$ ) (g/cm <sup>2</sup> d) |
| 9. incoming material temperature (°C)  | 24. salt content (mg/l)  |
| 10. heated wall temperature  | 25. oil content (mg/l)   |
| 11. heating oil temperature (°C)   |  |
| 12. vacuum (Torr)  |  |
| 13. secondary steam exit temperature (°C)                                      |  |
| 14. bituminized product exit temperature (°C)                                  |  |
| 15. bituminized material   |  |

Note: scraper revolving speed is 850 rpm

\*The alkalinity of the NaAlO<sub>2</sub> waste water was 2.3N, which made dehydration very difficult. In addition, the product exit temperature was low. Therefore, the water content was high. If pH is adjusted to <1.3, then the product will qualify.



Table 5. Summary of Parameters and Data Analysis for Turbulent Evaporator in Continuous Operation

(1) 运行 时间 总计 (h)	(2) 液 (6) 量 (l/h)		(3) 膏 (8) 量 (t/h)		(4) 刮板蒸发器运行参数					(5) 沥青固体物及二次蒸汽冷凝液取样分析值						
	(7) 温度 (°C)	(9) 温度 (°C)	(10) 上 度 (°C)	(11) 中 度 (°C)	(12) 下 度 (°C)	(13) 热 度 (°C)	(14) 真空 度 (Torr)	(15) 出口 温度 (°C)	(16) 刮出料 产量 (°C)	(17) 固体物		(18) 二次蒸汽				
										(20) 含水率 (%)	(21) 软化点 (°C)	(22) 熔点 (°C)	(23) 凝固点 (°C)	(24) 含盐 (mg/l)	(25) 含油 (mg/l)	
50.00	30	95	19.2	146	130	173	234	100	100	159	1.30	63.5	42.3	0.28~2.8	62~140	—
54.00	60	80	32.0	160	125	180	240	100	100	137	3.10	61.0	33.7	0.87~3.20	138	—
58.00	30	60	19.2	148	135	170	235	100	100	165	0.21	62.9	30.3	0.64~4.00	305	—
61.00	24	62	16.8	150	143	180	240	100	101	172	0.21	62.7	35.8	0.81~4.00	165	—
65.33	36	86	19.2	147	138	174	235	100	101	136	2.00	67.8	40.0	8.00~18.00	133	—
73.00	36	102	19.2	142	140	180	235	102	100	165	0.31	68.4	37.0	1.50~5.30	—	—
82.00	36	75	19.2	148	157	180	240	50	103	165	0.29	70.1	50.0	3.40~5.80	—	—
90.00	36	94	19.2	144	140	188	249	50	104	184	0.29	63.7	36.7	0.28~1.70	—	—
92.66	33	82	19.2	142	152	180	235	50	103	178	0.15	73.2	50.9	2.66	—	—
100.00	33	85	19.2	146	162	180	240	50	104	172	0.18	69.8	45.1	2.12	—	—
105.00	36	100	19.2	145	137	180	248	100	100	167	0.36	67.8	46.6	1.80	—	—
113.00	36	98	19.2	144	139	185	245	100	102	170	1.20	64.4	47.0	2.00	—	—
118.00	30	85	19.2	148	139	180	240	100	102	169	0.88	65.3	43.9	2.10	—	—
125.00	30	84	19.2	147	137	181	243	50	103	158	1.35	63.0	45.3	2.10	—	—
129.00	30	80	19.2	142	140	185	248	100	102	170	0.60	65.9	44.4	—	—	—
135.30	27	90	15.6	140	152	175	240	50	105	165	1.50	69.9	44.5	—	—	—

Key:

1. cumulated continuous operating time of the scraper
2. liquid
3. asphalt
4. operating parameters of turbulent evaporator
5. analysis on samples of bituminized material and secondary steam condensate
6. flow rate (l/h)
7. incoming material temperature (°C)
8. flow rate (l/h)
9. incoming material temperature (°C)
10. heated wall temperature
11. heating oil temperature (°C)
12. vacuum (Torr)
13. secondary steam exit temperature (°C)

Key continued on following page.

Table 5 Key continued:

14. bituminized product exit temperature (°C)	20. average water content (% wt)
15. bituminized material	21. average softening point (°C)
16. condensate	22. average salt content (°C)
17. upper section (°C)	23. average leaching rate ( $\times 10^4$ ) (g/cm <sup>2</sup> d)
18. middle section (°C)	24. salt content (mg/l)
19. lower section (°C)	25. oil content (mg/l)

Note: No 1 liquid was chosen in the experiment. The scraper revolving speed was 850 rpm.

\*The leaching rate is with respect to Na<sup>+</sup>. The specimens were soaked in distilled water statically for 1-15 days. Samples were taken daily for analysis.

Table 6. Differential Thermal Gravimetric Analysis of NaNO<sub>3</sub> Bituminized Products at Various Alkalinities

(1) 沥青固化物中 NaOH 含量 (%wt)	(2) 沥青固化物中 NaNO <sub>3</sub> 含量 (%wt)	DTA		TG	
		起始放热温度 (3) (°C)	放热峰值温度 (4) (°C)	起始失重温度 (5) (°C)	最大失重温度 (6) (°C)
$7 \times 10^{-5}$ (料液 pH = 9) (7)	40	270	342	230	320
0.4 ( = 0.1N)	50	277	364	240	325
1.2 ( = 0.3N)	50	197	340	210	320
2.0 ( = 0.5N)	50	184	347	200	312
2.8 ( = 0.7N)	50	182	327	180	300
4.0 ( = 1N)	50	146	347	160	305
8.0 ( = 2N)	50	167	332	170	295

Key:

1. NaOH content in bituminized products
2. NaNO<sub>3</sub> content in bituminized products
3. initial exothermic temperature (°C)
4. peak exothermic temperature (°C)
5. initial weight loss temperature (°C)
6. maximum weight loss temperature (°C)
7.  $7 \times 10^{-5}$  (solution pH = 9)

3. Recovery of Trichloroethylene Decontaminating Solution. The original turbulent evaporator process is used to recover the decontaminant. Because industrially pure trichloroethylene contains 5 percent tetrachloroethylene, it will decompose and release a small amount of HCl upon contact with a hot surface over 125°C. Therefore, the recovery consists of two boiling processes: trichloroethylene (boiling point 86.7°C) is recovered at 85-95°C, and tetrachloroethylene (boiling point 120.5°C) is collected at 95-135°C. The same receiving tank can be used because the decontaminating effect is the same. The recovery rate in a small scale still is 92.7-96.1 percent. Using a turbulent evaporator, the recovery rate is 88 percent. The softening point of the distillation residue is higher than 59°C. Furthermore, it possesses the characteristics of a bituminized product and can be directly stored in a barrel without further processing.

#### 4.4 Study of Thermal Stability of Bituminized Wastes

Experimental results showed that the bituminized product of  $\text{NaNO}_3$  has an apparent spontaneous exothermic reaction when the temperature reaches around 250°C. If heat is allowed to accumulate so that the temperature reaches the spontaneous combustion point (>300°C), explosion may occur. In order to obtain a reliable and safe operating temperature, it is necessary to study the thermal stability of various bituminized products. An accurate differential thermal balance was used to measure TG and DTA curves of various bituminized products. In the meantime, a constant temperature measuring device for larger specimens was developed to determine the initial exothermic temperatures of various bituminized products. The reproducibility of this device is very good for testing the thermal stability of a mixture. Because a sample can be as large as several kilograms, it is highly representative and the reaction is objective. It is a dependable technique. The experimental results are shown in Tables 6 and 7.

From Tables 6 and 7 one knows that the salt content has little effect on the initial reaction temperature. However, the effect of alkalinity on initial reaction temperature is apparent. When the solution  $\text{pH} > 13$ , the initial reaction temperature decreases apparently with increasing alkalinity. Therefore, it is safe to proceed with bituminization at  $\text{pH} < 13$ .

#### V. Conclusions

##### 5.1 Basic Characteristic Indicators of Bituminized Products

1. Average salt content in bituminized waste:  $45 \pm 5\%$  (wt);
2. average water content in bituminized waste:  $<0.5\%$  (wt);
3. average softening point of bituminized waste: approximately 70°C;
4. average salt grain size in bituminized waste:  $d = 5-8 \mu\text{m}$ ;
5. average leaching rate of bituminized waste (1-17 days with respect to  $\text{Na}^+$ ): approximately  $10^{-1} \text{g/cm}^2 \cdot \text{d}$ ;

Table 7. Thermal Stability Test Values of Various Bituminized Products and Two Raw Materials

(1) 测试单位	(2) 有色冶金院	(3) 北航	(4) 大连化物所	(5) 核工业部1	(6) 核工业部1	(7) 核工业部2	(19) 注
测试方法	起始温度 (°C)	起始温度 (°C)	起始温度 (°C)	起始温度 (°C)	1kg 固化物样品恒温测定起始温度 (°C)	2kg 固化物样品恒温测定起始温度 (°C)	
物料名称	起始温度 (°C)	起始温度 (°C)	起始温度 (°C)	起始温度 (°C)	起始温度 (°C)	起始温度 (°C)	
称量 (g)	起始温度 (°C)	起始温度 (°C)	起始温度 (°C)	起始温度 (°C)	起始温度 (°C)	起始温度 (°C)	
(8)	(9)	(10)	(11)	(12)	(13)	(14)	(15)
1	—	—	271	242	—	240°C 恒温 3.5h 明显放热 (20) (超过油温 + 18°C)	沥青固化物 (21) 含量 40—50% (wt)
4	251	208	235	220	—	210°C 恒温 7h 放热明显 (23) (超过油温 + 2°C)	分析仪器 (26) ① 有色冶金院用国产 4-1-C-1 型差热分析仪。 ② 北京航空学院用国产 CDR-1 型差热分析仪。 ③ 大连化学物理研究所用 (日本) 岛津 DT-2A 型自动记录式差热分析仪。 ④ 核工业部 1 用国产 4.1 型自动记录精密差示热天平。恒温用自制大样量恒温装置。
8	238	250	240	240	275	240°C 恒温 7h 放热明显 (25) (超过油温 + 3°C)	
9	275	261	—	270	235	230°C 恒温 12h 无放热 (28) (超过油温 0°C 即平衡)	
10	276	248	300	260	276	250°C 恒温 4h 后自燃 (30) (超过油温 + 14°C 后自燃)	
11	275	239	285	285	278	240°C 恒温 7.5h 放热明显 (32) (超过油温 + 11°C)	
12	210	210	220	—	242	250°C 恒温 5.5h 放热明显 (34) (超过油温 + 4°C)	
13	271	233	236	—	255	240°C 恒温 5.5h 轻微放热 (36) (超过油温 + 1°C)	
14	—	—	—	—	—	260°C 恒温 10h 无放热 (37) (低于油温 7°C)	
15	—	—	—	—	—	260°C 恒温 5h 放热明显 (38) (超过油温 + 10°C)	
16	—	—	—	—	—	260°C 恒温 7h 产品自燃 (39) (超过油温 + 10°C 后发生)	
17	285	247	280	—	—	260°C 恒温 7.5h 放热明显 (41) (超过油温 + 11°C)	
60号纯沥青	297	218	200	245	197	260°C 恒温 2h 无放热 (44) (低于油温 6°C)	
纯 $N_2O_5$ 盐	—	—	>400	>560	>500	—	

Key on following page.

Key to Table 7.

1. testing institution
2. Institute of Non-ferrous Metallurgy
3. Beijing Institute of Aeronautics and Astronautics
4. Dalian Chemical Physics Institute
5. Ministry of Nuclear Industry 1
6. Ministry of Nuclear Industry 1
7. Ministry of Nuclear Industry 2
8. material or liquid number
9. test method
10. DTA initial exothermic temperature ( $^{\circ}\text{C}$ )
11. TG initial weight loss temperature ( $^{\circ}\text{C}$ )
12. DTA initial exothermic temperature ( $^{\circ}\text{C}$ )
13. DTA initial exothermic temperature ( $^{\circ}\text{C}$ )
14. TG initial weight loss temperature ( $^{\circ}\text{C}$ )
15. DTA initial exothermic temperature ( $^{\circ}\text{C}$ )
16. TG initial weight loss temperature ( $^{\circ}\text{C}$ )
17. initial exothermic temperature measured with 1 Kg of bituminized specimen at constant temperature ( $^{\circ}\text{C}$ )
18. initial exothermic temperature 2 Kg of bituminized specimen measured at constant temperature ( $^{\circ}\text{C}$ )
19. remarks
20. 3.5 h at  $240^{\circ}\text{C}$  constant temperature, obviously exothermic ( $+18^{\circ}\text{C}$  above oil temperature)
21. bituminized products contain 40-50% (wt) salt
22. 8 h at  $230^{\circ}\text{C}$  constant temperature, obviously exothermic ( $+5^{\circ}\text{C}$  above oil temperature)
23. 7 h at  $210^{\circ}\text{C}$  constant temperature, obviously exothermic ( $+5^{\circ}\text{C}$  above oil temperature)
24. 4.5 h at  $250^{\circ}\text{C}$  constant temperature, spontaneously combusted ( $8^{\circ}\text{C}$  lower than oil temperature due to a shifting thermometer)
25. 7 h at  $240^{\circ}\text{C}$  constant temperature, obviously exothermic ( $+3^{\circ}\text{C}$  over oil temperature)
26. analytical instruments: (1) Institute of Non-Ferrous Metallurgy used a domestic Model 4-1-C-1 differential thermal analyzer. (2) Beijing Institute of Aeronautics and Astronautics used a domestic Model CDR-1 dynamic differential thermal analyzer. (3) Dalian Chemical Physics Institute used a Daojing Model DT-2A (Japan) automatic recording differential thermal analyzer. (4) Ministry of Nuclear Industry 1 used a domestic Model 4.1 automatic recording precision differential thermal balance. The home-made large specimen constant temperature device was used for constant temperature measurements.



27. 2 h at 230°C constant temperature, obviously exothermic (+18°C above oil temperature)
28. 12 h at 230°C constant temperature, no exotherm (0°C over oil temperature, i.e., equilibrium)
29. 3 h at 250°C constant temperature, obviously exothermic (+16°C over oil temperature)
30. spontaneous combustion after 4 h at 250°C constant temperature (spontaneous combustion after +14°C over oil temperature)
31. 8 h at 240°C constant temperature, obviously exothermic (+4°C over oil temperature)
32. 7.5 h at 240°C constant temperature, obviously exothermic (+11°C over oil temperature)
33. 5.5 h at 260°C constant temperature, obviously exothermic (+10°C over oil temperature)
34. 5.5 h at 250°C constant temperature, obviously exothermic (+4°C over oil temperature)
35. 3 h at 260°C constant temperature, obviously exothermic, product combusted spontaneously (occurred at +2°C above oil temperature)
36. 5.5 h at 240°C constant temperature, slightly exothermic (+1°C above oil temperature)
37. 10 h at 260°C constant temperature, no exotherm (7°C lower than oil temperature)
38. 5 h at 260°C constant temperature (+10°C above all temperature)
39. 7 h at 260°C constant temperature, product spontaneously combusted (occurred after 10°C above oil temperature)
40. 8 h at 260°C constant temperature, no exotherm (2°C above oil temperature)
41. 7.5 h at 260°C constant temperature, obviously exothermic (+11°C above oil temperature)
42. pure No 60 asphalt
43. 8 h at 230°C constant temperature, no exotherm (20°C lower than oil temperature)
44. 2 h at 260°C constant temperature, no exotherm (6°C below oil temperature).

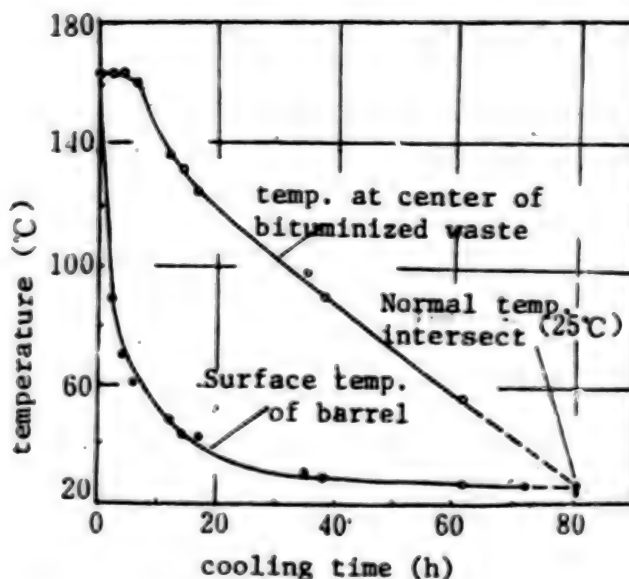
#### 6. Thermal stability of bituminized waste (when pH 13):

- (1) initial weight loss temperature 200°C (measured on TG curves);
- (2) initial exothermic temperature 230°C (measured on DTA curves in constant temperature large specimen tests);
- (3) spontaneous combustion temperature 300°C (measured by TG, DTA, and other methods).

Bituminized waste is loaded in 200 l barrels at 160-170°C. The precipitation of salt is not apparent. It requires approximately 80 hours for the center to naturally cool down to the normal temperature (25°C), as shown in Figure 3.

Figure 3.

Natural Cooling Temperature Curve of a 200 l Package of Bituminized Product from 45 Percent Sodium Nitrate



#### 5.2 Characteristic Indicators of Secondary Steam Condensate

1. average salt content: approximately 30 mg/l;
2. average oil content: approximately 40 mg/l;
3. pH = 7.5-9;
4. purification coefficient of turbulent evaporator with respect to  $\text{Na}^+$ : approximately  $10^4$ .

#### 5.3 Operating Parameters of Turbulent Film Evaporators

1. The optimum linear velocity of the scraper is 9 m/s, the lower limit is 7m/s;
2. vacuum: 50-150 Torr;
3. heating medium: the heat transfer effect was poor when over heated No 38 engine oil was used. The productivity of the turbulent evaporator only reached 40 l/m<sup>2</sup>.h. It is recommended to use steam.
4. The maximum volumetric liquid to asphalt ratio is 4.5:1; the gravimetric ratio is 5:1.
5. The scraper was operating normally, stably and reliably for 600 hours. Moreover, it was adaptable to the bituminization of all 13 model waste liquids.



It is feasible to adopt the process and equipment in the direct bituminization of low and medium level concentrated waste liquids by using a turbulent film evaporator. It is appropriate for continuous production. It is also economical and effective to use industrially pure trichlorochloride as a decontaminant to remove bituminized salt scale. The same process can be used for its recovery. The residue can be loaded in a barrel as a bituminized product without further processing. The heating temperature of the bituminization equipment should be several degrees lower than the initial reaction temperature of the bituminized product (should not be less than 20°C) to ensure the safety of production.

12553

CSO: 4008/36

A  $10^{11}$  W HIGH CURRENT PULSE ELECTRON BEAM ACCELERATOR DESCRIBED

Chongqing HEJUBIAN YU DENG LIZITI WULI [NUCLEAR FUSION AND PLASMA PHYSICS]  
in Chinese Vol 3, No 4, 15 Dec 83 pp 235-240

[Article by Lu Chuanxin [0712 0278 3932], Song Baozeng [1345 1405 1073],  
Wu Guannu [0702 7070 1166], Zhou Pizhang [0719 0013 3864], Zhang Chunsheng  
[1728 1108 3932], Zhang Judi [1728 5468 1229], Zhao Changhe [6392 7022 0735],  
Guo Zhongsen [6753 1813 2773], Man Yongzai [3341 3057 0961], Lu Jingping  
[7627 2417 1627] and Dai Dazhi [2071 6671 2535]: "A  $10^{11}$  W High Current  
Pulse Electron Beam Accelerator"]

[Text] Abstract

A  $10^{11}$  W water medium high current pulse electron beam  
accelerator has been developed. The machine configuration,  
principal parameters and operating conditions are  
described in this paper. The experiments of the diode  
focus are presented in detail and the comparison of  
experimental results for different cathode geometrics is  
given. The pinched electron beam behavior is diagnosed  
by means of an X-ray pinhole camera, a graphite calorimeter  
and a scintillator-optical fiber-photomultiplier system.  
The experimental results are also given.

In order to study the particle beam and target interaction experimentally,  
we developed a  $10^{11}$  W water medium high current pulsed electron beam  
accelerator.<sup>1</sup> The parameters are: output voltage 500 kV, beam current 120 kA,  
peak power approximately  $10^{11}$  W, pulse width (full width at half maximum  
70 ns and total beam energy 3 kJ.

The overall structure of the accelerator is shown in Figure 1. The twenty  
0.166  $\mu$ F parallel capacitors in the LC generator are first charged to  $\pm 80$  kV,  
a command trigger then connects five reversing switches simultaneously.  
After 1.9  $\mu$ s, the output high voltage of the LC generator reaches its peak  
value, and a second command trigger pulse connects the transmission switch  
and the LC generator undergoes linear harmonic charging of the pulse.  
After 320 ns, the voltage of the pulse formation line reaches its peak  
and a third command trigger pulse connects the multichannel output switch  
and the output transmission line then receives a nanosecond pulse with an

amplitude equal to half the pulse formation line voltage and a width equal to twice the transient time. Under the action of this high voltage pulse, the diode emits a high current electron beam due to the field effect.

Figure 2 shows the voltage waveforms measured on the main components of the accelerator.

#### I. LC Pulse High Voltage Generator

As compared to the usual Marx generator, the LC generator does not have a spark switch in the main loop and the advantages are a more compact construction and a lower voltage. Therefore, the LC generator may achieve direct and rapid charging of the pulse formation line without an extra "intermediate storage capacitor."

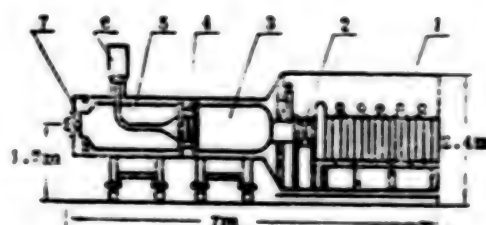


Figure 1. Schematic diagram of the  $10^{11}$ W water medium high current pulsed electron beam accelerator

#### Key:

1. LC generator
2. Transmission switch
3. Pulse formation line
4. Multichannel switch
5. Output line
6. Trigger
7. Diode

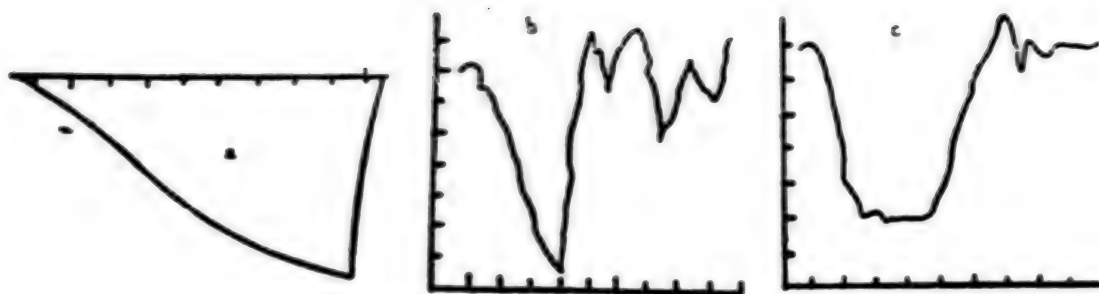


Figure 2. Voltage waveforms of main components

Key:

- (a) LC voltage waveform, time scale is 200 ns/division and peak voltage is 1.26 MV.
- (b) Voltage waveform of the pulse formation line, 100 ns/division, 176 kV/division.
- (c) Voltage waveform of the output line, 20 ns/division, 88 kV/division.

For a given charging voltage, the five reversing loops may be rigorously synchronous in order to obtain the maximum voltage output from the LC generator. The five reversing switches must therefore have a stable self breakdown voltage at a given pressure and good synchronization performance.

We used gas-filled reversing switches with ring-shaped trigger electrodes and contained a gas mixture (10 percent of  $\text{SF}_6$  and 90 percent of  $\text{N}_2$ ) at a pressure of 5 atmospheres. Experiments showed that these switches had a wide operating range for synchronization. The synchronization remained satisfactory even when the operating voltage was lowered to 40 percent of the self-breakdown voltage. This has effectively improved the stability of the generator. Figure 3 shows the open circuit output voltage waveform of the LC generator for synchronized and unsynchronized switches.



Figure 3. Open circuit output voltage waveform of the LC generator

Key:

- (a) Five reversing switches synchronized
- (b) Five reversing switches not synchronized

Table 1. lists the main parameters of the LC generator. Operating results show that this type of generator is suitable for being a high voltage source for 1-2 MV low induction microsecond pulses.

Table 1. LC generator parameters

Maximum charging voltage (kV)	±80
Output voltage (MV)	1.6
Output capacitance (nF)	8.67
Series induction (pH)	3
Maximum energy storage (kJ)	11.0
Series resistance (Ohm)	1.7
Voltage efficiency to pulse formation line (%)	79
Charging time (ns)	320

## II. Water Medium Pulse Formation Line

Both the pulse formation line and the output line are coaxial lines with water as the dielectric and have an outer diameter of 1m and an inner diameter of 0.57m. The impedance is 3.75 Ohms. Deionized water has good insulation properties for short pulses (less than or equal to 1  $\mu$ s) and the breakdown intensity and polarization effects are given by the formulas of J.C. Martin.<sup>2</sup> Since the deionized water has a high dielectric constant ( $\epsilon_r \approx 80$ ), it increases the energy storage density and the geometric dimension of the transmission line. The pulse formation line was operated for an extended period of time under 1.3 MV high voltage pulses and no breakdown was encountered.

## III. Multichannel Gas Trigger Output Switch

Figure 4 shows schematically the structure of the switch. The switch is filled with 10 percent  $\text{SF}_6$  and 90 percent nitrogen gas at 8 atmosphere of pressure. This type of switch is chosen in order to lower the induction and to suppress prepulses so that a fast risetime output pulse may be obtained and to improve the homogeneity and repeatability of the diode current.

[Figure 4., next page]

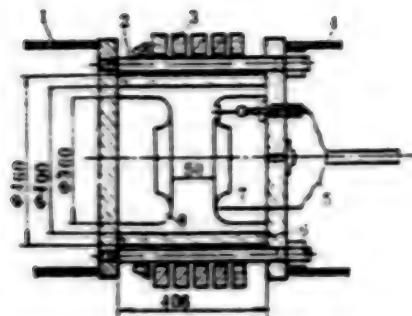


Figure 4. Schematic diagram of the multichannel switch

Key:

1. Formation line
2. Nylon rod
3. Glass ring
4. Output line
5. Trigger cable
6. Nylon tube
7. Trigger electrode
8. Electrode

The anode of the switch has 8 trigger electrodes. Eight SYV-75-9 cables deliver positive pulses (60 kV amplitude and 20 ns risetime) to the trigger electrodes so that the switch may conduct when the voltage of the pulse formation line reaches its peak. Even though the shieldings of the eight cables connect the inner conductor of the output line to ground, the effect on the main pulse transmission can still be neglected because the electromagnetic wave has a long transit time on the cable and the cable has a large inductance.

The technical difficulty of this type of switch is the effective formation of multichannels when the switch is fired. At the present time we have not found a method to measure the number of channels precisely. We roughly estimated the conduction status of the switch by analyzing the risetime of the output voltage. When the switch undergoes self-breakdown, the risetime of the output line voltage is 40 ns, similar to that of a single channel switch. When the switch undergoes trigger breakdown, the risetime is about 20 ns, equivalent to a switch inductance of 60 nH and indicating the formation of multichannels.

In order to avoid internal circuitry (?) on the inner wall of the nylon tube, an organic glass ring is added outside the tube and  $SF_6$  gas is added to reduce the distance between the electrodes. The switch has endured 1.2MV. Aside from periodic replacement of the trigger cable (every 500 fires or so) and cleaning of the switch (every 1,000 fires or so), no other maintenance is required.



#### IV. Radial Insulating Vacuum Diode

The function of the diode is to convert the electromagnetic energy to the electron beam energy and to focus the high current electron beam to the center of the anode in order to compress the energy spatially.

Figure 5 shows the construction of the diode. Also shown are the locations for electric parameter devices. The capacitive voltage divider, resistive current divider, and the Lukevich [?] coil respectively measure the voltage, diode current and the anode current of the diode. The differential ring is used for voltage correction.

We concentrated on the self-pinching characteristics of the electron beam, that is, focusing the electron beam with the magnetic field of the beam itself. We developed three diodes with different cathode geometry, and the experimental results are as follows:

1. Stainless steel needle cathode:<sup>3</sup> The cathode is a stainless steel needle 7 mm long and 1.5 mm in diameter. The anode is a flat piece of brass, separated from the cathode by 3.5 mm. The 1 mm thick brass anode target plate was punched through in one shot at 300 kV. At 450 kV, a 2 mm thick brass target can be punched through in one shot.

Experimental results show that the diode tube with a needle cathode has a small focal spot. The spatial repeatability of the focal spot is good but the total beam energy is small.

2. Hollow graphite cone cathode:<sup>4</sup> This type of cathode is shown in Figure 6. Since the aspect ratio ( $R/d$ ) is large, the critical current ( $I_c = 8500 \sqrt{R/d}$ ) is also large. Tight pinching is obtained at voltages greater than 450 kV. Figure 7 shows the voltage, current, impedance and power variations of this cathode. The total energy of the electron beam is found to be 2.2 kJ by integrating the power curve.

Experimental results show that the hollow cathode diode has a long service life and a large beam energy, but the focus spot size is also large. Under identical experimental conditions, the graphite cathode has a better focusing performance than brass and stainless steel cathodes of the same shape. The larger the inner diameter of the hollow cathode, the longer it lasts before the impedance collapse, but the pinching is poorer (see Figure 8).

3. Stainless steel conical cathode: The structure of this type of cathode is shown in Figure 6(a). Experiment shows that the total beam energy and the focusing spot size is intermediate between the stainless steel needle and the hollow graphite cone cathode (see Table 2). The spatial reproducibility of the focal spot is good. Preliminary tests show a higher power density using this type of cathode.

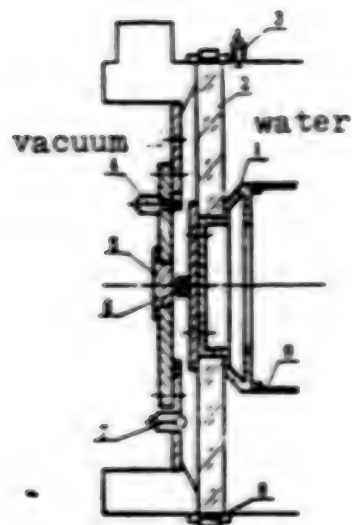


Figure 5. Construction of the diode tube

Key:

1. Transition body
2. Organic glass separator plate
3. Capacitive voltage divider
4. coil
5. Replaceable anode
6. Replaceable cathode
7. Differential ring
8. Resistive current divider
9. Inner tube of the output line

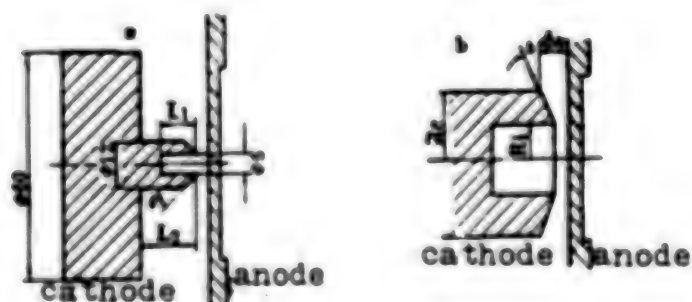


Figure 6. Structure of the diode cathode

Key:

- (a) Conical cathode,  $L_1 = 10\text{mm}$ ,  $L_2 = 15\text{mm}$ ,  $\Theta = 45^\circ$
- (b) Hollow cathode,  $R_c = 25\text{mm}$ ,  $R_1 = 15\text{mm}$ ,  $\delta = 5.7^\circ$ ,  $d_0 = 3.5 \sim 4.0\text{mm}$

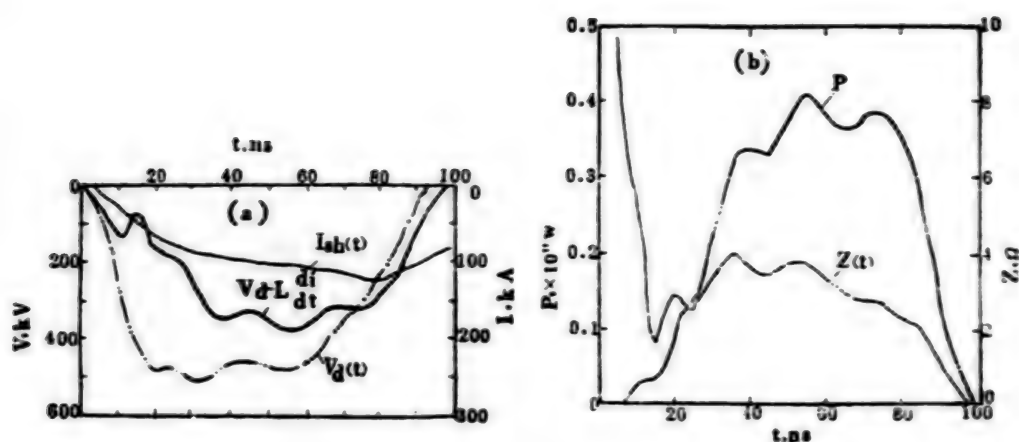


Figure 7. Experimental waveforms of the hollow graphite cathode

Key:

- (a) Voltage and current waveform of the diode
- (b) Impedance and electron beam power of the diode

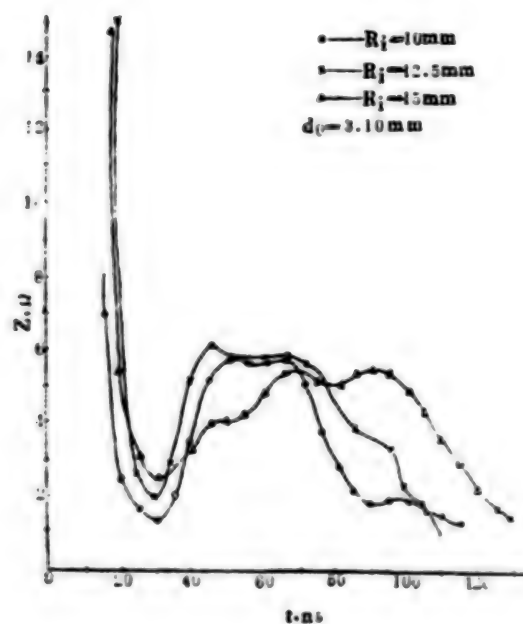


Figure 8. Impedance curve of three hollow cathodes with different inner diameters

Table 2. Diode parameters

Item	Voltage kV	Current kA	$M \frac{di}{dt}$ kV	Anode focal spot mm	Beam energy kJ	Pinch velocity mm/ns
Measuring device	Capacitive voltage divider	coil (current divider)	Differential ring	X-ray pinhole camera	Graphite calorimeter	Optical fiber- photo- multiplier
Cathode shape	planar	260	75	60	--	--
	needle	~630	~120	300	φ 1.2	0.58
	hollow cone	~450	~120	120	φ 3.8	2.10
	conic	~480	~120	190	φ 3.0	0.72

Ye Jinxiang [0673 6855 4382] has diagnosed the electron beam characteristics. Using a graphite differential calorimeter,<sup>5</sup> he measured a total beam energy of 0.58 kJ for the stainless steel cathode diode, 2.1 kJ for the hollow graphite conical cathode and 0.72 kJ for the stainless steel cone cathode. Using an X-ray pinhole camera,<sup>6</sup> he measured a focal spot size of 1.2 mm diameter for the stainless steel needle cathode, 3.8 mm diameter for the hollow graphite conical cathode and 3 mm diameter for the stainless steel conical cathode. Using a scintillator-optical fiber-photomultiplier system,<sup>7</sup> he measured an average pinching velocity of 1.3 mm/ns for the hollow graphite cone cathode. Using the calorimeter-pinhole camera-scintillator-optical fiber system,<sup>8</sup> he measured an average power density of  $1-2 \times 10^{11}$  W/cm<sup>2</sup> for the stainless steel cone cathode.

After operating the accelerator for two years, we found the accelerator to be a convenient high current pulsed electron beam source. By adjusting the charging voltage of the LC generator and the gas pressure in the switches, the diode voltage is continuously tunable in the 200-500 kV range and provides different electron beam parameters.

The authors thank Wang Shiji [3769 0013 4921] for advice and Peng Hansheng [1756 5060 3932], Liu Guoliang [0491 0948 5328], Xiong Riheng [3574 2480 1854], Hua Degen [5478 1795 2704] and He Yongwe [0149 3057 2976] for participating in this research.

## FOOTNOTES

1. Peng Hangsheng, Design Plan for a Water Dielectric Pulsed Electron Beam Accelerator, 1978. Unpublished.
2. J.C. Martin, SSWA/JCM/704/49, AWRE, 4, 1970.

3. E.I. Baranchikov, et al., International Conference on Plasma Physics and Controlled Nuclear Fusion Research, 1, 185 (1976).
4. P. Spence, et al., Proceedings of the International Topical Conference on Electron Beam Research and Technology, 1, 346 (1976).
5. Ling Qiu [0407 3808], et al., Graphite Calorimeter for Measuring the Total Energy of a High Current Pulsed Electron Beam, 1980, unpublished.
6. He Shaotang [0149 4801 1016], Zhao Fengsheng [6392 7685 0581], et al., Focusing of a High Current Pulsed Electron Beam as Measured by Pinhole Photography, 1980, unpublished.
7. Ye Jingxiang, Measuring the Pinch Velocity of a High Current Electron Beam with a Scintillator-Optical Fiber-Photomultiplier System, 1980, unpublished.
8. Ling Qiu, et al., Measuring the Average Power Density of a High Current Pulsed Electron Beam Using a Calorimeter-Pinhole Camera-Scintillator-Optical Fiber System, 1980, unpublished.

9698

CSO: 4008/286

MICRO-DEFORMATION OF QUARTZ UNDER DYNAMIC ACTION AND ITS APPLICATIONS

Beijing DIQIUHUAXUE [GEOCHEMISTRY] in Chinese No 4, 1982 pp 403-411

[Article by Zhu Lin [2612 2651] and Meng Guangkuí [1322 1639 7608] of the Twenty-First Institute]

[Text] Under the action of large stress, rocks and minerals undergo a series of deformation. By studying the micro-deformation of specimens in controlled impact experiments, one can determine the relationship between micro-deformation and pressure and thereby estimate the shock wave pressure endured by rocks in a underground unclear explosion and use the data as a basis for classifying the damage zones in a free-field explosion medium.

There are two experimental methods of inducing micro-deformation in rocks: static pressurization and dynamic shock. A number of techniques exist in the dynamic shock method. The plane wave shock method<sup>1</sup> is a good technique for simulating underground nuclear explosion. In this paper we discuss the plane shock wave experiment in granite medium at China's underground nuclear test site. We also describe the observation results of micro-deformation of quartz under petrographic microscopes and preliminary applications of distinguishing the rock damage zones in the free field after a underground nuclear explosion.

### I. Shock Experiment

The pressure source used in the experiment was a plane wave generator consisting of high-explosive lenses, charge column and detonator. The plane shock wave produced by the high explosive lenses pushed an impactor to hit the specimens in an impact container. The pressure provided by this set-up was experimentally calibrated. By varying the material, thickness and other properties of the impactor, we obtained 15 data points in the pressure range of 30 kbar to 380 kbar. The errors are respectively within 8 percent and 18 percent for the low end and the high end of the pressure range.

The specimens were test ground media. One type of sample is a black mica granite (henceforth referred to as medium 1) and the other type of sample is a black mica plagioclastic granite (henceforth referred to as medium 2). The rock samples were polished to form circular disks with plane and parallel faces 35mm in diameter and 4mm thick. Samples were loaded into the container and shock loaded with the calibrated pressure source. Specimens were then taken out of the container on a lathe.



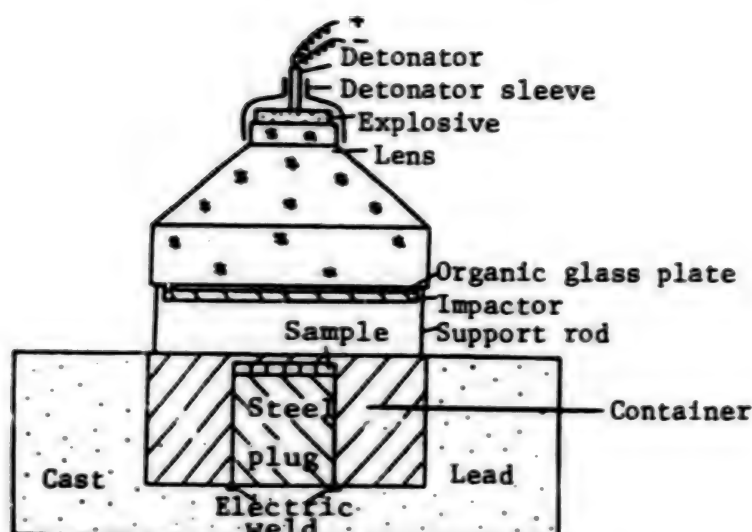


Figure 1. Cross-section of the  $139.4 \pm 2.9$  kbar device

## II. Petrographic Microscopic Observation of the Shock Samples

### 1. Microcrack statistics

Microcracks are the main characteristic deformation of quartz under a low pressure shock. As the pressure increases the number of microcracks also goes up. Microcrack statistics were obtained using a polarized light microscope fitted with a 6-axis planimeter. The number of microcracks in the quartz grains extending vertically over one half the field of view were counted in each measuring line. The same crack in two adjacent halves of field of view was counted as one crack. The length of the measuring line in each sample was generally a few hundred millimeters. By dividing the total number of cracks by the number of measuring lines, we have a value called the "crack index," i.e., the average number of microcracks in one millimeter. The crack index is an indication of the density of microcrack growth for a given pressure<sup>2</sup>. Statistics were collected for the two groups of samples at 7 low pressure points (including zero pressure). Table 1 shows the statistical results and Figure 2 shows the relationship between the crack index and pressure based on the data in Table 1.

Table 1. Crack index in medium 1 and medium 2 at different pressure

Medium	1							2						
Pressure ( $10^4$ bar)	0	3*	5*	7*	7.4	8.7	10.8	0	2.42 $\pm 0.49$	3.57 $\pm 0.44$	6.93 $\pm 1.23$	8.55*	9.97 $\pm 1.38$	11.63*
Crack index	2.2	4.4	8.2	11.2	11.8	14.9	19.3	9.1	10.8	13.5	20.9	28.3	35.8	44.8

\*uncalibrated pressure

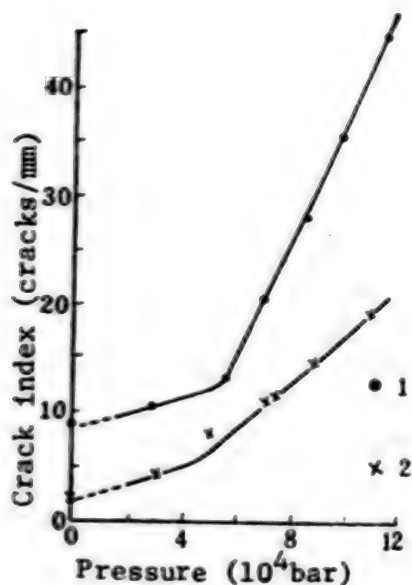


Figure 2. Crack index of quartz as a function of pressure

Key:

1. Medium 1 data
2. Medium 2 data

## 2. Micro-lamellae statistics

When the peak pressure of the shock wave reaches a certain value, a set of parallel and closely spaced ( $2-5 \mu\text{m}$ ) deformation lines with a thickness of  $1-2 \mu\text{m}$  or less begin to appear in the quartz crystal along certain crystalline planes. We shall call one set of parallel lines with one orientation as a group. At low pressure a crystalline grain often grows one group of lamellae consisting of 5 sets or more. At high pressure there may be several groups and the number of sets in each group also increases<sup>3</sup>. These deformation lines are given different names in the literatures. We prefer the term "shock-induced micro-lamellae." The method of collecting statistical data of the micro-lamellae<sup>4</sup> is to place a wafer of standard rock on a (Feishi) rotation stage installed on a polarized light microscope and use a Wolff net plate for the analysis. The angles between the poles of the shock lamellae and the c-axis of quartz are obtained graphically. From the values of these angles, one can determine (by looking up a table) the crystalline plane parallel to the lamellae growth. Generally 100-200 sets of statistical data were collected for each sample. The results are listed in Table 2 and Table 3 and plotted as histograms in Figure 3. In Figure 3 the abscissa is the angle between the micro-lamellae pole and the c-axis of quartz and the ordinate is the growth frequency of the micro-lamellae expressed in percentage. Figure 4 shows the micro-lamellae ratio in quartz as a function of pressure for different orientations in medium 2.

Our observations showed that micro-lamellae in quartz began to grow at a pressure of 87 kbar for medium 1 specimens. For medium 2, the pressure was

69.3  $\pm$  12.3 kbar. We therefore believe that micro-lamellae in quartz in granite samples subjected to a plane shock wave began to grow at a pressure between 70 and 90 kbar.

Table 2. Micro-lamellae of quartz in medium 1 after shock

Freq Crystal plane	P(10 <sup>4</sup> bar)								
	8.7	10.8	11*	14*	17*	18	20*	25.7	CAL
$\omega\{10\bar{1}3\}$	48.3	21.2	27.3	16.7	17.8	13.5	24.6	23.5	22°
$\pi\{10\bar{1}2\}$	14.6	13.4	17.1	15.2	13.9	18.1	26.3	24.7	32°
$\xi\{11\bar{2}2\}$	12.5	17.3	15.9	15.9	18.8	14.8	14.3	17.1	47°
$\tau\{10\bar{1}1\}$	8.3	25.0	13.0	21.7	18.8	16.7	11.4	11.8	52°
$\epsilon\{11\bar{2}1\}$	4.2	2.0	8.0	10.1	15.0	19.4	6.3	10.6	64°
$\pi\{51\bar{6}1\}$	2.0	2.0	0	2.9	3.0	0	0.6	1.2	82°
$\{22\bar{4}1\}$	0	4.0	1.1	2.1	2.0	1.3	3.4	1.8	77°
$\{21\bar{3}1\}$	0	0	1.1	1.5	3.0	5.2	2.3	1.2	71°
$c\{0001\}$	0	0	2.3	1.5	1.0	0	1.7	0	0°
$m\{10\bar{1}0\}$	2.5	0	1.1	0.7	0	2.6	0.6	0	90°
Misc	12.5	15.4	13.6	11.6	6.9	7.7	8.6	8.8	
$\omega/\pi$	3.00	1.58	1.60	1.10	1.28	0.75	0.94	0.95	
$\frac{\xi + \tau + \epsilon + \dots}{\omega + \pi}$	0.05	1.45	0.95	1.77	1.94	1.92	0.80	0.89	

### 3. Ordinary light refractive index changes in quartz

When quartz is subjected to high pressure shock, both its principal refractive indices will change. In our observations, we only made statistical study of the changes in the ordinary light refractive index  $N_o$  of quartz. Because the forces experienced by the shock specimens is nonuniform, the changes of the principal refractive index  $N_o$  in different crystalline grains of the same specimen are not all the same. Even in the same crystal grain the changes in  $N_o$  may still vary with location. Therefore, the pressure dependence can be obtained only after the maximum change in  $N_o$  is found for a specific pressure. The method we used was to select single-crystal grains 100  $\mu$ m (0.1mm) in size or smaller and compare their refractive indices with oils of known index until the maximum  $N_o$  was found. This is the immersion comparison method.

Table 3. Micro-lamellae of quartz in medium 2 after shock

Freq $\backslash$ P( $10^4$ bar)	9.97 $\pm$ 1.38	11.6*	13.94 $\pm$ 0.29	16.12*	17.30 $\pm$ 0.41	20.70*	23.74 $\pm$ 1.71	C $\wedge$ 1
Crystal plane								
$\omega\{10\bar{1}3\}$	59.2	53.0	38.0	37.3	31.1	31.1	29.4	22°
$\pi\{10\bar{1}2\}$	9.6	12.1	21.0	21.2	24.8	31.1	29.4	32°
$\xi\{11\bar{2}2\}$	15.2	13.6	16.4	16.9	15.0	9.9	11.2	47°
$r\{10\bar{1}1\}$	5.6	9.1	9.9	11.0	9.7	8.0	5.9	52°
$s\{11\bar{2}1\}$	3.2	3.0	1.2	3.4	2.9	2.8	2.7	64°
$x\{51\bar{6}1\}$	1.6	0	1.8	1.7	1.5	2.4	3.2	82°
$\{22\bar{4}1\}$	0.8	0	0.6	0	4.4	1.4	2.7	77°
$\{21\bar{3}1\}$	0	1.5	0.6	1.7	1.5	1.9	0	71°
$c\{0001\}$	2.4	4.5	0.6	0	0	0.5	0	0°
$m\{10\bar{1}0\}$	0.8	0	0	0	0	1.4	2.1	90°
Misc	1.6	3.2	9.8	6.8	9.2	9.4	13.4	
$\omega/\pi$	6.17	4.38	1.81	1.76	1.25	1.00	1.00	
$\frac{\xi + r + s + \dots}{\omega + \pi}$	0.42	0.49	0.55	0.61	0.63	0.45	0.45	

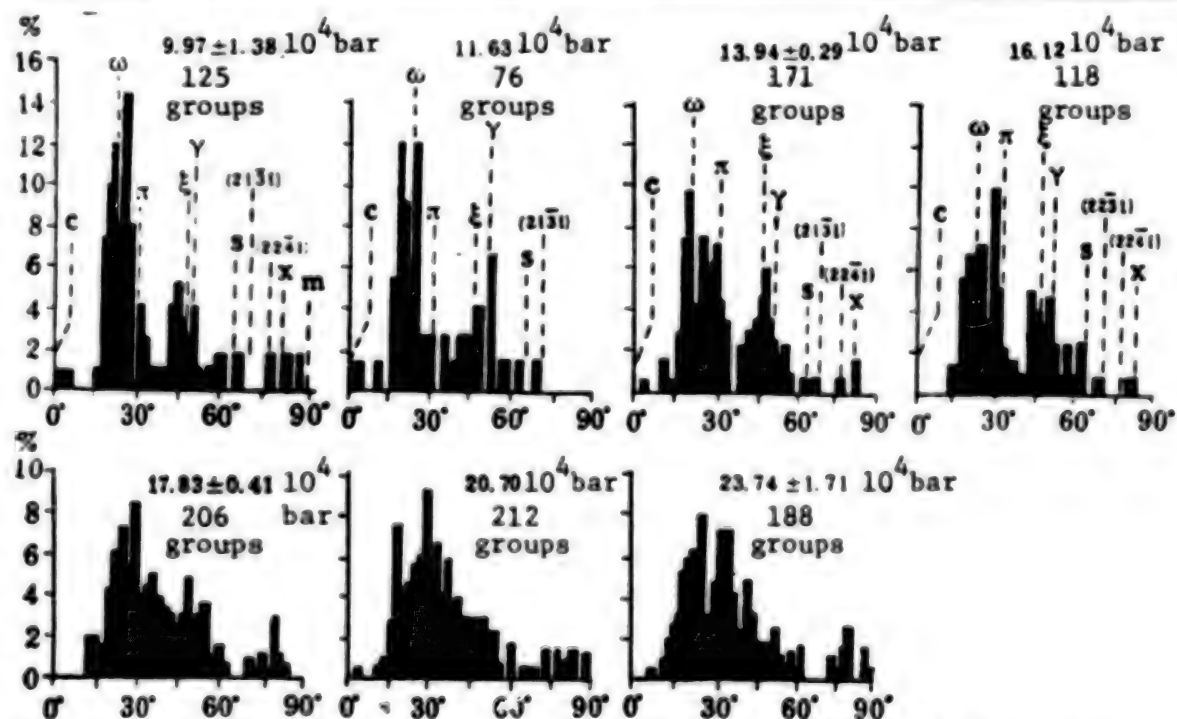


Figure 3. Histogram for medium 2 specimens as a function of the angle between the micro-lamellae pole and the c-axis of quartz

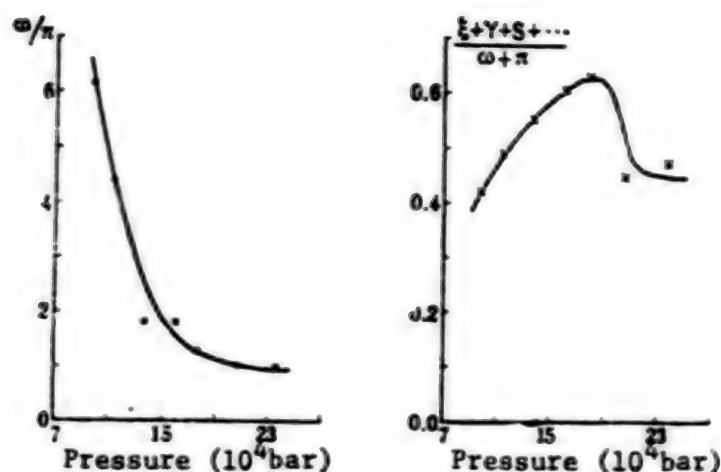


Figure 4. Micro-lamellae ratio of quartz as a function of pressure for medium 2

For each sample we used at least 50 grains in the comparison. The measurement results showed that  $N_0$  of quartz for the two media showed no change for pressures up to 140 kbar. After 140 kbar the refractive index  $N_0$  showed systematic change. The higher the pressure, the lower the  $N_0$ . In a 273.2 kbar medium 2 specimen some of the crystal grains began to homogenize. Its refractive index was about 1.460 and the pressure for total homogenization was about 300 kbar. Table 4 shows the observation results for the two media and Figure 5 shows the decreasing refractive index as a function of pressure.

Table 4. Changes in refractive index  $N_0$  of quartz after shock

Sample P(10 <sup>4</sup> bar)	Medium 1					Medium 2					
	14*	17*	18	20*	25.7	13.94 ±0.29	16.13*	17.83 ±0.41	20.7*	23.74 ±1.71	27.32*
Minimum $N_0$	1.544	1.540	1.539	1.537	1.512	1.544	1.541	1.539	1.535	1.521	1.460
Decrease in $N_0$	0	0.004	0.005	0.007	0.032	0	0.003	0.005	0.009	0.023	0.084

Based on the discussion above, we may draw the following conclusions:

(1) For quartz in granite specimens under controlled shock loading, the principal deformation characteristics at lower pressure is microcracking. 50 kbar is the critical point for the crack index, from a few thousand bar to 50 kbar, the crack index increases slowly, beyond 50 kbar, it increases rapidly.

(2) The shock lamellae begin to develop at a pressure less than 70-90 kbar. In the pressure range from 7 kbar to 12 kbar, the shock lamellae are parallel to the  $\omega \{10\bar{1}3\}$  planes, for pressures greater than 200 kbar [sic],



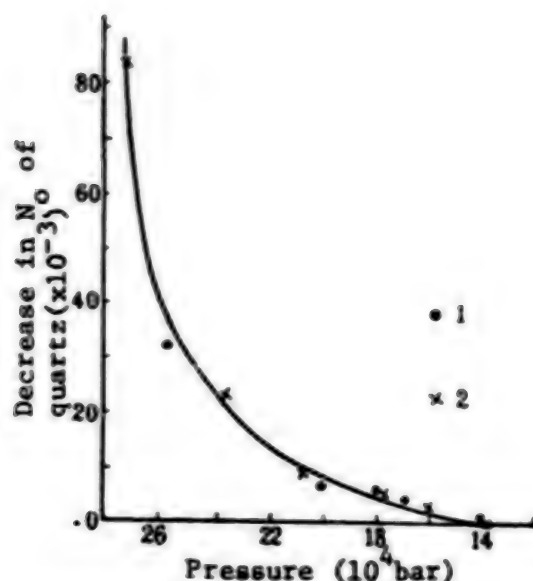


Figure 5. Refractive index of shocked quartz as a function of pressure

Key:

1. Medium 1 results
2. Medium 2 results

the lamellae growth is parallel to the  $\pi \{10\bar{1}2\}$  planes, between 140 and 180 kbar the growth parallel to  $\xi \{11\bar{2}2\}$  and  $\zeta \{11\bar{2}1\}$  dominates. As pressure increases,  $\omega/\pi$  gradually decreases, at medium pressure,  $(\xi + \zeta + \dots)/(\omega + \pi)$  is relatively large and greater than 200 kbar, the two ratios above are independent of pressure, see Figure 4.

(3) At a pressure 150 kbar or so, the ordinary light refractive index  $N_o$  of quartz begins to decrease and the amount of decrease becomes greater as the pressure increases. At the vicinity of 270 kbar, some of the quartz grains begin to homogenize and at 300 kbar all the quartz grains become homogenized.

(4) The petrological properties of the two types of granites are somewhat different, but the shock-induced changes of the quartz in the granite are quite similar and their pressure dependence are also basically the same.

Based on the results just described, we may use the microscopic deformation of quartz in the granite to obtain the peak shock wave pressure experienced by the granite medium in a nuclear explosion. Microcracks may be used in the evaluation of pressures below 100 kbar. Shock lamellae may be used to determine the pressure in the 70 kbar to 200 kbar range. The change in the refractive index  $N_o$  may be used for estimating the pressure from 150 kbar to the pressure that produces homogeneous glass states.

### III. Preliminary Observation of Micro-deformation in Quartz Caused by Nuclear Explosion Shock Wave

An underground nuclear explosion causes damages to the rocks in the peripheral of the cavity. Rock damage is usually divided into the ruptured compact



zone, the cracked loose zone, and the residual stress zone<sup>5</sup>. After one underground nuclear explosion, a probe hole was drilled through the cavity and research specimens were taken from the rock core of the hole. Studies were made using the methods described above. A lamprophyric rock core with a quartz content of only 5 percent was obtained from the section immediately adjacent to the bottom of the cavity. The micro-deformation of quartz should be greatest in the section adjacent to the cavity wall, but difficulties were encountered in the microscopic statistical measurement because of differences in the rock properties and insufficient sample.

In the space below we shall describe the observation results of various deformations and the application to the classification of rock damages in the free field of the explosion.

#### 1. Preliminary observation of microcracks

Since the quartz content in the lamprophyre was too low to satisfy the statistical requirements, we only made statistical measurements of quartz microcracks in granites located slightly farther away from the explosion center and experienced weaker shock waves. Table 5 shows the measurement results and Figure 6 shows the quartz crack index as a function of the radial distance from the cavity wall with the origin taken at the cavity wall.

Table 5. Statistical results of quartz crack index obtained after a underground nuclear explosion

Sample No	Radial distance from cavity wall (m)	Forecast pressure ( $10^4$ bar)	Crack index
19	9.94—10.15	1.70—1.58	3.4
21	11.15—11.75	1.45—1.38	3.6
23	12.00—13.65	1.30—1.18	3.3
25	16.40—17.55	0.96—0.90	2.8
28	22.40	0.68	2.4
29	25.15	0.60	2.4
30	28.15	0.52	2.2
32	33.65	0.40	2.3
35	40.15	0.33	2.4
37	47.28	0.25	2.0

As can be seen in Figure 6, the quartz crack index monotonically decreases as the radial distance from the cavity wall increases. The background value 2.2 is reached at a distance of 33.65m from the cavity wall. Because specimens of 30 kbar or less were unavailable in the experiment, we did not obtain the pressure at which the quartz crack index exceeded the background. Based on quartz microcrack statistics in the American "Hardhat" explosion medium granodiorite obtained by N. M. Short<sup>6</sup>, the quartz crack index began to exceed the preexplosion background at 3 kbar. Because both black mica granite and granodiorite are granites, we used the results of Short and assumed the peak pressure of the shock wave at 33.65m from the cavity wall

to be 3 kbar. This is very close to the 4kbar pressure forecasted for that location, see Figure 7.

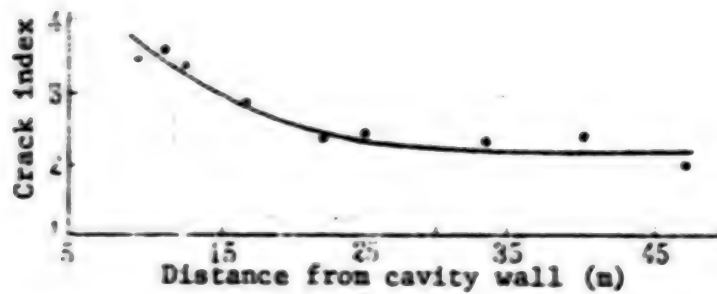


Figure 6. Quartz crack index as a function of radial distance from the cavity wall

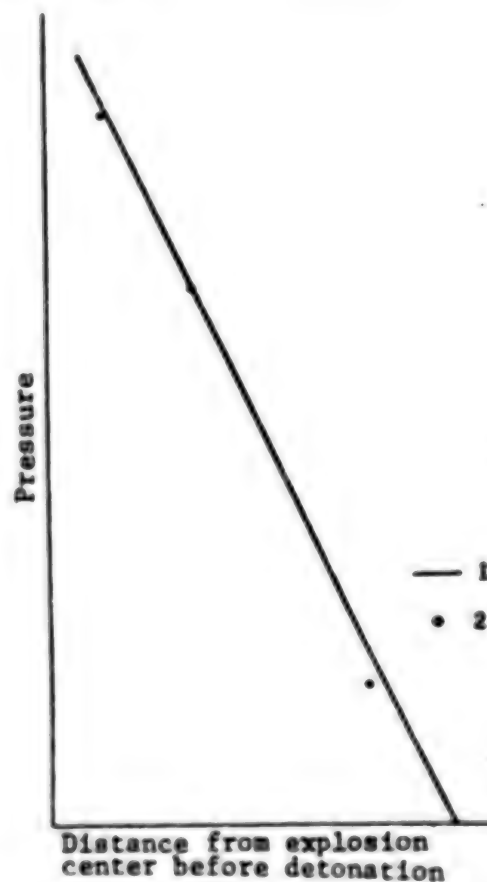


Figure 7. Comparison of calculated pressure and forecasted pressure

Key:

1. Forecasted pressure versus distance
2. Pressure deduced from quartz deformation after the explosion

## 2. Preliminary observation of the shock micro-lamellae

The growth shock micro-lamellae was observation in quartz in the lamprophyre specimens located within 1.65 m from the cavity wall but not outside this range. Since the quartz content was very low in such specimens, a statistical functional study was difficult to make. As described earlier, the pressure at which shock lamellae began to grow in our experiment was 70-90 kbar and the results of Short's study of Hardhat explosion medium<sup>6</sup> showed that shock lamellae began to grow in quartz at a pressure of 50-75 kbar. Even though the shock conditions of these hard intrusions were different and the rock properties were not exactly the same, the pressures at which shock lamellae began to grow in quartz were relatively close. We therefore accept 70 kbar as the pressure at which the growth of shock lamellae began in quartz contained in the lamprophyre. The forecasted pressure at 1.65m from the cavity wall for this particular explosion was also 70 kbar, consistent with the pressure deduced from shock micro-lamellae in quartz.

## 3. Preliminary observation of the change in ordinary light refractive index in quartz

This study was made using the lamprophyre specimens (No 1-4) taken from the vicinity of the cavity wall. The radial distances were 0-0.65m for specimens No 1 and No 2 and 1.15-1.65m for specimens No 3 and No 4. Studies of these specimens showed that only specimen No 1 had homogenized grain with a refractive index of 1.460. In a large single crystal homogenization occurred only locally and the rest of the crystal grain showed shock lamellae growth. This not only showed the inhomogeneity of pressure within a crystal grain but also gave the pressure for the onset of homogenization. As described earlier, the pressure was 273.2 kbar for partial homogenization and 300 kbar for total homogenization, we therefore conclude that the shock wave peak pressure was 270-300 kbar at the location of specimen No 1. Specimen No 1 was closer to the cavity wall than specimen No 2; in terms of color specimen No 1 has changed from the original grayish green to grayish white. The radial distance from the cavity wall to specimen No 1 was estimated to be 20 cm. Therefore, the shock wave peak pressure at 20 cm from the cavity wall in this explosion as deduced from refractive index study was 270-300 kbar, close to the theoretical forecast value of 310 kbar.

The examples given above are applications of controlled shock experiments in the deduction of shock wave peak pressure after nuclear explosions. Table 6 gives a comparison of the pressure deduced from deformation studies and the forecasted pressure. Limited by the number of available specimens, we gave pressure at only three points. The comparison in Table 6 shows good agreement between the deduced pressure and the forecast pressure.

As already discussed, the shock wave of a underground nuclear explosion causes rock deformation and damage in the free field outside the cavity. The results of Short's study showed that at 3 kbar the microcracking in feldspar and quartz contained in granodiorite exceeded the background. The microcracking increased slowly from 3 kbar to 40 kbar. Above 40 kbar, microcracking increased noticeably. As pointed out by Short, 3 kbar is

Table 6. Comparison of the forecasted pressure and the pressure deduced from quartz deformation in a nuclear explosion medium

Quartz deformation	Radial distance from cavity wall (m)	Pressure ( $10^4$ bar)	
		Deduced	Forecast
Grain homogenization	0.20	27-30	31
Lamellae growth	1.65	$7.0 \pm$	7.0
Crack index approaching background	33.65	$0.3 \pm$	0.4

close to the limit of the dynamic tensile strength determined by R. Butkovich and 40 kbar is the dynamic elastic limit<sup>6</sup>. In fact, Short used these two values as the standard for the classification of the rock damage zones in the free field, 40 kbar is the outer boundary of the compact ruptured zone and 3 kbar is the outer boundary of the loose cracked zone. The dynamic elastic limit of the medium 1 granite is 55.4 kbar, close to the 50 kbar pressure at which the quartz crack index made a sudden jump as described earlier. We therefore take 50 kbar as the outer boundary of the compact ruptured zone and the quartz deformation indicator is the pronounced increase in microcracking. We take 3 kbar as the outer boundary of the loose cracked zone and the quartz deformation indicator is that the microcracking begins to exceed the background value. According to our study of the post-explosion specimens, the pressure at a distance of 33.65 m from the cavity wall was 3 kbar and the pressure at a distance of 2.65 m from the cavity wall was 50 kbar<sup>a</sup>). The free field rock damage zones of the underground nuclear explosion studied can be expressed with the following empirical formulae:

$$\begin{aligned}
 \text{Cavity radius} & R_{\text{cavity}} = 11.2 W^{1/3} & (1) \\
 \text{Radius of the compact fractured zone} & R_{\text{compact}} = 12.7 W^{1/3} & (2) \\
 \text{Radius of the loose cracked zone} & R_{\text{loose}} = 30.3 W^{1/3} & (3) \\
 \text{Radius of the residual stress zone} & R_{\text{residual}} = 58.2 W^{1/3} & (4)
 \end{aligned}$$

where  $W$  is the equivalent explosive in kilotons and  $R$  is the distance measured from the explosion center. Equations (1) and (4) are determined from interrogation drilling.

#### IV. Conclusions

In this paper we described the controlled shock experiments in two types of granites using plane waves and presented analysis results of petrographic microscope studies of samples recovered immediately after the explosion. As an example of application, we have also described a study of quartz microdeformation in a underground nuclear explosion and the classification of free

a) The distances given are after the explosion.

field rock damage zones. It should be pointed out that the pressure calculations in the simulation experiments were made using the low pressure equation of state data<sup>7</sup> on the same type of granite in the United States. As discussed earlier, we only deduced the pressure at three points for the actual underground nuclear explosion because of the limited number of available specimens. Of the three points, the 3 kbar pressure at which microcracking exceeded the background was obtained on the basis of Short's conclusion. The other two pressures were deduced from the quartz deformation in the lamprophyre. Even though the quartz deformation in the several types of rocks discussed in this paper are not strong functions of pressure, the conclusions do show a certain degree of similarity. Further research are needed to improve the understanding.

The authors thank Ouyang Ziyuan [2962 7123 5261 6678], Wang Daode [3769 6670 1795] and Xie Xiande [6200 0341 1795] for valuable consultation on the experimental method and Liu Changtai [0491 7022 3141] and Li Shizhang [2621 1102 2222] of the Twenty-First Institute for their contribution to the pressure calibration experiments.

1. N. M. Short, "Experimental Microdeformation of Rock Minerals by Shock Pressures From Laboratory Scale Impacts and Explosion," in Shock Metamorphism of Natural Materials, B. M. French and N. M. Short, editors, 1968, p 219.
2. N. M. Short, J. Geophys. Res. 71, 1195 (1966).
3. F. Horz, "Statistical Measurements of Deformation Structures and Refractive Index in Experimentally Shock Loaded Quartz," in Shock Metamorphism of Natural Materials, B. M. French and N. M. Short, editors, 1968, p 243.
4. He Zuolin [0149 0155 7207], "Application of Stereographic Polar Projection in Geosciences," Science Press, 1965.
5. Lu Yan [7130 1484], Hydrological Geology and Engineering Geology, 5, 36 (1980).
6. N. M. Short, "Nuclear-explosion-induced Microdeformation of Rocks: An Aid to the Recognition of Meteorite Impact Structures," in Shock Metamorphism of Natural Materials, B. M. French and N. M. Short, editors, 1968, p 185.
7. A. J. Chabai and R. C. Bass, "Measurements on a Spherical Shock Wave in a Granite Medium," SC-4741-RR, 1963.

9698

CSO: 4008/52



## LIFE SCIENCES

### FORUM DISCUSSES BIOENGINEERING IN SICHUAN

Chengdu SICHUAN RIBAO in Chinese 7 Feb 84 p 2

[Article by Shen Longyi [3088 7893 0181]: "The Prospects for Biotechnical Research Are Bright: A Summary of a Panel Discussion among Some of Sichuan's Experts"]

[Text] On 24 January, experts from Sichuan University, the Sichuan Medical College, the Chengdu Technical University, the Chengdu Institute of Biology, the Sichuan Institute of Antibiotics, the Sichuan Foods Fermenting Institute and the Sichuan Soil and Fertilizer Institute participated, at the invitation of the Sichuan Science and Technology Commission, in a panel discussion of how to accelerate the development of biotechnology in the province. The experts surveyed the future and raised ideas.

According to these experts, biotechnical engineering includes genetic engineering, cytoengineering, fermentation engineering and enzymatic engineering and forms an important component of the new technological revolution. Bioengineering enjoys much potential for application in Sichuan's economic development, agriculture, animal husbandry, aquatic production, medicine, environmental protection and silk, leather goods, textile, brewing and chemical industries.

Wu Yanyong [0702 5888 1661], associated researcher at the Chengdu Institute of Biology, noted that Sichuan is a leading producer of famous wines, yet output thereof remains low, and the ratio of fine-wine production at Luzhou's old wine cellars is only 10 percent. Thus, if we emphasize microbial fermentation engineering, we can increase taxable profits in fine-wine production by 100 million yuan. Li Zelin [2621 3419 2651], an engineer at the Foods Fermentation Institute, and Huang Guanglin [7806 0342 3829], an associate professor at Sichuan University, stressed the importance of the development of enzyme engineering, stating that enzymatic preparations, simulation and fixation technology enjoy widespread applicability in all fields and that detergents with enzyme additives possess great developmental value. If we employ enzyme technology to effect amylofermentation, we can achieve a general renovation of traditional alcohol production technology. Liu Fangxiu [0491 2455 4423], assistant researcher at the Sichuan Soil and Fertilizer Institute, believes that bioengineering should be utilized in isolating, fermenting and domesticating prized edible fungi and in studying the biological nitrogen fixation of crops. His institute has collected,



isolated and is currently conducting simulated tests of the "gray-tree flower," the "fungus of the immortals" and the "yellow cap," rare fungus species that may prove cultivatable. His institute has also isolated effective soybean nodule bacterial strains that can increase soybean yields by 20 to 30 percent with only 15 fen worth of bacterial manure. Yue Yilun [2867 0110 0243], professor at the Chengdu Technical University, and Hu Xiaosu [5170 1321 4790], associate researcher at the Sichuan Medical College, stressed the importance of bioengineering in medicine. They emphasized the organization of key-task development of artificial heart valves, which efforts can greatly promote research on the cardiovascular system, improve medical treatment and, with some new products, directly yield substantial economic results.

These experts believe that, while Sichuan may have started later than developed countries and continues to lag behind some provinces in China in bioengineering, Sichuan nevertheless possesses many favorable conditions and much potential in this field. First, Sichuan enjoys rich material resources. Our province has more than 10,000 species of higher plants alone, ranks first nationally in terms of gymnosperms and second in angiosperms, produces one-half of China's wild edible fungi and thus is a rich, natural genetic storehouse. We can use biotechnology to develop this storehouse and promote Sichuan's economic development. Secondly, Sichuan possesses considerable technological strength, which is distributed among universities, research units and productive sectors and can be organized into a unified key-task force. Sichuan has 40 institutions of higher learning, disciplines and specialized basic support structures; several tens of central, local and departmental research institutes; and much talent and equipment. Thirdly, bioengineering has already established a foundation in some areas, achieved some progress and produced substantial results in application. If we proceed from Sichuan's actual conditions and organize for the development of bioengineering, we will certainly achieve even greater results in the next few years.

These experts believe that in the short-term Sichuan should focus on providing the things needed in the development of agriculture, light industry, foods and medicine; strengthen technological development in fermentation and enzyme engineering; closely integrate basic research, applied research, extension and application; and strive for economic results. Meanwhile, the province should also organize research and technological development in genetic and cytoengineering at qualified universities and colleges, strengthen inter-provincial and international contact and cooperation, be attentive to the import of technology and equipment and require that colleges and universities strengthen related specialties and curricula so that talent can be trained as soon as possible.

12431

CSO: 4008/205

## LIFE SCIENCES

### MODERN CONTRACEPTIVE DRUG PLANT COMPLETED IN SHANGHAI

Shanghai JIEFANG RIBAO in Chinese 6 Dec 83 p 1

[Article by Wang Yinhua [3769 6892 5478]: "The Contraceptives Plant of the Huaihai Pharmaceutical Factory Is Completed; China's First Modern Contraceptive Drug Plant"]

[Text] Assisted by the UN Fund for Population Activities, China's first modern contraceptive drug plant, the Injectable Contraceptives Plant of the Huaihai Pharmaceutical Factory in Shanghai, has been completed after 17 months of construction. Yesterday (5 December), the Shanghai Pharmaceutical Administration convened a national conference at the site to check and accept the plant and initiate trial production.

This new contraceptives plant meets international pharmaceutical production and quality-control standards and was designed by Shanghai Municipality. The entire project, which includes two large sections for producing drug materials and injection devices as well as auxiliary facilities, covers 26 mu and has a building area of over 10,000 square meters. Primary production equipment and precision instruments were imported from abroad and financed by the United Nations, but the rest of the support components were funded and supplied domestically. Since the plant will employ advanced technology and scientific management, worker safety and waste disposal problems can basically be handled internally.

The plant is designed annually to produce 9.5 tons of such drugs as delalutin and estradiol valerate and 32.5 million multiuse contraceptive injection devices, which can supply the needs of 2.5 million childbearing-aged women for 1 year. Once production formally begins, the plant will double the present supply of such devices and thus will play an important role in controlling population growth in the municipality and in supplying the drug needs of family planning programs in fraternal provinces and municipalities.

Attending yesterday's conference were representatives from the State Pharmaceutical Administration, the China Pharmaceutical Industry Co, the Shanghai Planning and Capital Construction Commissions and other related departments. After careful evaluation, the representatives determined that construction quality meets design specifications and gave approval to commence trial production.

12431

CSO: 4008/205

BRIEFS

**SHANGHAI CONTRACEPTIVES PLANT**—Dedication ceremonies were conducted yesterday (21 February) for the Injectable Contraceptives Plant of the Huaihai Pharmaceutical Factory, construction of which was assisted by the UN Fund for Population Activities. This project, which includes two large sections for producing drug materials and injection materials as well as auxiliary facilities, covers 26 mu and has a building area of 10,000 square meters. Primary production equipment and precision instruments were financed by the United Nations and imported from abroad, but the rest of the support components were funded and supplied domestically. The plant is designed annually to produce 9.5 tons of such drugs as delalutin and estradiol valerate and 32.5 million multiuse injection devices, which can supply the needs of 2.5 million child-bearing aged women for 1 year. Since commencing trial production last year, the plant has already produced 3 tons of drug materials and 3-plus million injection devices. The quality of this output meets national standards, and the project has satisfied design requirements. At yesterday's dedication ceremonies, Li Xiaodong [2621 2556 2639], deputy director of the State Pharmaceutical Administration; Sun Rentong [1327 0088 0681], director of the Shanghai Pharmaceutical Administration; (Baiweila), China-based representative of the UN Fund for Population Activities; and (Boken), administrative director of the International Contraceptive Technology Extension and Application Center, each delivered speeches congratulating the completion of the project and the plant's commencement of production. [Text] [Shanghai JIEFANG RIBAO in Chinese 22 Feb 84 p 1] 12431

**NEW ANTIVENINS**—The JIANKANG BAO [HEALTH] reports that new specific drugs have been added to the treatment of poisonous snake bites. The Shanghai Vaccine and Serum Institute under the Ministry of Public Health, the Pharmacology Teaching and Research Section of the Guangzhou Medical College and other units have cooperated to develop six new antivenins. These drugs include refined antivenins for the Pallas pit viper, the long-nosed pit viper, the many-banded krait and the cobra, which preparations have already been appraised by the state and put into production by the Shanghai Vaccine and Serum Institute; and antivenins for the banded krait and the daboia, which drugs are now undergoing trial use clinically. These drugs neutralize snake venom very effectively. Relevant medical units in Guangxi, Guangdong, Fujian, Anhui and Jiangxi have employed the antivenins to save as many as 1,000 snake-bite victims, and the drugs have shown distinct curative effect. In most minor and grave cases, blood tests are conducted to diagnose the type

of snake bite; and once the appropriate antivenin is administered, the patients' general symptoms disappear within 12 hours and local swelling is basically alleviated. The cure rate is more than 95 percent. [Text]  
[Beijing RENMIN RIBAO in Chinese 15 Mar 84 p 3] 12431

CSO: 4008/205

## SCIENTISTS AND SCIENTIFIC ORGANIZATIONS

### ELECTRONICS, COMPUTER SOCIETIES 1984 ACTIVITIES

Beijing JISUANJI YANJIU YU FAZHAN [COMPUTER RESEARCH AND DEVELOPMENT] in Chinese No 2, 1984 pp 64-65

[Table: "China Electronics Society and China Electronic Computer Society 1984 Academic Activity Plan"]

[See table on following page]

[Text]

Name of Activity	Time & Place	Host Unit	Cooperating Units	Scale	Notes
1. First International Conference on Computers and Their Applications	June, 1984 Beijing				Jointly hosted by China Electronics Society, China Electronic Computer Society and the U.S. Electronics and Electrical Engineering Society and the Computer Society; note: Domestic preparatory meeting to be held in April, 1984 to be attended by domestic workers and programmers
2. Exhibit of Micro-computer Applications	1984, Xi'an	Microcomputer Branch and Shanxi Science Committee	Shanxi Micro-computer Branch		
3. Exhibit of New Microcomputer Products and Technology	1984, Guangzhou	Microcomputer Branch	Guangdong Science Committee and South China Normal Univ. Micro-computer Inst.		



Name of Activity	Time & Place	Host Unit	Cooperating Units	Scale	Notes
4. Microcomputer Applications and Development Training Class	1984	Computer Society and Wuhan Central China Electronic Instrument Plant	Local Units concerned		
5. Third Exchange Meeting on Use and Maintenance Technology of Foreign Equipment	March, 1984, Wuxi	Foreign Equipment Study Group	Wuxi Electronic Computer Plant	150 persons	"
6. Second Computer Maintenance Technology Conference	First Quarter, 1984, Wuhan	Maintenance Study Group	Wuhan Institute 709	150 persons 6 days	Notice soliciting articles already issued
7. Second Microcomputer Program Design and Distribution System Conference	October, 1984, Guilin	Microcomputer Program Design and Distribution System Study Group	Wang Shulin [3769 2885 2651] Chinese Academy of Sciences, Computer Institute	150 persons 7 days	"
8. Digital System Design Automation Conference	August, 1984, Yantai	Digital System Design Automation Specialization Group	He Chengyu 0149 2052 2976] East China Computer Institute	100 persons 5 days	
9. Computer Education and Personnel Training Conference	September, 1984, Hefei	Education Specialization Group, Training Specialization Group	Research Institute of Hefei Industrial University, Beijing Univ. 2nd Branch School	200 persons	

Name of Activity	Time & Place	Host Unit	Cooperating Units	Scale	Notes
10. Software Engineering Conference	Fourth Quarter 1984	Software Branch	Zhu Sanyuan [2612 0005 0337], Shanghai Computer Institute	150 persons	Precise date will be set in mid year when papers have been reviewed and preparations have been made
11. Meeting of the Editorial Committee of the Science Popularization Library	First Quarter, 1984 Beijing	Popularization Committee		25 persons 3 days	
12. Second Conference on Structural Industrial Technology	October, 1984, Changsha	Industrial Technology Specialization Group	Research Institute of the National Defence Science University	100 persons 7 days	
13. Industrial Control-Computer Conference	Third Quarter 1984 Chongqing	Chongqing Institute of Automation		100 persons 5 days	Preparations group already set up
14. Computer Management System (Ministry and Commission 1 Level) Academic Exchange and Proposal Forum	1984, Beijing	Bureau 6, Ministry of Electronics Industry		70-80 persons	To accelerate bureau and ministry network applications work and to promote ministry, bureau and enterprise automated management.
15. Fourth Micro-computer Conference	Second Quarter, Wuhan	Microcomputer Branch	Wuhan 709 Bureau		On the basis of present situation in terms of articles, it has been proposed to delay meeting and requests for articles have already been issued.
16. Second China Computer Diagnosis and Treatment Conference	March, 1984 Wuhan	Shanghai Computer Institute and the Hubei Academy of Chinese Medicine	Department of Computers Central China Industrial College	100 persons 6 days	105 articles have been received and the review committee issued abstracts of the articles

Name of Activity	Time & Place	Host Unit	Cooperating Units	Scale	Notes
17. Conference on Data Base Systems Technology	July, 1984 Tianjin	Sa Shixuan [5646 1597 3551] Software Branch			
Second 18. /Conference on Non-numeric Applications	Third Quarter 1984	Zhu Xuzeng [2612 1331 1073], Chengdu Institute of Computers, Chinese Academy of Sciences		100 persons 5 days	
19. Second Conference on Application of Microcomputers in Peripheral Systems	October 1984, Nanjing	Peripherals Group	52 Bureau 734 Plant	100 persons 5 days	May be postponed until end of 1984 or early 1985, will deal with application of microcomputers in printers.
20. Conference on Triple April, and Multiple Value Logic	April, 1984 Guangzhou		South China	15 persons 5 days	
21. Exchange Conference on Artificial Intelligence	1984	Artificial Intelligence Study Group		100 persons 5 days	
22. Colloquium on Information Storage Technology	Late June 1984 Dalian	Information Storage Tech- nology Study Group	Wei Baolin [7614 1405 2651] Shenyang Institute of Computers		To investigate the present state of information storage technology in China and abroad, discuss future directions
23. Colloquium on Partial Networking of Microcomputers	August, 1984, Chengdu	Microcomputer Branch, System Structure Computers, Specialization Group	Shanghai Institute of Computers, Qinghua Uni- versity	100 persons 5 days	
24. Colloquium on Computer Operations (Use) Management		Maintenance Specialisation Study Group			Self-supporting

Name of Activity	Time & Place	Host Unit	Cooperating Units	Scale	Notes
25. Conference on Disk Use and Maintenance Management Experience		Maintenance Specialization Study Group			Self supporting
26. First National Conference on Computer Technical Training	April, 1984, Suzhou	Technical Training Specialization Group	Suzhou Computer Plant	100 persons	
27. Colloquium on Computer System Function Evaluation	Fourth Quarter 1984	System Structure Study Group	Su Dongzhuang [5685 2639 5445] Computer Department, Northwest Telecommunications Engineering College	40 persons 4 days	Place yet to be determined
28. Exhibit of Microcomputer Applications Results	October, 1984 Xi'an	Microcomputer Branch, Shanxi Science Committee	Shanxi Micro computer Branch	300 persons 10-15 days	exhibitions
29. Exhibit of New Microcomputer Products and Technology	Second Quarter 1984 Guangzhou	Microcomputer Branch	Guangdong Science Committee, South China Normal Univ. Computer Institute	300 persons 10-15 days	Shanghai is also planning an exhibition, time to be determined
30. Network Technical Training Class	Second Quarter, Taiyuan				
31. Training classes to be held in 1984 by Training group					Plans to be announced

AUTHOR: BODDINGTON, T.  
FENG Changgen [7458 7022 2704]  
GRAY, P.

ORG: BODDINGTON and GRAY both of the School of Chemistry, University of Leeds, Leeds, U.K.

TITLE: "Thermal Explosion and Times to Ignition in Systems with Distributed Temperatures. I. Reactant Consumption Ignored"

SOURCE: Beijing BINGGONG XUEBAO [ACTA ARMAMENTARII] in Chinese No 2, May 84 pp 1-14

TEXT OF ENGLISH ABSTRACT: This paper studies the time dependence of spatially distributed temperature profiles in an exothermically reacting system under marginally supercritical conditions (reactant consumption ignored). The earlier results for uniform-temperature systems ( $\beta = 0$ ) have been extended and the quantitative mathematical formula for non-uniform temperature systems ( $0 < \beta \leq \infty$ ),  $t/t_{ad} = M/(\delta/\delta_0 - 1)^{1/2}$ , is derived. The proportionality constant  $M$  is provided and its variation with geometry and the Biot number ( $\beta$ ) is discussed. The geometry studies are the infinite slab, infinite cylinder and sphere and the reaction rate law discussed is Arrhenius' law; however, our results are readily applicable to further geometry studies and rate laws. Our results are also compared with an exact (numerical) solution: the agreement close to criticality is very good and, surprisingly, remains fair up to  $\delta \approx 2$  cr.

AUTHOR: YANG Daren [2799 1129 0117]

ORG: None

TITLE: "The Design of the K $\theta$  Lens Used on a Laser Scanning for Automatic Inspection of Object Size"

SOURCE: Beijing BONGGONG XUEBAO [ACTA ARMAMENTARII] in Chinese No 2, May 84 pp 15-22

TEXT OF ENGLISH ABSTRACT: This paper describes the basic concept, working principle and design process of the K $\theta$  lens to be used on a laser beam scanning system for automatic inspection of object size. Under proper conditions of the pupil and wavelength, the K $\theta$  lens can be optically designed with simple construction, at low cost and satisfactory for practical usage. With an accuracy of  $\pm 3 \mu\text{m}$ , the measuring region stretches to  $47 \times 1000 \text{ mm}^2$ .



AUTHOR: ZHANG Hongming [1728 7703 7686]  
YUN Guobao [0061 0948 1405]  
XU Chengdong [1776 2052 2639]  
et al.

ORG: None

TITLE: "The Crystal and Molecular Structure of 1,3,5-Trinitro-1,3,5-Triazopetane"

SOURCE: Beijing BINGGONG XUEBAO [ACTA ARMAMENTARII] in Chinese No 2, May 84  
pp 43-48

TEXT OF ENGLISH ABSTRACT: The crystal structure of 1,3,5-Trinitro-1,3,5-Triazopetane ( $C_2H_6O_6N_6$ ) has been determined by the X-ray single-crystal diffraction technique. The space group is  $P_{6CN}$ , with  $a = 8.674 (3) \text{ \AA}$ ,  $b = 6.346 (2) \text{ \AA}$ ,  $c = 13.420 (4) \text{ \AA}$ ,  $Z = 4$ . The crystal structure was solved by the direct method, and the hydrogen atom positions were obtained by means of the difference Fourier synthesis technique. The final  $R = 0.048$  for 904 unique observed reflections after least-squares refinement. The shape of the molecule of the compound is a chain configuration having diad axis. The N-N, N-C bond lengths are shorter than those in a normal molecule, and some short intermolecular and intramolecular distances exist. The electronic charge distribution in the molecule is also calculated using the CNDO/2 method.

9717

CSO: 4009/111

AUTHOR: LIU Jiamo [0491 0857 6206]

ORG: Southwestern Institute of Physics

TITLE: "Design of Preliminary Testing of a Particle Injector Beam Transport System"

SOURCE: Chongqing HEJUBIAN YU DENGLIZITI WULI [NUCLEAR FUSION AND PLASMA PHYSICS] in Chinese Vol 3, No 3, 15 Sep 83, pp 180-187

ABSTRACT: First, the beam transport system of a particle injector was described in detail and a photograph of the particle injector was shown. Then, the design considerations and equations for the transport system were given. In order to choose the optimum aperture, the envelop equations were introduced to directly find a solution matching the beam parameters. It was followed by a description of the computation method of the envelop equation. Finally, the tolerance of the system was discussed. The system just underwent preliminary testing. Using a 100 keV arc source with a 40 mA maximum  $H_2^+$  beam, it was already capable of passing a 12 mA  $H_2^+$  beam through a  $4 \times 6 \text{ cm}^2$  limiting aperture to hit a  $\phi 7 \text{ cm}$  target in the capture chamber 175 cm behind the aperture. The effective brightness of the injecting beam was  $4.5 \times 10^6$ , which is comparable to that of  $4.9 \times 10^6$  for OGRA - I.

The manuscript was received on 9 Aug 81. The author wished to acknowledge that the system was fabricated by the Xianfeng Electrical Plant in Shanghai and system testing was performed with the cooperation of the comrades in the ionic source group. He wished to express his gratitude to the relevant people.

12553

CSO: 4009/89

AUTHOR: HUANG Jinhua [7806 6930 5478]

ORG: Southwestern Institute of Physics

TITLE: "Importance of Fusion Neutron to Reactor First Wall"

SOURCE: Chongqing HEJUBIAN YU DENGLIZITI WULI [NUCLEAR FUSION AND PLASMA PHYSICS] in Chinese Vol 3, No 3, 15 Sep 83, pp 129-134

ABSTRACT: Due to the high neutron flux through the first wall, radiation damage and heat accumulation became one of the problems of most concern in studying the design of a fusion reactor. In a spherical geometry, corresponding to an inertially confined reactor, neutron flux could not be accurately calculated by the  $S_n$  method using a point source because of the extreme anisotropy of the uncollided fusion neutron. Heating and radiation damage thus estimated were found to be excessively high. The simplest way was to treat it as a shell source located on the inner surface of the first wall and  $S_{16}$  could provide results with sufficient accuracy. For a cylindrical geometry such as in the case of a magnetically confined fusion reactor, it was possible to estimate the neutron flux with a point source because the anisotropy of the fusion neutron was much weaker. Wide discrepancies were discovered in calculating the power density of the first wall for a specific reactor design. It was identified as due to the difference in the Kerma factor of the iron neutron in various data banks. This effect was further confirmed by the information supplied by Mr Robert Seamon of LANL in Jun 82. Since the Kerma factor is important in determining the behavior of the first wall in the high energy region, it is obvious that further investigation is needed.

The work was completed in November 82 in the Nuclear Engineering Department at University of Wisconsin. The author wished to thank Professor Maynard for the beneficial discussion, Mr Robert Seamon for providing the information, and Comrade Li Shupeí [2621 3359 8951] for translating the English manuscript.

12553

CSO: 4009/89

## Nuclear Science

AUTHOR: DAI Chuanzeng [2071 0278 2582]

ORG: Institute of Atomic Energy, Chinese Academy of Sciences

TITLE: "Nuclear Safety of PWR System"

SOURCE: Beijing HE KEXUE YU GONGCHENG [CHINESE JOURNAL OF NUCLEAR SCIENCE AND ENGINEERING] in Chinese Vol 4 No 2, Jun 84 pp 97-104

TEXT OF ENGLISH ABSTRACT: The status of nuclear safety of the PWR system is reviewed. The "defense in depth" concept and intensive research and development have made the nuclear power industry one of the safest industries in the modern world.

Both mechanistic and probabilistic methodology have been shown to be powerful analytical tools for foreseeing the accident sequence and its probability of occurrence. They are used in further improving the safety of reactor systems.

Important safety measures for preventing severe core damage of the PWR and ensuing serious consequences are discussed for typical cases.

Finally, recent efforts toward further improvements in safety are reviewed.

AUTHOR: LING Shi [0407 1395]

ORG: Shanghai Institute of Nuclear Research, Chinese Academy of Sciences

TITLE: "The Critical Assembly of the Shanghai Institute of Nuclear Research Division of Reactor Technology"

SOURCE: Beijing HE KEXUE YU GONGCHENG [CHINESE JOURNAL OF NUCLEAR SCIENCE AND ENGINEERING] in Chinese Vol 4 No 2, Jun 84 pp 111-116

TEXT OF ENGLISH ABSTRACT: A general description of the slightly enriched uranium fueled and light water moderated critical assembly of the Shanghai Institute of Nuclear Research, Chinese Academy of Sciences, is given. Some experimental works carried out with it are also briefly presented.

The main task of this facility is the research for PWR power plants. The core design is to simulate the clustered fuel assembly structure without a box and the whole lattice arrangement of PWR's. It is also possible to simulate the chemical control of the reactivity by putting soluble boron poison into the light water moderator and reflector. In addition, the following advantages are available: fairly good flexibility of the core structure for the application of pluggable fuel assemblies and improved physical conditions for the application of a pneumatic transportation system of the neutron source.

Most results of the experiments are provided for the designers of the PWR for their reference.

AUTHOR: ZHANG Senru [1728 2773 1172]

ORG: Southwest Institute of Nuclear Reactor Engineering

TITLE: "Some Special Safety Problems of the High Pressurized Intermediate Water Loop of a Nuclear Heat Power Plant"

SOURCE: Beijing HE KEXUE YU GONGCHENG [CHINESE JOURNAL OF NUCLEAR SCIENCE AND ENGINEERING] in Chinese Vol 4 No 2, Jun 84 pp 117-122

TEXT OF ENGLISH ABSTRACT: A nuclear heat power plant adopts a three-loop system power installation. This paper presents a preliminary analysis of some possible accidents associated with the high pressurized intermediate water loop scheme, namely, boric acid dilution, second loop pressure decrease out of the external power supply, etc. The installation not only supplies the steam safely, but also can assure safety during these accidents.



AUTHOR: WANG Jiafeng [3769 1367 0023]

ORG: Southwest Institute of Nuclear Reactor Engineering

TITLE: "Natural Convection in the HFETR Core"

SOURCE: Beijing HE KEXUE YU GONGCHENG [CHINESE JOURNAL OF NUCLEAR SCIENCE AND ENGINEERING] in Chinese Vol 4 No 2, Jun 84 pp 123-128, 104

TEXT OF ENGLISH ABSTRACT: A natural convection experiment has been performed at the beginning of the first cycle in the HFETR. This paper analyzes theoretically the natural convection heat transfer in the HFETR core. For the case of non-uniform wall temperature, non-uniform heat flow and steady and fully developed laminar flow in the multi-annular type fuel element, the heat transfer coefficient for natural convection is well represented by the equation:  $Nu_f = 1.05(RePr)^{\frac{1}{4}} \cdot 2^5$ .

AUTHOR: MAO Zongqiang [3029 1350 1730]  
SUN Shiren [1327 0013 0088]  
MA Xuquan [7456 2700 3123]  
ZHANG Chengqun [1728 2052 5028]

ORG: All of Qinghua University

TITLE: "Influence of Pulse on Mass Transformation in Extraction Column  
(30 percent TBP-Kerosene/ $\text{HNO}_3$ - $\text{UO}_2(\text{NO}_3)_2$  System)"

SOURCE: Beijing HE KEXUE YU GONGCHENG [CHINESE JOURNAL OF NUCLEAR SCIENCE  
AND ENGINEERING] in Chinese Vol 4 No 2, Jun 84 pp 129-135

TEXT OF ENGLISH ABSTRACT: A pulsed column is a kind of important extraction equipment. At present, studies of mass transfer in extraction columns require consideration of the effect of longitudinal mixing. Some authors have engaged in such studies and a number of calculation methods for the pulsed extraction column have been established.

This paper represents the characteristics of mass transfer for low concentration uranium-nitric acid-water/TBP-kerosene system in an air-pulsed nozzle plate extraction column of a two-inch diameter. Stable concentration profiles under different pulsed conditions were determined by separately sampling each phase from the extraction column. Data obtained were treated by a simple approximation method using a diffusion model. The relation between pulse intensity and true height of the mass transfer unit in which the effect of longitudinal mixing has been deducted is obtained.

AUTHOR: WANG Kuiwu [3769 7608 2976]  
WANG Changyin [3769 7022 7113]  
LIU Mingshe [0491 2494 0772]  
WANG Enyue [3769 1869 6460]

ORG: All of Southwest Institute of Physics

TITLE: "Progress in Engineering Studies of a Steady-state Superconducting Mirror Machine"

SOURCE: Beijing HE KEXUE YU GONGCHENG [CHINESE JOURNAL OF NUCLEAR SCIENCE AND ENGINEERING] in Chinese Vol 4 No 2, Jun 84 pp 143-152

TEXT OF ENGLISH ABSTRACT: A steady-state superconducting mirror machine is outlined. The results obtained during 1977-1982 are given for separate adjustments on its vacuum system, electrosystem, ion injector, physical alignment of particle beam, carbon arc neutralizer and cryogenic superconducting system of the magnetic trap, and for whole system adjustment.

After adjustments of separate parts and the whole system, the engineering goal of this machine, as the first step, has been achieved: the energy of the ion source is 100 keV; the total ion current is 0.7 A, the current of  $H_2^+$  is 120 mA and 26 mA at the access of magnetic lenses for focus and at the trap center respectively; the equivalent current of a neutral beam at the trap center is 7.2 mA; the operation of superconducting magnets has lasted for 9 hours at 4.2 K, and 21.7 kGs of the magnetic field at the trap center has been obtained when the magnet current is 133 A; and by using cryopumps, the background vacuum in the magnetic trap is  $4.8 \times 10^{-9}$  Torr and  $3.5 \times 10^{-8}$  Torr with beam injection.

9717  
CSO: 4009/121

END

**END OF**

**FICHE**

**DATE FILMED**

18 Sept. 1984

JPRS-CST-84-025

10 September 1984

# China Report

SCIENCE AND TECHNOLOGY

**FBIS** FOREIGN BROADCAST INFORMATION SERVICE

#### NOTE

JPRS publications contain information primarily from foreign newspapers, periodicals and books, but also from news agency transmissions and broadcasts. Materials from foreign-language sources are translated; those from English-language sources are transcribed or reprinted, with the original phrasing and other characteristics retained.

Headlines, editorial reports, and material enclosed in brackets [ ] are supplied by JPRS. Processing indicators such as [Text] or [Excerpt] in the first line of each item, or following the last line of a brief, indicate how the original information was processed. Where no processing indicator is given, the information was summarized or extracted.

Unfamiliar names rendered phonetically or transliterated are enclosed in parentheses. Words or names preceded by a question mark and enclosed in parentheses were not clear in the original but have been supplied as appropriate in context. Other unattributed parenthetical notes within the body of an item originate with the source. Times within items are as given by source.

The contents of this publication in no way represent the policies, views or attitudes of the U.S. Government.

#### PROCUREMENT OF PUBLICATIONS

JPRS publications may be ordered from the National Technical Information Service, Springfield, Virginia 22161. In ordering, it is recommended that the JPRS number, title, date and author, if applicable, of publication be cited.

Current JPRS publications are announced in Government Reports Announcements issued semi-monthly by the National Technical Information Service, and are listed in the Monthly Catalog of U.S. Government Publications issued by the Superintendent of Documents, U.S. Government Printing Office, Washington, D.C. 20402.

Correspondence pertaining to matters other than procurement may be addressed to Joint Publications Research Service, 1000 North Glebe Road, Arlington, Virginia 22201.



10 September 1984

## CHINA REPORT SCIENCE AND TECHNOLOGY

### CONTENTS

#### PEOPLE'S REPUBLIC OF CHINA

#### APPLIED SCIENCES

Radiographic Inspection of Butt Welds Described (Zhang Junzhe; WUSUN JIANCE [NONDESTRUCTIVE TESTING], No 2, 1984).....	1
Thermophysical Properties of Matter (ZIRAN ZAZHI [NATURE JOURNAL], No 1, 1984).....	11
Pilot Model Test for Bituminization of Concentrated Radioactive Wastes Using Continuous Turbulent Film Evaporator (Li Dongcai; HE KEXUE YU GONGCHENG [CHINESE JOURNAL OF NUCLEAR SCIENCE AND ENGINEERING], Vol 3, No 2, Jun 83)....	13
A $10^{11}$ W High Current Pulse Electron Beam Accelerator Described (Lu Chuanxin, et al.; HEJUBIAN YU DENGLIZITI WULI [NUCLEAR FUSION AND PLASMA PHYSICS], Vol 3, No 4, 15 Dec 83).....	33
Micro-Deformation of Quartz Under Dynamic Action and its Applications (Zhu Lin, Meng Guangkui; DIQIUHUAXUE [GEOCHEMISTRY], No 4, 1982).....	43

#### LIFE SCIENCES

Forum Discusses Bioengineering in Sichuan (Shen Longyi; SICHUAN RIBAO, 7 Feb 84).....	55
Modern Contraceptive Drug Plant Completed in Shanghai (Wang Yinhua; JIEFANG RIBAO, 6 Dec 83).....	57

Briefs		
Shanghai Contraceptives Plant		58
New Antivenins		58
SCIENTISTS AND SCIENTIFIC ORGANIZATIONS		
Electronics, Computer Societies 1984 Activities		
(JISUANJI YANJIU YU FAZHAN [COMPUTER RESEARCH AND		
DEVELOPMENT] No 2, 1984).....		60
ABSTRACTS		
Armaments		
(BINGGONG XUEBAO [ACTA ARMAMENTARII], No 2, May 84).....		66
Nuclear Engineering		
(HEJUBIAN YU DENGLIZITI WULI [NUCLEAR FUSION AND PLASMA PHYSICS],		
Vol 3, No 3, 15 Sep 83).....		69
Nuclear Science		
(HE KEXUE YU GONGCHENG [CHINESE JOURNAL OF NUCLEAR SCIENCE AND		
ENGINEERING], Vol 4, No 2, Jun 84).....		71

## RADIOGRAPHIC INSPECTION OF BUTT WELDS DESCRIBED

Shanghai WUSUN JIANCE [NONDESTRUCTIVE TESTING] in Chinese No 2, 1984 pp 16-19

[Article by Zhang Junzhe [1728 0193 0772]: "Radiographic Inspection of Butt Welds in Small Spherical Thick-Wall Vessels"]

### [Text] Introduction

Fig. 1 shows a small spherical thick-wall vessel with 100-200 mm outer diameter and 6-10 mm wall thickness; it is made of 1Cr18Ni9Ti austenitic stainless steel, and is constructed by welding together two forged hemispherical shells. It is difficult to use ultrasonic techniques to inspect the welds because signals from material defects cannot be identified due to interference of reflected waves from coarse crystals and stop joints. Therefore, radiographic techniques with sensitivity no less than 2 percent must be used.

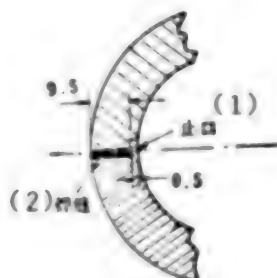


Fig. 1 Schematic Diagram of the Butt Weld and Stop Joint of a Small Spherical Thick-Wall Vessel

KEY: (1) Stop joint  
(2) Butt weld

Clearly, to apply X-ray inspection for this type of butt welds, only the double-wall transillumination, double-image technique can be used. But the image quality is affected by the curvature and wall thickness of the inspected object and the scattered rays. Therefore, to achieve satisfactory results, it is necessary to give careful consideration to the selection of focal

distance, angle of incidence, radiation hardness, intensifying screen and film; it is also necessary to take appropriate measures to improve the shield for scattered radiation and the design of penetrometer.

#### Selection of Focal Distance

In general, to obtain sharp images require the focal distance to be as large as possible. Also, due to the conical scattering pattern and continuous spectrum of X-rays and the effect of curvature and wall thickness of the inspected object, the penetration distance and surface intensity of the X-rays will vary from one part of the object to another. In Fig. 2, if  $f_1 > f_2$ , then  $t_2 > t_1 > t$ ; let  $k$  denote the thickness ratio,  $k_1 = t_1/t$ ,  $k_2 = t_2/t$ , then  $k_1 < k_2$ . From the law of X-ray attenuation  $I = I_0 \exp(-\mu t)$ , and the fact that  $t < t_1 < t_2$ , it follows that  $I > I_1 > I_2$ . This effect is even more pronounced under the condition of double-wall transillumination. It can be seen that the thickness ratio  $k$  decreases with increasing focal distance, which ensures the uniformity of film blackness and the sensitivity of detecting defects along the edges of the inspected object. From this point of view, the focal distance clearly should as large as possible.

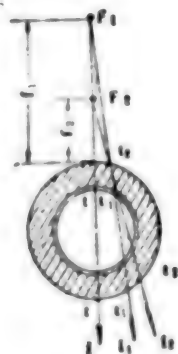


Fig. 2 Comparison of Focal Distances

However, with larger focal distance, the tube voltage and exposure time must be increased in order to ensure sufficient amount of light exposure; as a result, the degree of foginess will increase and the degree of contrast will decrease. In addition, the increase in scattered rays caused by higher tube voltage will have a serious effect on the clarity of image. If the tube voltage remains unchanged while the focal distance is increased, then the exposure time must be increased significantly to achieve the same amount of exposure, again resulting in increased scattered rays and reduced clarity.<sup>[1]</sup> Test results showed that in order to meet the technical requirements of geometric lack of clarity, the focal distance should be as small as possible. The focal distance selected for our application was 1 meter.

## X-Ray Angle of Incidence

In applying the double-wall transillumination technique to inspect the butt welds of spherical thick-wall vessel, the beam center of the X-ray should be offset from the plane of the butt weld in order to achieve a small-opening elliptical image of the butt weld. For a small-diameter, thick-wall vessel, the upper layer of the butt weld image cannot satisfy the sensitivity requirement; only the lower layer can be diagnosed. The X-ray angle of incidence should be determined such that the upper and lower images are as close to each other as possible without overlapping in order to avoid overamplification of the images of the lower butt weld and the defects, and possible mis-inspection due to the low degree of contrast.

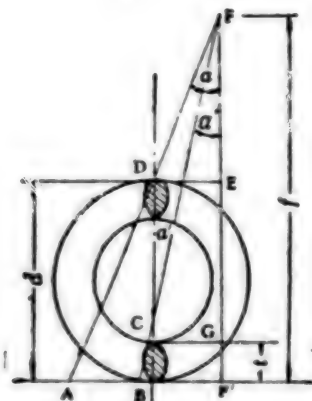


Fig. 3 Selection of Angle of Incidence

In Fig. 3, the outer diameter of the vessel is denoted by  $d$ ,  $F$  is the focal point,  $f$  is the focal distance,  $t$  is the wall thickness, and  $\alpha$  is the angle of incidence. The ray is projected from the focal point  $F$  to the center of the butt weld, through two layers of wall and onto the film at point  $A$ ; the base of the lower butt weld surface is projected onto the point  $B$ , whose angle of incidence is  $\alpha'$ . Then, in  $\triangle FAF'$  and  $\triangle FBF'$ : [3]

$$AF' = f \cdot \tan \alpha$$

$$BF' = f \cdot \tan \alpha'$$

$$\therefore AB = f(\tan \alpha - \tan \alpha') \quad (1)$$

In  $\triangle FDC$ ,  $\angle FCD = \alpha'$ ,  $\angle FDC = 180^\circ - \alpha$ .

$$FD = \frac{f-d}{\cos \alpha}, \quad FC = \frac{f-t}{\cos \alpha'}$$

From the law of sines:

$$\begin{aligned} \frac{FD}{\sin \alpha'} &= \frac{FC}{\sin(180^\circ - \alpha)} \\ \text{i.e.,} \quad \frac{(f-d)/\cos \alpha}{\sin \alpha'} &= \frac{(f-t)/\cos \alpha'}{\sin(180^\circ - \alpha)} \\ \therefore \frac{(f-d)/\cos \alpha}{\sin \alpha'} &= \frac{(f-t)/\cos \alpha'}{\sin \alpha} \end{aligned}$$

then,

$$\begin{aligned} \operatorname{tg} \alpha (f-d) &= \operatorname{tg} \alpha' (f-t) \\ \therefore \operatorname{tg} \alpha' &= \frac{f-d}{f-t} \cdot \operatorname{tg} \alpha \end{aligned} \quad (2)$$

By substituting equation (2) into (1), one obtains the following:

$$\begin{aligned} AB &= f \left( \operatorname{tg} \alpha - \frac{f-d}{f-t} \cdot \operatorname{tg} \alpha \right) = \operatorname{tg} \alpha \cdot f \left( \frac{d-t}{f-t} \right) \\ \therefore \operatorname{tg} \alpha &= \frac{AB(f-t)}{f(d-t)} \\ \alpha_{\max} &\leq \operatorname{tg}^{-1} \left[ \frac{AB(f-t)}{f(d-t)} \right] \end{aligned} \quad (3)$$

In equation (3), AB is the elliptical opening of the X-ray image center of the butt weld, which can be determined from the required width of the image; the value of  $\alpha$  then can be determined accordingly. For example, suppose  $AB=20$  mm for a vessel with  $d=200$  mm,  $t=10$  mm, and  $f=1000$  mm, then  $\alpha$  is calculated to be  $\leq 6^\circ$ ; if  $AB=30$  mm, then  $\alpha \leq 9^\circ$ ; if  $AB=40$  mm, then  $\alpha = 12^\circ$ . For a vessel with  $d=100$  mm,  $t=10$  mm, and assume  $AB=20$  mm, then  $\alpha \leq 12^\circ$ ; if  $AB=30$  mm, then  $\alpha \leq 18^\circ$ . In actual inspection, the angle of incidence for a 200 mm-diameter vessel is chosen to be around  $10^\circ$ ; for a 100 mm-diameter vessel, the angle of incidence is chosen to be around  $15^\circ$ .

#### Radiation Hardness, Film and Intensifying Screen

For a given focal distance and rated tube current, the exposure condition is determined by the tube voltage and exposure time. By selecting a relatively low tube voltage, the average wavelength of X-ray is longer, or the radiation quality is said to be softer. As a result, the attenuation of rays through the material is more pronounced, thus increasing the contrast ratio and improving the sharpness of X-ray photography. The attenuation coefficient is given by  $\mu = C Z^3 \lambda^3$  ( $Z$  is the atomic coefficient of the material,  $\lambda$  is the wavelength of the incident ray,  $C$  is the speed of light); thus, the longer the wavelength, the larger  $\mu$  becomes, the better the contrast ratio and the higher the sensitivity in revealing material defects. Conversely, if a higher voltage is used, the X-ray generated will be harder, and the contrast ratio will be reduced; as a result, level of scattered rays will increase, and the quality of X-ray photography will be adversely affected. In applying the



technique of double-wall transillumination to inspect thick-wall vessels, if the tube voltage is too low, the exposure time becomes excessive, and penetration may be impossible. Therefore, in selecting radiation hardness, we must first ensure penetration (at the thickest part of transillumination) and select as low a tube voltage as possible without excessive exposure time. Test results showed that when using the Model 2515 X-ray inspection unit on a vessel with 6 mm wall thickness (i.e., penetrating a double wall thickness of 12 mm), satisfactory transillumination results were obtained by selecting the tube voltage to be 180 KVP, the tube current to be 18 mA, and the exposure time to be 4 minutes; for a 10 mm-thick vessel (penetrating a double wall thickness of 20 mm), a tube voltage of 200 KVP, tube current of 18 mA and exposure time of 5 minutes were selected.

Under the condition of the focal distance and exposure time as indicated above, penetration can only be achieved by using an intensifying screen. While fluorescent intensifying screen would allow penetration, the resulting image quality was so poor that diagnosis of the negative may not be possible. Later, satisfactory results were obtained by using 0.1 mm lead-foil intensifying screens (the front and back screens had the same thickness). Such screens not only provided intensification and reduced exposure time, they could also absorb scattered rays to improve the clarity of the negatives.

Test results also showed that even with lead-foil intensifying screens, the contrast ratio and clarity of certain films were still very poor. To achieve satisfactory results, we used the Belgium Gevoert D4 type film, which was a medium-speed film with high contrast ratio and very fine particles. The higher speed Gevoert D7 film was also satisfactory.

#### Shielding of Scattered Rays

Although we took various technical measures such as careful selection of the technical parameters, and the use of lead-foil intensifying screens and D4 type films, it is still difficult to obtain high-quality X-ray pictures without taking special measures in shielding the scattered rays. A small spherical thick-wall vessel is different from ordinary small-diameter thick tubes. Since the film cannot be bent into a sphere, the contact surface between the lower butt weld of the vessel and the film is very small. On the other hand, the effective region of the image obtained from transillumination must have a finite length; also, due to the large double-wall transillumination thickness, the high tube voltage, and the long exposure time, scattered rays pose a serious problem and must be carefully shielded.

To achieve more effective shielding, we took the following measures: (1) we used a lead-foil intensifying screen to absorb a large amount of scattered rays during the period of exposure; (2) we used a large 5 mm-thick lead-foil screen backing to absorb scattered rays arriving from the rear; (3) we built a special frame to perform shielded photography, as shown in Fig. 4. The thickness of the shield plate was 5 mm, and the opening at the bottom was used for inserting and retrieving the negatives. It is our experience that the shielding of scattered rays is the most important factor in X-ray transillumination of butt welds of small spherical thick-wall vessel.

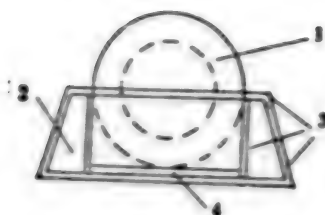


Fig. 4 Frame for Shielded Photography

- KEY: (1) Vessel  
 (2) Wooden box  
 (3) Lead plate  
 (4) Negative

#### Control of Effective Range of Transillumination and the Segmented Measurement Method

It has been pointed out in the discussion of focal distance selection that the blackness and sensitivity requirements of the midsection and boundary of the negative can be satisfied only by appropriately controlling the thickness ratio  $k$  (in the case of a flat plate, the effect of  $k$  can be ignored). Based on production experience and technical requirements on the blackness of negatives to comply with radiographic inspection standards for butt welds, we have specified a standard blackness value of  $D=1.5$  (as measured by the MDX-2 black and white densitometer). Within the effective region of X-ray exposure, the blackness of negatives decreases uniformly from the center of the ray toward the two edges; when the difference in blackness reaches  $\Delta D=0.5-0.6$ , calculations using the steel-wire penetrometer (the XZQ-1 image quality indicator) show that the ray center and the edges have the same sensitivity level. It is pointed out in Ref. 2 that for materials with transillumination thickness of less than 20 mm, an appropriate value for the thickness ratio  $k$  is 1.25. Ref. 3 presents a method of calculating the length of the effective transillumination range (Fig. 5). Suppose the diameter of the vessel is  $d$ , the wall thickness is  $t$ , and the controlled thickness ratio is  $k=1.1$ , then the length  $AB$  in the figure is  $AB=1.1t$ .  $\alpha$  is the angle of the incident ray.



Fig. 5 Control of Effective Transillumination Range

In  $\triangle ABO$ ,  $OA=R-d/2$ ,  $OB=R-t$ ,  $AB=1.1t$ .

From the law of cosines

$$\begin{aligned} OB^2 &= OA^2 + AB^2 - 2AB \cdot OA \cdot \cos \alpha \\ \therefore (R-t)^2 &= R^2 + (1.1t)^2 - 2.2Rt \cos \alpha \end{aligned}$$

or

$$\begin{aligned} \cos \alpha &= (d + 0.21t) / 1.1d \\ \therefore \alpha &= \cos^{-1} [(d + 0.21t) / 1.1d] \end{aligned} \quad (4)$$

Also, in  $\triangle FAO$ ,

$$\begin{aligned} \therefore \alpha &= \alpha' + \theta \\ \therefore \theta &= \alpha - \alpha' \\ \therefore \angle ACO &= \angle BAO = \alpha \\ \therefore \theta' &= \alpha + \alpha' \\ \therefore \angle AFO &= \angle OFB = \alpha', \\ \angle F'OD &= \angle F'OC = \theta' \\ \therefore 2(\theta + \theta') &= 4\alpha \end{aligned} \quad (5)$$

The length of the effective transillumination range  $L$  is equal to twice the arc lengths corresponding to the central angles  $\theta$  and  $\theta'$ . Thus,

$$L = \pi d \cdot 4\alpha / 360^\circ \quad (6)$$

Substituting equation (4) into (6) gives

$$L = \pi d [\cos^{-1} (d + 0.21t) / 1.1d] \cdot (90^\circ)^{-1} \quad (7)$$

By the same token, when the controlled thickness ratio is  $k=1.2$ , then

$$L = \pi d [\cos^{-1}(d + 0.44t) / 1.2d] \cdot \pi 90^{-1} \quad (8)$$

If the total length of the butt weld is  $C = \pi d$ , and  $k=1.2$ , then for a vessel with  $d=200$  mm,  $t=10$  mm, the number of transilluminations can be calculated from equation (8) to be  $n=3$ , which ensures that there is certain amount of overlap at the joints. Under the same conditions, for a vessel with  $d=100$  mm,  $t=10$  mm,  $n$  is calculated to be 4.

For a vessel with small outer diameter and large wall thickness, even though the calculated number of transilluminations is still accurate, the image of the upper butt weld may not be able to meet sensitivity requirements because it is too far from the negative. In this case, the segmented measurement method must be used.

The so-called segmented measurement method consists of building a penetrometer which meets the 2 percent sensitivity requirement; it is constructed using 11 stainless steel wires which are 20 mm long and separated by 5 mm, and it is covered with foam rubber to allow easy bending. After normal exposure and dark room processing, one can calculate the length of each transillumination  $L$  and the number of transilluminations  $n = \frac{C}{L}$  by measuring the distance between the metal wires at the farthest edge of the negative. In order to accommodate vessels of different thicknesses, several sets of penetrometers were constructed using wire sizes ranging from  $\phi 0.1$ - $0.4$  mm. The penetrometers can be attached using adhesive paper. They should be attached to both the upper and lower butt welds to provide close monitoring of transillumination sensitivity. For a vessel with  $d=200$  mm,  $t=10$  mm as in the above example, the segmented method of measurement requires  $n=3$  to achieve 100 percent transillumination; for a vessel with  $d=100$  mm,  $t=10$  mm, it requires  $n=5$  to achieve 100 percent effective inspection and to ensure certain amount of overlap at the joints of the negatives. This result illustrates that the segmented measurement method is basically consistent with the calculation method. If the image of the upper butt weld cannot meet sensitivity requirement, one should use the result of the segmented measurement method.

Fig. 6 and Fig. 7 show the elliptical images of the butt welds of two vessels with different wall thicknesses. It can be seen from Fig. 7 that the butt weld has two chain-shaped air bubbles.



Fig. 6 Elliptical Image of the Butt Weld

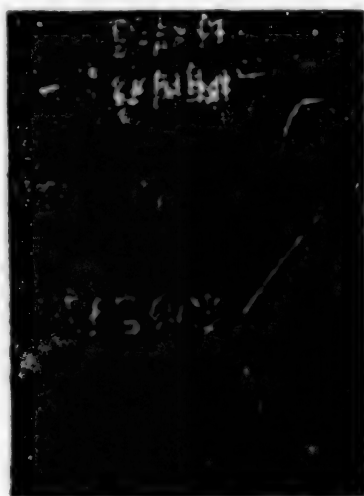


Fig. 7 Chain-Shaped Air Bubbles

Recently, we performed an experiment of inspecting the butt welds of a small spherical thick-wall vessel with the model XY-1520 X-ray machine. This machine was assembled by the Dandong Instrument Factory using the MCN161 beryllium window metal-ceramic tubes produced by the Philips Co of Holland. The experiment was conducted under the condition where the film, the intensifying screen and the X-ray angle of incidence remained unchanged. Because of the small size of the focal point of this device (typical focal point is  $3 \times 3 \text{ mm}^2$ ), it follows from the formula of geometric unclarity:  $U_g = t \cdot F / f$  ( $U_g$  is the geometric half image,  $t$  is the thickness of the article,  $F$  is the dimension of the focal point, and  $f$  is the focal distance) that when  $F$  is reduced, the focal distance  $f$  can be reduced accordingly without changing the value of  $U_g$ . The experiment

showed that for a vessel with wall thickness of 10 mm (i.e., penetrating a double wall thickness of 20 mm), tube voltage of 130 KVP, tube current of 20 mA, and focal distance of 600 mm, satisfactory transillumination results were obtained with 6 minutes of exposure time, and the inspection sensitivity was increased to approximately 1.5 percent.

3012

CSO: 4008/314



THERMOPHYSICAL PROPERTIES OF MATTER

Shanghai ZIRAN ZAZHI [NATURE JOURNAL] in Chinese No 1, 1984 pp 28-29

[Excerpt] Research on thermophysical properties in China began in the mid-1950's when room temperature thermal conductivity measurements were made in universities and research units. In the early 1960's more resources were devoted to large-scale thermophysical properties research. Due to the urgent demands of national economic construction and particularly of defense construction, the State Science and Technology Commission established some research institutes and high temperature measurement bases at participating universities. These organizations planned the research and assigned research tasks on thermophysical measurements. Scientific research resources in China were organized and measurement methods and facilities for thermal conductivity and specific heat were established for different temperature ranges. The first high temperature annual symposium was held in 1961 and made a good start for China's thermophysical properties study. In the past 20 years China has made considerable progress in thermophysical research and has formed a science and technology rank of substantial quantity and quality. One important goal was to satisfy the timely needs of thermophysical properties data and testing techniques in China's aviation, aerospace and nuclear technology development.

On the whole, however, there is still a considerable gap between China's thermophysical research level and the international standard. Many weak links need to be strengthened and many voids need to be filled. In the author's opinion, we should pay attention to problems in the following six areas:

1. In contrast to the testing technology of thermophysical properties, the breadth and depth of the research on thermophysical mechanism, variation and parameters are relatively weak. This has not only impeded the in-depth development of the thermophysical properties science but also the progress of other scientific disciplines.
2. In contrast to the thermophysical testing methods and devices for solid matter, the study of fluid media is weak and the study of the thermophysical properties of gases is almost nonexistent.

3. In contrast to the conventional or specialized measurement techniques, the serialization and particularly the standardization (including standard samples) of thermophysical measurement techniques and equipment are still in the development or planning stages. Although tentative ministry-level standards for certain thermophysical measurements have been established, a national standard has not. As a result, the thermophysical properties data in China (especially for thermal conductivity) vary from research unit to research unit and sometimes with large discrepancies.

4. Although the research units in China have accumulated a great amount of thermophysical properties data on Chinese-made materials, China still does not have her own thermophysical properties handbook encompassing all the solid materials. (The responsible unit is in the process of compiling a thermophysical properties handbook for metallic materials.) Although a thermophysical properties data center and a data bank are being established, the amount of manpower and material resources devoted to this task is inadequate and cannot quickly satisfy the urgent need.

5. If thermophysical properties research in the past is considered closely tied to the development of defense and frontier science and technology, then we still need to strengthen the connection between energy technology and other industrial departments. For example, the development and production of heat insulation material for energy conservation basically was not guided by the principles of thermal insulation and thermal design, and neither were the application parameters optimized by thermophysical properties principles.

6. We must create a conducive environment and actively establish China's research center for thermophysical parameters. China's research and application of thermophysical properties must be promoted on two fronts: experimental study based on scientific theories and measurement techniques.

9698

CSO: 4008/175

PILOT MODEL TEST FOR BITUMINIZATION OF CONCENTRATED RADIOACTIVE WASTES USING CONTINUOUS TURBULENT FILM EVAPORATOR

Beijing HE KEXUE YU GONGCHENG [CHINESE JOURNAL OF NUCLEAR SCIENCE AND ENGINEERING] in Chinese Vol 3, No 2, Jun 83 pp 142-152

[Article by Li Dongcai [2621, 2767, 2088] of Beijing Institute of Nuclear Reactor Engineering: "An Expanded Cold Pilot-Model Test for Bituminization of Concentrated Radioactive Liquid Wastes Using Turbulent Film Evaporator"; manuscript received 14 July 1982]

[Text] Abstract

The emphasis of the paper was placed on the introduction to the selection of technological parameters in the bituminization process using continuous turbulent film evaporators, the verification experiments on various medium and low level radioactive cold model waste liquids, the test of the flow process and the equipment during continuous operation, the decontamination method of the bituminization equipment and recovery of the decontaminant, and the measurement of thermal stabilities of various bituminized wastes, etc.

I. Introduction

China began the technological study of bituminization of radioactive liquid wastes from 1969; starting with small-scale hot and cold tests as well as some basic research. Expanded cold model tests for bituminization of low and medium level radioactive concentrated liquid wastes using continuous turbulent film evaporators began in 1975. The accomplishments of research have already been applied to engineering constructions.

II. Brief Introduction to Technological Process and Equipment

2.1 Brief Introduction to Technological Process

See Figure 1. A 200l barrel of No 60 asphalt is heated to melt in a furnace (at temperatures above 100°C). It is then dehydrated by flowing through a dehydration tank (temperatures around 130°C). The impurities in the asphalt

- 0- Liquid level indicator
- 0+ Resistance thermometer
- Vacuum gauge
- Kotometer
- Glass thermometer
- Glass liquid level indicator
- Steam trap
- 1 Pipe filter
- 2 Asphalt gear pump

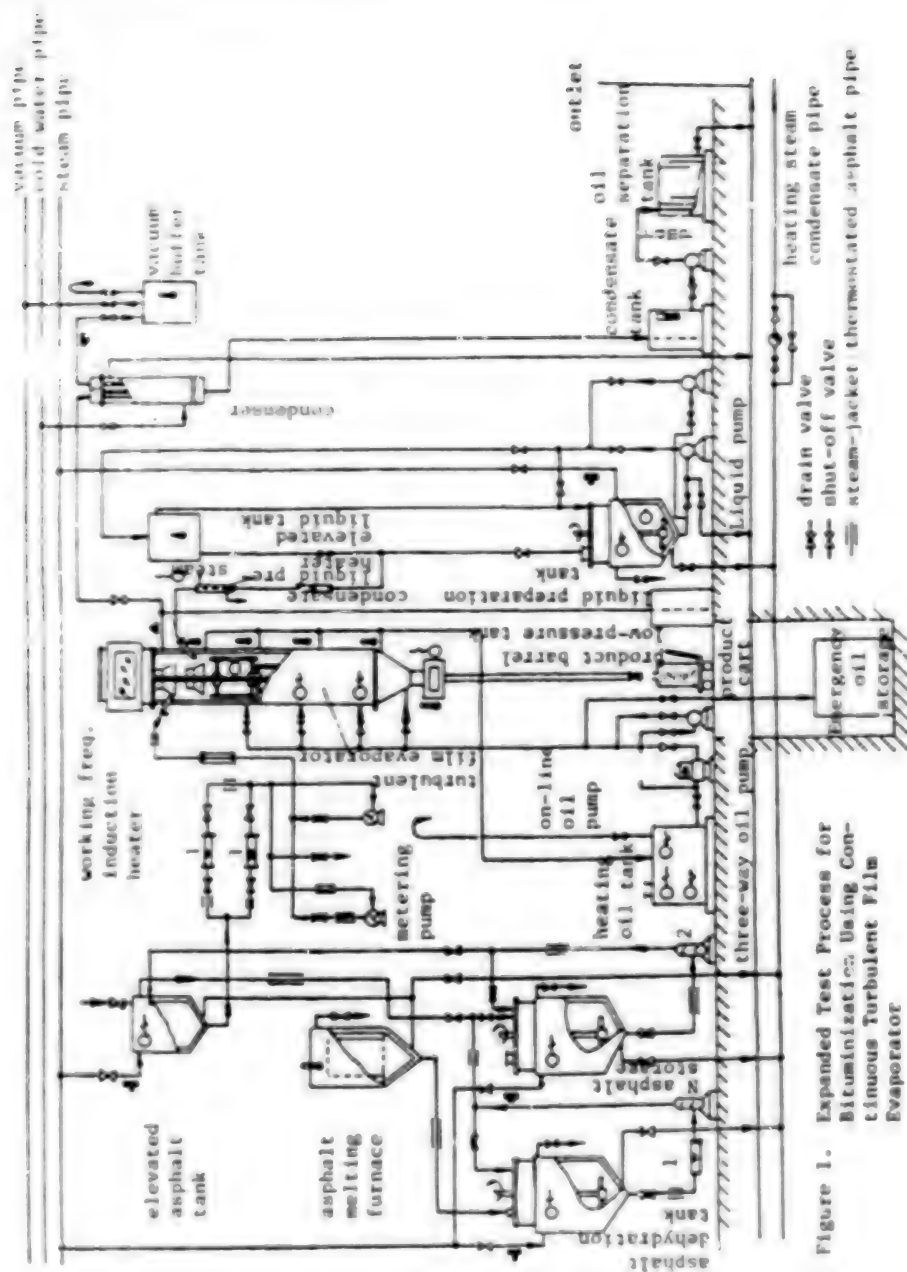


Figure 1. Expanded Test Process for Bituminization Using Continuous Turbulent Film Evaporator

are removed by a filter, and it is sent into an asphalt storage tank by a pump. The asphalt is again delivered by another pump to an elevated asphalt tank for use. When this material is fed, another filter is used to further remove the impurities. It is delivered at a fixed rate by a metering pump to an induction heater to be rapidly heated to 170-180°C. Then it flows into the distribution plate of the turbulent film evaporator. The solution is prepared in the solution preparation tank and then delivered to an elevated tank for use by a pump. Through a flowmeter, this liquid enters a pre-heater to be heated to around 95°C. Then, it enters the lower distribution plate of the turbulent evaporator.

The turbulent evaporator is pre-heated to 100°C before the scraper motor can be turned on and the rotating speed is adjusted to the specific value. Only when the wall temperature of the turbulent evaporator reaches above 200°C, then the test liquid can be added. Asphalt is first added for over 5 minutes, then the test liquid is delivered. When stopping, the liquid is stopped first before asphalt is turned off to prevent scab formation on the wall surface. When the scraper is operating, asphalt is thrown to the heated wall of the turbulent evaporator from the distribution plate by centrifugal force. A thin film less than 1.5 mm thick with a continuously renewed surface is formed by the rotating scraper. When liquid is added, it is thrown from the lower distribution plate to the asphalt film, and is thoroughly mixed with the asphalt by the vigorous stirring of the rotating scraper. The film is continuously renewed and the liquid is dehydrated by absorbing the required heat of vaporization from the heated surface. The mixture moves towards the outlet on the surface of the evaporator in a spiral by gravity. As it reaches the outlet, it becomes a qualified bituminized product. The product can flow away by itself, or it can be delivered continuously under a sealed atmosphere by a triple element rotor pump (process not shown) to ensure the continuous operation of the evaporator at a certain negative pressure.

The secondary steam generated in the turbulent evaporator is cooled to 20-30°C by a condenser. It flows automatically into a condensate tank (maintaining a 7m water column seal). Periodically, the condensate, which contains a minute amount of oil, is delivered to an oil separation tank by a water pump to remove the oil. It is then discharged into the sewer system. The turbulent evaporator is heated by using over heated No 38 engine oil. The oil is heated by 40 kW electric heating element in the heating tank. Heated oil is used to heat up the turbulent evaporator by circulating with an on-line oil pump and a three-way oil pump. The heating temperature is around 200-230°C.

## 2.2 Brief Introduction to Turbulent Evaporator

Look at Figure 2. Turbulent evaporators are suited for continuously concentrating high viscosity, heat sensitive, and easily foaming matters. Furthermore, the heat transfer efficiency is relatively high, and the duration of stay for the materials in the equipment is only a few minutes. It is appropriate to be used to treat highly viscous and heat sensitive bituminized wastes. The following problems should be noticed in the design:

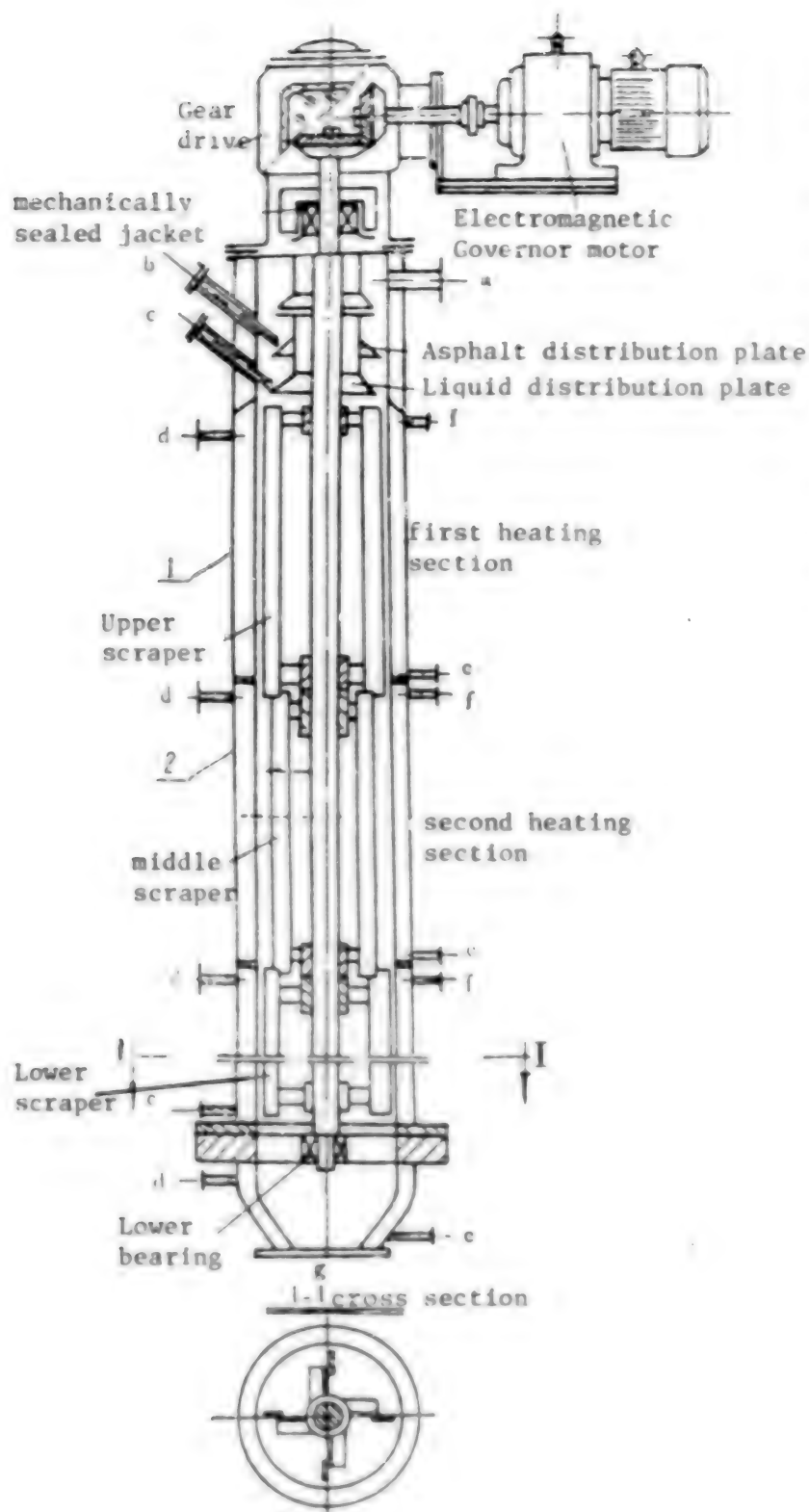


Figure 2.

Schematic Diagram of the Structure of the Turbulent Film Evaporator

- a. secondary steam outlet
- b. asphalt inlet
- c. liquid inlet
- d. oil outlet (or steam inlet)
- e. oil inlet (or cooling water outlet)
- f. uncondensed gas exhaust
- g. bituminized product outlet



1. Select a suitable aspect ratio (usually 4-6). The longer the axle is, the higher the strength requirement becomes. Requirements in material selection, processing and surface heat treatment are also more complicated. A small value should be adopted in the design, to the extent possible.
2. It is required that the scraper axle have high strength and small deformation. The surface must be heat treated in nitrogen. It must qualify both the static and dynamic tests.
3. The product outlet must be placed properly to prevent blockage. This modified turbulent evaporator (i.e., as shown in Figure 2) was stable and reliable after placed in operation. Furthermore, it had been tested under special environmental conditions.

### III. Types of Bituminized Wastes

No 60 asphalt from Nanjing Refinery was selected for use in the experiment. The types and major compositions of liquid wastes studied experimentally are shown in Table 1.

### IV. Discussion of Experimental Results

#### 4.1 Selection of Operating Parameters of Turbulent Evaporator

##### 1. Optimum Salt Content of Bituminized Material

It was proven experimentally that the optimum salt content is 40-50 percent (wt). The experimental data is shown in Table 2.

##### 2. Allowable Range of Scraper Rotating Speed

Experimental results showed that the product was mixed homogeneously at a high rotating speed. Dehydration was thorough and leaching rate was low. However, an excessively high speed can easily cause vibration of the scraper, increasing power consumption, and accelerate the wearing and tearing of the bearing. At a low speed, however, the tendency of poor dehydration increases.

##### 3. Degree of Vacuum in Turbulent Evaporator

Experiments showed that dehydration capability was low at the normal pressure, and the water content in the product was high. It is appropriate that the vacuum is not less than 50 Torr, as shown in Table 3. From the table one knows that the higher the vacuum is, the larger the amount of salts and oil in the secondary steam will remain; which lowers the purification coefficient. Therefore, a suitable vacuum must be selected for the operation.

##### 4. Product Temperature

When the product temperature is too low, the water content is too high, leaching rate is large, and fluidity is so poor that the exit may be clogged. When the product temperature is too high, energy consumption is increased.

Table 1. Chemical Compositions of Cold Model Liquid Wastes and Types of Waste Water

Liquid Number	Major Composition*	Waste Water Type
1.	30-34%(wt) $\text{NaNO}_3$ , pH = 10 - 13, salt content about 463 (prepared with industrially pure $\text{NaNO}_3$ ).	low-level radioactive waste water
2.	$\text{NaCO}_3$ : 5.25, $\text{Na}_2\text{C}_2\text{O}_4$ : 13.5, $\text{NaOH}$ : 3.38 $\text{NaNO}_3$ : 43.27, $\text{Na}_2\text{SO}_4$ : 10.5, $\text{Mg}(\text{OH})_2$ : 1.78, $\text{Ca}_3(\text{PO}_4)_2$ : 2.35, $\text{CaCO}_3$ : 11.1, petroleum sulfonic acid: 7.5, detergent: 2.3, defoaming agent (dipropanol butyl ethyl epoxy ester) = 10, and others 15. Mixture salt content at about 120, pH adjusted to 10-13.	low-level radioactive waste water (1:1 mixture of floor washing water and waste laundry water).
3.	Chemical slurry crudely prepared in a rapid settling vessel by adding reagents such as $\text{Fe}_2(\text{SO}_4)_3$ , $\text{Na}_3\text{PO}_4$ , $\text{NaOH}$ , $\text{KMnO}_4$ , $(\text{NaPO}_4)_6$ , etc into waste water No 2, total salt 20-30, total salt in concentrated slurry after freeze-pump-thaw filtering around 100, pH adjusted to = 10-13.	low-level radioactive chemical slurry
4.	$\text{NaNO}_3$ : 314, $\text{KNO}_3$ : 0.103, $\text{Fe}_2(\text{SO}_4)_3$ : 32, $\text{Nn}(\text{NO}_3)_2$ : 0.154, $\text{NHO}_3$ : 63, using $\text{NaOH}$ to adjust pH = 12, salt content in waste water around 430.	acidic medium level radioactive waste water
5.	$\text{NaAlO}_2$ : 82, $\text{NaNO}_3$ : 61.5, $\text{NaOH}$ : 31.5, $\text{Na}_2(\text{O}_3\text{O } 9)$ , waste water salt content about 235, actually measured alkalinity 2.3N.	medium-level radioactive waste liquid discharged from the shell
6.	Mixing 1# + 3#, volume ratio 1#:3# = 1:0.635 (chemical slurry with salt content 26.5), mixture liquid salt content around 337, pH adjusted to = 10-13.	low-level mixed waste water
7.	Mixing 1# + 3#, volume ratio 1#:3# = 1:0.21 (freeze-pump-thaw filtered slurry), liquid mixture salt content around 285, pH adjusted to $\frac{1}{2}$ 13.	low-level radioactive mixed waste water

Table 1. Continued

8.	Mixing 1# + 2#, volume ratio 1#:2# = 1:0.25 (1# salt content 450, 2# 120), mixture salt content about 380, pH adjusted to = 10-13.	low-level radioactive mixed waste water
9.	Mixing 1# + 2# + 3#, volume ratio 1#:2#:3# = 1.0:0.41 : 0.9 (1# salt content 300, 2# 120, and 3# 30), liquid mixture salt content about 145, pH adjusted to = 10-13.	low-level radioactive waste water mixed with reagents
10.	Mixing 4# + 5# + 1# (i.e., absorbed acidic and basic waste water): volume ratio 4#:5#:1# = 0.4:1:3.6 (4# salt content 422, 5# 322, and 1# 520), mixed waste water salt content 480, pH adjusted to = 10-13.	medium-level radioactive waste water mixed with reagents
11.	Mixing 17# + 4# + 1# (basic waste water neutralizing agent): volume ratio 17#:4#:1# = 1:0.255:2.3, mixed waste water salt content 480, pH adjusted to = 10-13.	medium-level radioactive waste water mixed with reagents
12.	Mixing absorbing solutions: acidic absorbing solution-citric acid 2%(wt), ammonium citrate 5%(wt), EDTA 0.5%(wt), water 92.5%(wt). Basic absorbing solution - NaOH 10%(wt), $\text{KMnO}_4$ 3%(wt), water 87%(wt). Mixing volume ratio 1:1, concentrated one time by distillation, liquid mixture salt content about 256, pH adjusted to = 9.24.	low-level radioactive mixed waste water
13.	12# = boron containing waste water (mixing $\text{H}_3\text{BO}_3$ :316 with NaOH:203), volume ratio 1:1, liquid mixture salt content about 540, pH adjusted to = 13.	low-level radioactive waste mixed with reagents
14.	Nitric acid waste water: $\text{Mg}(\text{NO}_3)_2$ :247, $\text{Ca}(\text{NO}_3)_2$ :45, $\text{Ba}(\text{NO}_3)_2$ :9.5, $\text{HNO}_3$ 13Bm after OG adhysted ti = 9- 11, liquid mixture salt content around 500.	low-level radioactive waste water

Table 1. continued

15.	Mixed acid waste water: $\text{HNO}_3$ :11N, $\text{HCl}$ :5N, pH adjusted to = 11.6, waste water salt content about 446	low-level radioactive waste water
16.	14# + 15# + chemical slurry ( $\text{Fe}_2(\text{SO}_4)_3$ :0.8, $\text{KMnO}_4$ :0.4, using NaOH to adjust pH to = 9-11, slurry salt content about 23), volume ratio:14#:15#:chemical slurry = 1:1:4, mixed liquid salt content about 276, pH adjusted to = 9.1.	low-level radioactive waste mixed with reagents
17.	$\text{NaAlO}_2$ + $\text{Na}_2\text{CO}_3$ waste water: $\text{NaAlO}_2$ :193.7, NaOH:146, $\text{Na}_2\text{CO}_3$ :85.6, pH adjusted to = 10-13, total salt 480.	medium-level radioactive mixed waste water

\*Unit of salt concentration is g/l.

(1) 固化物平均含盐率 (%wt)	(2) 平均浸出率* (1-16天对 $\text{Na}^+$ ) (g/cm <sup>2</sup> ·d)	(3) 沥青固化物软化点 (°C)	(4) 沥青固化物平均含水率 (%wt)	(5) 备 注
41.80	$0.88 \times 10^{-4}$	63.7	0.20	(6) 产品流动性好, 表面光亮, 盐份分布均匀, 蒸发器运行平稳, 出料顺畅。
48.30	$1.18 \times 10^{-4}$	68.8	0.63	
51.70	$1.15 \times 10^{-4}$	69.3	0.28	
57.85	$1.00 \times 10^{-4}$	71.4	1.10	(7) 产品流动性差, 表面粗糙, 盐粉分布不均, 蒸发器面有时结疤, 出料口堵塞及刮板短时震动。
57.80	$4.65 \times 10^{-4}$	78.3	1.03	
59.60	$13.68 \times 10^{-4}$	81.7	0.85	

(8) 文中浸出率, 指固化物在蒸馏水中, 静态浸泡 1—16 天, 每天取样测定  $\text{Na}^+$  浓度的平均值。

Table 2. Effect of Salt Content in Bituminized Material on Part of the Product Characteristics (No 1 liquid)

- average salt content in bituminized material (% wt)
- average leaching rate\* (1-16 days with respect to  $\text{Na}^+$ ) (g/cm<sup>2</sup>·d)
- softening point of bituminized material (°C)
- average water content in bituminized material (%wt)
- remarks
- good fluidity, shining surface, homogeneous salt distribution, evaporator operating stably, product moving smoothly
- poor fluidity, rough surface, uneven salt distribution, scab formation on evaporator wall surface at times, blockage of product outlet, short-term vibration of scraper

Table 2 continued:

8. \*The leaching rate given in the paper is the average  $\text{Na}^+$  concentration measured during daily sampling when the bituminized material was soaked in distilled water for 1-16 days statically.

(1) 绝对真空度 (Torr)	(2) 含水量 (%wt)	(3) 温度 (°C)	(4) 加量 (l/h)	(5) 二次蒸汽冷凝液 盐, 油含量 (6) 盐 (mg/l) (7) 油 (mg/l)		(8) 备注
(10) 0 (真空)	11.69	130-161	24-27	—	22.0	(9) 用1号料液试验
10	0.72	144-172	24	29.2	24.9	
87-120	0.46	140-160	24	31.2	23.6	
110	0.16	135-180	24-30	124.5	62.9	

Table 3. Effect of Vacuum Turbulent Evaporator on Water Content in Products

Key:

1. vacuum in turbulent evaporator (Torr)
2. average water content in bituminized material (%wt)
3. product exit temperature (°C)
4. liquid feeding rate (l/h)
5. salt and oil contained in secondary steam condensate
6. salt (mg/l)
7. oil (mg/l)
8. remarks
9. tested using No 1 liquid
10. normal pressure

It may even cause the dissociation of salts and lead to the danger of explosion. The appropriate product exit temperature is 160-180°C.

#### 5. Optimum Productivity of Turbulent Evaporator

The optimum productivity was obtained under the following conditions: scraper rotating speed 850 rpm, bituminized salt content 45 percent (wt) vacuum 100 Torr, liquid 40 percent  $\text{NaNO}_3$  (pH = 10-13), oil temperature 220-230°C, and water content in bituminized product < 0.5 percent (wt). It was proven experimentally that the optimum productivity of the turbulent evaporator was only 40 l/m<sup>2</sup>.h when heated with No 38 engine oil.

#### 4.2 Cold Test With Engineering Model Liquid and Evaluation of Continuous Operation of the Process.

Bituminization tests on the 13 waste liquids listed in Table 1 were performed separately in a turbulent evaporator. Qualified products can always be obtained as long as the operating conditions are appropriate, which indicates that a turbulent evaporator is highly adaptable to various types of waste water. Results are shown in Table 4.

No 1 liquid was used in a continuous operation for 180 hr to evaluate the reliability of the technological process. A total of 6500 l of 40 percent  $\text{NaNO}_3$  solution was treated, and 5500 l of bituminized product was obtained. Together with 300 hours of intermittent batch process tests, results indicated that the turbulent evaporator was operating normally without apparent vibration, blockage and scab formation. After the test was completed, it was observed that there was a 0.5-1.0 mm thick gray bituminized salt scale on the middle and lower portion of the heated wall. Because the scraper gap was 15.0 mm, therefore, it did not affect the operation (but affected heat transfer). The data is shown in Table 5.

#### 4.3 Decontamination Method of Bituminization

Because a bituminized salt scale will form on the solidifying surface and moving parts of the evaporator, a good decontaminant must be used to wash it away in order to ensure heat transfer and safety. Now, the results of decontamination study are summarized in the following:

1. Selection of Decontaminant. Twelve decontaminants were tested. We recommend the use of industrially pure trichloroethylene as the decontaminant after making our selection.

2. Decontamination of Turbulent Evaporator. A salt scale was first formed by nearly 20 hours of bituminization of No 9, 12, 15, 16 liquids. Trichloroethylene was then added. The decontaminant was drained after 24 hours of static soaking. The equipment surface was completely decontaminated and restored after a 10 minute static soaking by hot water at 90-100°C. The decontamination effect would be even better if it is done dynamically (i.e., with scraper revolving).





Key to Table 4:

- |  |   |
|--|---|
| 1. liquid number   | 16. condensate  |
| 2. liquid  | 17. upper section (°C)  |
| 3. asphalt   | 18. middle section (°C)   |
| 4. operating parameters of turbulent evaporator                                | 19. lower section (°C)  |
| 5. analysis of samples of bituminized materials and secondary steam condensate | 20. average water content (% wt)                                      |
| 6. flow rate (l/h)   | 21. average softening point (°C)                                      |
| 7. incoming material temperature (°C)  | 22. average salt content (% wt)                                       |
| 8. flow rate (l/h)   | 23. average leaching rate ( $\times 10^{-4}$ ) (g/cm <sup>2</sup> -d) |
| 9. incoming material temperature (°C)  | 24. salt content (mg/l)   |
| 10. heated wall temperature  | 25. oil content (mg/l)  |
| 11. heating oil temperature (°C)   |   |
| 12. vacuum (Torr)  |   |
| 13. secondary steam exit temperature (°C)                                      |   |
| 14. bituminized product exit temperature (°C)                                  |   |
| 15. bituminized material   |   |

Note: scraper revolving speed is 850 rpm

\*The alkalinity of the  $\text{NaAlO}_2$  waste water was 2.3N, which made dehydration very difficult. In addition, the product exit temperature was low. Therefore, the water content was high. If pH is adjusted to <1.3, then the product will qualify.

Table 5. Summary of Parameters and Data Analysis for Turbulent Evaporator in Continuous Operation

(1) 运行 时间 连续 运行 (h)	(2) 渣 (6) 量 (t/h)		(3) 渣 (8) 量 (t/h)		(4) 刮板蒸发器运行参数			(5) 沥青固化物及二次蒸汽冷凝液取样分析值			(25) 渣 (25) 油 (mg/l)	
	(7) 渣 温度 (°C)	(9) 渣 温度 (°C)	(10) 渣 温度 (°C)	(11) 渣 温度 (°C)	(12) 真空 度 (Torr)	(13) 出口 温度 (°C)	(14) 出口 温度 (°C)	(15) 沥青 固化 物 (%wt)	(16) 渣 温度 (°C)	(17) 渣 温度 (°C)	(18) 渣 温度 (°C)	(19) 渣 温度 (°C)
50.00	95	19.2	146	140	100	100	159	1.30	63.5	42.3	0.28~2.8	62~140
54.00	80	33.0	140	140	100	100	137	3.10	61.0	33.7	0.87~3.20	138
56.00	60	19.2	148	135	100	130	165	0.21	62.9	30.3	0.64~4.00	305
61.00	62	16.8	150	143	100	101	172	0.21	62.7	35.8	0.81~4.00	165
65.33	86	19.2	147	138	100	101	136	2.00	67.8	40.0	8.00~16.00	133
73.00	102	19.2	142	140	102	100	165	0.31	68.4	37.0	1.50~5.30	—
82.00	75	19.2	148	157	50	103	165	0.29	70.1	50.0	3.40~5.80	—
90.00	94	19.2	144	140	50	104	184	0.29	63.7	36.7	0.28~1.70	—
92.66	82	19.2	142	152	50	103	178	0.15	73.2	50.9	2.66	—
100.00	85	19.2	146	152	50	104	172	0.18	69.8	45.1	2.12	—
105.00	100	19.2	145	137	100	100	167	0.36	67.8	46.6	1.90	—
113.00	98	19.2	144	139	100	102	170	1.20	64.4	47.0	2.00	—
118.00	86	19.2	148	139	100	102	169	0.88	65.3	43.9	2.10	—
125.00	94	19.2	147	137	50	105	158	1.35	63.0	45.3	2.10	—
129.00	80	19.2	146	140	100	102	170	0.60	65.9	44.4	—	—
135.30	90	15.6	140	152	50	105	165	1.50	69.9	44.5	—	—

Key:

1. cumulated continuous operating time of the scraper
2. liquid
3. asphalt
4. operating parameters of turbulent evaporator
5. analysis on samples of bituminized material and secondary steam condensate
6. flow rate (l/h)
7. incoming material temperature (°C)
8. flow rate (l/h)
9. incoming material temperature (°C)
10. heated wall temperature
11. heating oil temperature (°C)
12. vacuum (Torr)
13. secondary steam exit temperature (°C)

Key continued on following page.

Table 5 Key continued:

14. bituminized product exit temperature (°C)	20. average water content (% wt)
15. bituminized material	21. average softening point (°C)
16. condensate	22. average salt content (°C)
17. upper section (°C)	23. average leaching rate ( $\times 10^4$ ) (g/cm <sup>2</sup> d)
18. middle section (°C)	24. salt content (mg/l)
19. lower section (°C)	25. oil content (mg/l)

Note: No 1 liquid was chosen in the experiment. The scraper revolving speed was 850 rpm.

\*The leaching rate is with respect to  $\text{Na}^+$ . The specimens were soaked in distilled water statically for 1-15 days. Samples were taken daily for analysis.

Table 6. Differential Thermal Gravimetric Analysis of  $\text{NaNO}_3$  Bituminized Products at Various Alkalinities

(1) 沥青固化物中 NaOH 含量 (%wt)	(2) 沥青固化物中 $\text{NaNO}_3$ 含量 (%wt)	DTA		TG	
		起始放热温度 (3) (°C)	放热峰值温度 (4) (°C)	起始失重温度 (5) (°C)	最大失重温度 (6) (°C)
$7 \times 10^{-5}$ (料液 pH = 9) (7)	40	270	342	230	320
0.4 ( = 0.1N)	50	277	364	240	325
1.2 ( = 0.3N)	50	197	340	210	320
2.0 ( = 0.5N)	50	184	347	200	312
2.8 ( = 0.7N)	50	182	327	180	300
4.0 ( = 1N)	50	146	317	150	305
8.0 ( = 2N)	50	167	332	170	295

Key:

1. NaOH content in bituminized products
2.  $\text{NaNO}_3$  content in bituminized products
3. initial exothermic temperature (°C)
4. peak exothermic temperature (°C)
5. initial weight loss temperature (°C)
6. maximum weight loss temperature (°C)
7.  $7 \times 10^{-5}$  (solution pH = 9)

3. Recovery of Trichloroethylene Decontaminating Solution. The original turbulent evaporator process is used to recover the decontaminant. Because industrially pure trichloroethylene contains 5 percent tetrachloroethylene, it will decompose and release a small amount of HCl upon contact with a hot surface over 125°C. Therefore, the recovery consists of two boiling processes: trichloroethylene (boiling point 86.7°C) is recovered at 85-95°C, and tetrachloroethylene (boiling point 120.5°C) is collected at 95-135°C. The same receiving tank can be used because the decontaminating effect is the same. The recovery rate in a small scale still is 92.7-96.1 percent. Using a turbulent evaporator, the recovery rate is 88 percent. The softening point of the distillation residue is higher than 59°C. Furthermore, it possesses the characteristics of a bituminized product and can be directly stored in a barrel without further processing.

#### 4.4 Study of Thermal Stability of Bituminized Wastes

Experimental results showed that the bituminized product of  $\text{NaNO}_3$  has an apparent spontaneous exothermic reaction when the temperature reaches around 250°C. If heat is allowed to accumulate so that the temperature reaches the spontaneous combustion point ( $>300^\circ\text{C}$ ), explosion may occur. In order to obtain a reliable and safe operating temperature, it is necessary to study the thermal stability of various bituminized products. An accurate differential thermal balance was used to measure TG and DTA curves of various bituminized products. In the meantime, a constant temperature measuring device for larger specimens was developed to determine the initial exothermic temperatures of various bituminized products. The reproducibility of this device is very good for testing the thermal stability of a mixture. Because a sample can be as large as several kilograms, it is highly representative and the reaction is objective. It is a dependable technique. The experimental results are shown in Tables 6 and 7.

From Tables 6 and 7 one knows that the salt content has little effect on the initial reaction temperature. However, the effect of alkalinity on initial reaction temperature is apparent. When the solution  $\text{pH} > 13$ , the initial reaction temperature decreases apparently with increasing alkalinity. Therefore, it is safe to proceed with bituminization at  $\text{pH} < 13$ .

#### V. Conclusions

##### 5.1 Basic Characteristic Indicators of Bituminized Products

1. Average salt content in bituminized waste:  $45 \pm 5\%$  (wt);
2. average water content in bituminized waste:  $<0.5\%$  (wt);
3. average softening point of bituminized waste: approximately  $70^\circ\text{C}$ ;
4. average salt grain size in bituminized waste:  $d = 5-8 \mu\text{m}$ ;
5. average leaching rate of bituminized waste (1-17 days with respect to  $\text{Na}^+$ ): approximately  $10^{-4} \text{g/cm}^2 \cdot \text{d}$ ;





Key to Table 7.

1. testing institution
2. Institute of Non-ferrous Metallurgy
3. Beijing Institute of Aeronautics and Astronautics
4. Dalian Chemical Physics Institute
5. Ministry of Nuclear Industry 1
6. Ministry of Nuclear Industry 1
7. Ministry of Nuclear Industry 2
8. material or liquid number
9. test method
10. DTA initial exothermic temperature ( $^{\circ}\text{C}$ )
11. TG initial weight loss temperature ( $^{\circ}\text{C}$ )
12. DTA initial exothermic temperature ( $^{\circ}\text{C}$ )
13. DTA initial exothermic temperature ( $^{\circ}\text{C}$ )
14. TG initial weight loss temperature ( $^{\circ}\text{C}$ )
15. DTA initial exothermic temperature ( $^{\circ}\text{C}$ )
16. TG initial weight loss temperature ( $^{\circ}\text{C}$ )
17. initial exothermic temperature measured with 1 Kg of bituminized specimen at constant temperature ( $^{\circ}\text{C}$ )
18. initial exothermic temperature 2 Kg of bituminized specimen measured at constant temperature ( $^{\circ}\text{C}$ )
19. remarks
20. 3.5 h at  $240^{\circ}\text{C}$  constant temperature, obviously exothermic ( $+18^{\circ}\text{C}$  above oil temperature)
21. bituminized products contain 40-50% (wt) salt
22. 8 h at  $230^{\circ}\text{C}$  constant temperature, obviously exothermic ( $+5^{\circ}\text{C}$  above oil temperature)
23. 7 h at  $210^{\circ}\text{C}$  constant temperature, obviously exothermic ( $+5^{\circ}\text{C}$  above oil temperature)
24. 4.5 h at  $250^{\circ}\text{C}$  constant temperature, spontaneously combusted ( $8^{\circ}\text{C}$  lower than oil temperature due to a shifting thermometer)
25. 7 h at  $240^{\circ}\text{C}$  constant temperature, obviously exothermic ( $+3^{\circ}\text{C}$  over oil temperature)
26. analytical instruments: (1) Institute of Non-Ferrous Metallurgy used a domestic Model 4-1-C-1 differential thermal analyzer. (2) Beijing Institute of Aeronautics and Astronautics used a domestic Model CDR-1 dynamic differential thermal analyzer. (3) Dalian Chemical Physics Institute used a Daojing Model DT-2A (Japan) automatic recording differential thermal analyzer. (4) Ministry of Nuclear Industry 1 used a domestic Model 4.1 automatic recording precision differential thermal balance. The home-made large specimen constant temperature device was used for constant temperature measurements.

27. 2 h at 230°C constant temperature, obviously exothermic (+18°C above oil temperature)
28. 12 h at 230°C constant temperature, no exotherm (0°C over oil temperature, i.e., equilibrium)
29. 3 h at 250°C constant temperature, obviously exothermic (+16°C over oil temperature)
30. spontaneous combustion after 4 h at 250°C constant temperature (spontaneous combustion after +14°C over oil temperature)
31. 8 h at 240°C constant temperature, obviously exothermic (+4°C over oil temperature)
32. 7.5 h at 240°C constant temperature, obviously exothermic (+11°C over oil temperature)
33. 5.5 h at 260°C constant temperature, obviously exothermic (+10°C over oil temperature)
34. 5.5 h at 250°C constant temperature, obviously exothermic (+4°C over oil temperature)
35. 3 h at 260°C constant temperature, obviously exothermic, product combusted spontaneously (occurred at +2°C above oil temperature)
36. 5.5 h at 240°C constant temperature, slightly exothermic (+1°C above oil temperature)
37. 10 h at 260°C constant temperature, no exotherm (7°C lower than oil temperature)
38. 5 h at 260°C constant temperature (+10°C above all temperature)
39. 7 h at 260°C constant temperature, product spontaneously combusted (occurred after 10°C above oil temperature)
40. 8 h at 260°C constant temperature, no exotherm (2°C above oil temperature)
41. 7.5 h at 260°C constant temperature, obviously exothermic (+11°C above oil temperature)
42. pure No 60 asphalt
43. 8 h at 230°C constant temperature, no exotherm (20°C lower than oil temperature)
44. 2 h at 260°C constant temperature, no exotherm (6°C below oil temperature).

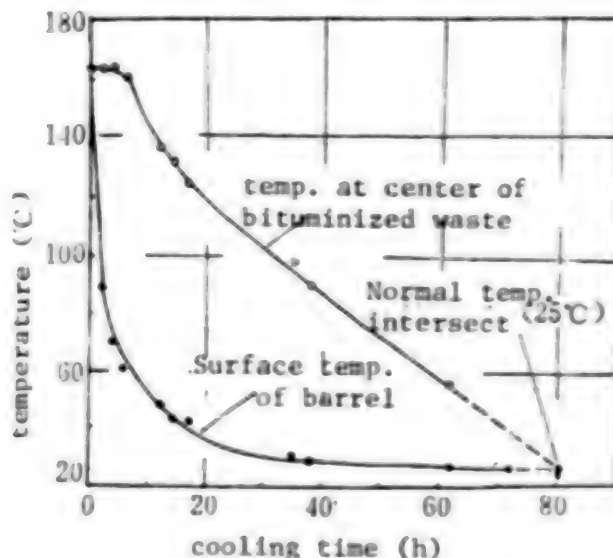
6. Thermal stability of bituminized waste (when pH 13):

- (1) initial weight loss temperature 200°C (measured on TG curves);
- (2) initial exothermic temperature 230°C (measured on DTA curves in constant temperature large specimen tests);
- (3) spontaneous combustion temperature 300°C (measured by TG, DTA, and other methods).

Bituminized waste is loaded in 200 l barrels at 160-170°C. The precipitation of salt is not apparent. It requires approximately 80 hours for the center to naturally cool down to the normal temperature (25°C), as shown in Figure 3.

Figure 3.

Natural Cooling Temperature Curve of a 200 l Package of Bituminized Product from 45 Percent Sodium Nitrate



5.2 Characteristic Indicators of Secondary Steam Condensate

1. average salt content: approximately 30 mg/l;
2. average oil content: approximately 40 mg/l;
3. pH = 7.5-9;
4. purification coefficient of turbulent evaporator with respect to  $\text{Na}^+$ : approximately  $10^4$ .

5.3 Operating Parameters of Turbulent Film Evaporators

1. The optimum linear velocity of the scraper is 9 m/s, the lower limit is 7 m/s;
2. vacuum: 50-150 Torr;
3. heating medium: the heat transfer effect was poor when over heated No 38 engine oil was used. The productivity of the turbulent evaporator only reached 40 l/m<sup>2</sup>.h. It is recommended to use steam.
4. The maximum volumetric liquid to asphalt ratio is 4.5:1; the gravimetric ratio is 5:1.
5. The scraper was operating normally, stably and reliably for 600 hours. Moreover, it was adaptable to the bituminization of all 13 model waste liquids.

It is feasible to adopt the process and equipment in the direct bituminization of low and medium level concentrated waste liquids by using a turbulent film evaporator. It is appropriate for continuous production. It is also economical and effective to use industrially pure trichlorochloride as a decontaminant to remove bituminized salt scale. The same process can be used for its recovery. The residue can be loaded in a barrel as a bituminized product without further processing. The heating temperature of the bituminization equipment should be several degrees lower than the initial reaction temperature of the bituminized product (should not be less than 20°C) to ensure the safety of production.

12553

CSO: 4008/36

# A $10^{11}$ W HIGH CURRENT PULSE ELECTRON BEAM ACCELERATOR DESCRIBED

Chongqing HEJUBIAN YU DENGGLIZITI WULI [NUCLEAR FUSION AND PLASMA PHYSICS]  
in Chinese Vol 3, No 4, 15 Dec 83 pp 235-240

[Article by Lu Chuanxin [0712 0278 3932], Song Baozeng [1345 1405 1073],  
Wu Guannu [0702 7070 1166], Zhou Pizhang [0719 0013 3864], Zhang Chunsheng  
[1728 1108 3932], Zhang Judi [1728 5468 1229], Zhao Changhe [6392 7022 0735],  
Guo Zhongsan [6753 1813 2773], Man Yongzai [3341 3057 0961], Lu Jingping  
[7627 2417 1627] and Dai Dazhi [2071 6671 2535]: "A  $10^{11}$  W High Current  
Pulse Electron Beam Accelerator"]

## [Text] Abstract

A  $10^{11}$  W water medium high current pulse electron beam  
accelerator has been developed. The machine configuration,  
principal parameters and operating conditions are  
described in this paper. The experiments of the diode  
focus are presented in detail and the comparison of  
experimental results for different cathode geometrics is  
given. The pinched electron beam behavior is diagnosed  
by means of an X-ray pinhole camera, a graphite calorimeter  
and a scintillator-optical fiber-photomultiplier system.  
The experimental results are also given.

In order to study the particle beam and target interaction experimentally,  
we developed a  $10^{11}$  W water medium high current pulsed electron beam  
accelerator.<sup>1</sup> The parameters are: output voltage 500 kV, beam current 120 kA,  
peak power approximately  $10^{11}$  W, pulse width (full width at half maximum  
70 ns and total beam energy 3 kJ.

The overall structure of the accelerator is shown in Figure 1. The twenty  
0.166  $\mu$ F parallel capacitors in the LC generator are first charged to  $\pm 80$  kV,  
a command trigger then connects five reversing switches simultaneously.  
After 1.9 ns, the output high voltage of the LC generator reaches its peak  
value, and a second command trigger pulse connects the transmission switch  
and the LC generator undergoes linear harmonic charging of the pulse.  
After 320 ns, the voltage of the pulse formation line reaches its peak  
and a third command trigger pulse connects the multichannel output switch  
and the output transmission line then receives a nanosecond pulse with an

amplitude equal to half the pulse formation line voltage and a width equal to twice the transient time. Under the action of this high voltage pulse, the diode emits a high current electron beam due to the field effect.

Figure 2 shows the voltage waveforms measured on the main components of the accelerator.

#### I. LC Pulse High Voltage Generator

As compared to the usual Marx generator, the LC generator does not have a spark switch in the main loop and the advantages are a more compact construction and a lower voltage. Therefore, the LC generator may achieve direct and rapid charging of the pulse formation line without an extra "intermediate storage capacitor."

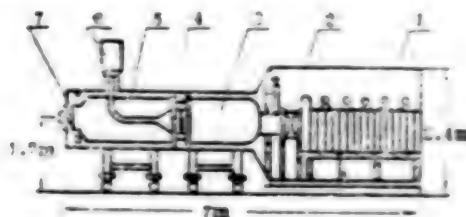


Figure 1. Schematic diagram of the  $10^{11}$  W water medium high current pulsed electron beam accelerator

Key:

1. LC generator
2. Transmission switch
3. Pulse formation line
4. Multichannel switch
5. Output line
6. Trigger
7. Diode



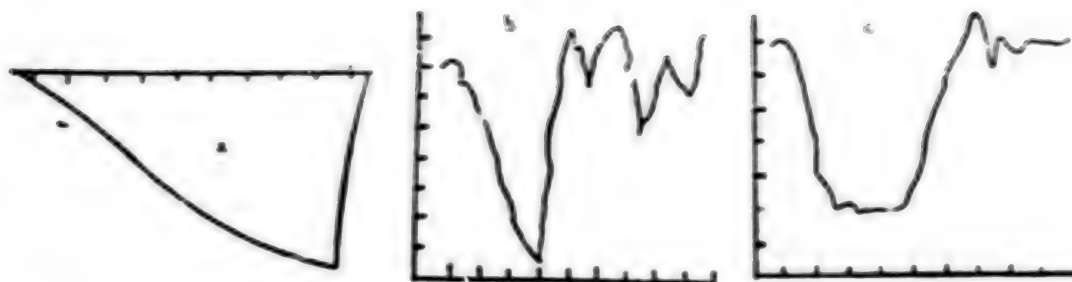


Figure 2. Voltage waveforms of main components

Key:

- (a) LC voltage waveform, time scale is 200 ns/division and peak voltage is 1.26 MV.
- (b) Voltage waveform of the pulse formation line, 100 ns/division, 176 kV/division.
- (c) Voltage waveform of the output line, 20 ns/division, 88 kV/division.

For a given charging voltage, the five reversing loops may be rigorously synchronous in order to obtain the maximum voltage output from the LC generator. The five reversing switches must therefore have a stable self breakdown voltage at a given pressure and good synchronization performance.

We used gas-filled reversing switches with ring-shaped trigger electrodes and contained a gas mixture (10 percent of  $\text{SF}_6$  and 90 percent of  $\text{N}_2$ ) at a pressure of 5 atmospheres. Experiments showed that these switches had a wide operating range for synchronization. The synchronization remained satisfactory even when the operating voltage was lowered to 40 percent of the self-breakdown voltage. This has effectively improved the stability of the generator. Figure 3 shows the open circuit output voltage waveform of the LC generator for synchronized and unsynchronized switches.



Figure 3. Open circuit output voltage waveform of the LC generator

Key:

- (a) Five reversing switches synchronized
- (b) Five reversing switches not synchronized

Table 1. lists the main parameters of the LC generator. Operating results show that this type of generator is suitable for being a high voltage source for 1-2 MV low induction microsecond pulses.

Table 1. LC generator parameters

Maximum charging voltage (kV)	$\pm 80$
Output voltage (MV)	1.6
Output capacitance (nF)	8.67
Series induction ( $\mu\text{H}$ )	3
Maximum energy storage (kJ)	11.0
Series resistance ( $\Omega$ )	1.7
Voltage efficiency to pulse formation line (%)	79
Charging time (ns)	320

## II. Water Medium Pulse Formation Line

Both the pulse formation line and the output line are coaxial lines with water as the dielectric and have an outer diameter of 1m and an inner diameter of 0.57m. The impedance is 3.75 Ohms. Deionized water has good insulation properties for short pulses (less than or equal to 1  $\mu\text{s}$ ) and the breakdown intensity and polarization effects are given by the formulas of J.C. Martin.<sup>2</sup> Since the deionized water has a high dielectric constant ( $\epsilon_r \approx 80$ ), it increases the energy storage density and the geometric dimension of the transmission line. The pulse formation line was operated for an extended period of time under 1.3 MV high voltage pulses and no breakdown was encountered.

## III. Multichannel Gas Trigger Output Switch

Figure 4 shows schematically the structure of the switch. The switch is filled with 10 percent  $\text{SF}_6$  and 90 percent nitrogen gas at 8 atmosphere of pressure. This type of switch is chosen in order to lower the induction and to suppress prepulses so that a fast risetime output pulse may be obtained and to improve the homogeneity and repeatability of the diode current.

[Figure 4., next page]

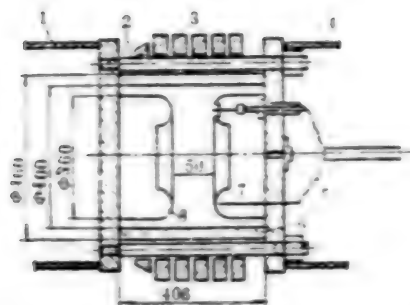


Figure 4. Schematic diagram of the multichannel switch

Key:

1. Formation line
2. Nylon rod
3. Glass ring
4. Output line
5. Trigger cable
6. Nylon tube
7. Trigger electrode
8. Electrode

The anode of the switch has 8 trigger electrodes. Eight SYV-75-9 cables deliver positive pulses (60 kV amplitude and 20 ns risetime) to the trigger electrodes so that the switch may conduct when the voltage of the pulse formation line reaches its peak. Even though the shieldings of the eight cables connect the inner conductor of the output line to ground, the effect on the main pulse transmission can still be neglected because the electromagnetic wave has a long transit time on the cable and the cable has a large inductance.

The technical difficulty of this type of switch is the effective formation of multichannels when the switch is fired. At the present time we have not found a method to measure the number of channels precisely. We roughly estimated the conduction status of the switch by analyzing the risetime of the output voltage. When the switch undergoes self-breakdown, the risetime of the output line voltage is 40 ns, similar to that of a single channel switch. When the switch undergoes trigger breakdown, the risetime is about 20 ns, equivalent to a switch inductance of 60 nH and indicating the formation of multichannels.

In order to avoid internal circuitry [?] on the inner wall of the nylon tube, an organic glass ring is added outside the tube and  $\text{SF}_6$  gas is added to reduce the distance between the electrodes. The switch has endured 1.2MV. Aside from periodic replacement of the trigger cable (every 500 fires or so) and cleaning of the switch (every 1,000 fires or so), no other maintenance is required.

#### IV. Radial Insulating Vacuum Diode

The function of the diode is to convert the electromagnetic energy to the electron beam energy and to focus the high current electron beam to the center of the anode in order to compress the energy spatially.

Figure 5 shows the construction of the diode. Also shown are the locations for electric parameter devices. The capacitive voltage divider, resistive current divider, and the Lukevich [?] coil respectively measure the voltage, diode current and the anode current of the diode. The differential ring is used for voltage correction.

We concentrated on the self-pinching characteristics of the electron beam, that is, focusing the electron beam with the magnetic field of the beam itself. We developed three diodes with different cathode geometry, and the experimental results are as follows:

1. Stainless steel needle cathode:<sup>3</sup> The cathode is a stainless steel needle 7 mm long and 1.5 mm in diameter. The anode is a flat piece of brass, separated from the cathode by 3.5 mm. The 1 mm thick brass anode target plate was punched through in one shot at 300 kV. At 450 kV, a 2 mm thick brass target can be punched through in one shot.

Experimental results show that the diode tube with a needle cathode has a small focal spot. The spatial repeatability of the focal spot is good but the total beam energy is small.

2. Hollow graphite cone cathode:<sup>4</sup> This type of cathode is shown in Figure 6. Since the aspect ratio ( $R/d$ ) is large, the critical current ( $I_{CF} = 8500 \sqrt{R/d}$ ) is also large. Tight pinching is obtained at voltages greater than 450 kV. Figure 7 shows the voltage, current, impedance and power variations of this cathode. The total energy of the electron beam is found to be 2.2 kJ by integrating the power curve.

Experimental results show that the hollow cathode diode has a long service life and a large beam energy, but the focus spot size is also large. Under identical experimental conditions, the graphite cathode has a better focusing performance than brass and stainless steel cathodes of the same shape. The larger the inner diameter of the hollow cathode, the longer it lasts before the impedance collapse, but the pinching is poorer (see Figure 8).

3. Stainless steel conical cathode: The structure of this type of cathode is shown in Figure 6(a). Experiment shows that the total beam energy and the focusing spot size is intermediate between the stainless steel needle and the hollow graphite cone cathode (see Table 2). The spatial reproducibility of the focal spot is good. Preliminary tests show a higher power density using this type of cathode.

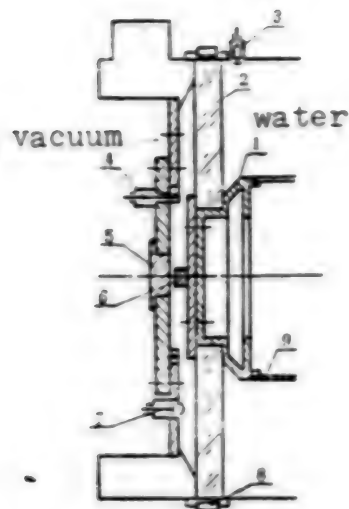


Figure 5. Construction of the diode tube

Key:

1. Transition body
2. Organic glass separator plate
3. Capacitive voltage divider
4. coil
5. Replaceable anode
6. Replaceable cathode
7. Differential ring
8. Resistive current divider
9. Inner tube of the output line

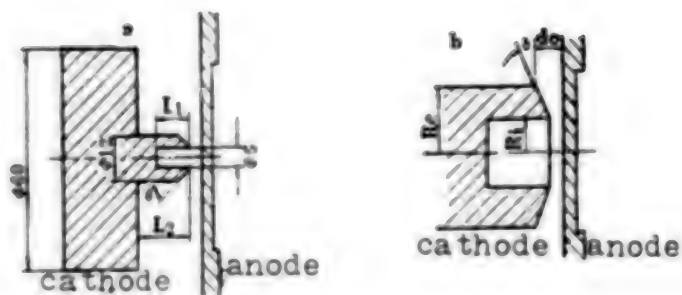


Figure 6. Structure of the diode cathode

Key:

- (a) Conical cathode,  $L_1 = 10\text{mm}$ ,  $L_2 = 15\text{mm}$ ,  $\theta = 45^\circ$
- (b) Hollow cathode,  $R_c = 25\text{mm}$ ,  $R_i = 15\text{mm}$ ,  $\delta = 5.7^\circ$ ,  $d_o = 3.5 \sim 4.0\text{mm}$

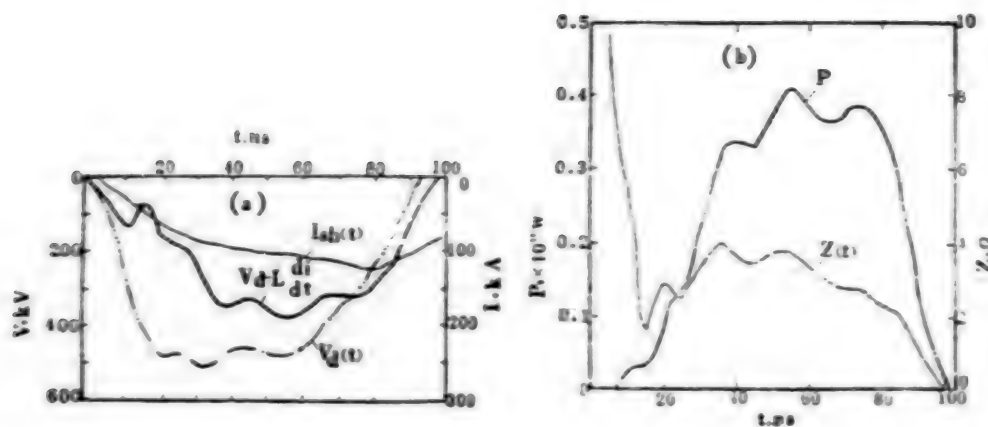


Figure 7. Experimental waveforms of the hollow graphite cathode

Key:

- (a) Voltage and current waveform of the diode
- (b) Impedance and electron beam power of the diode

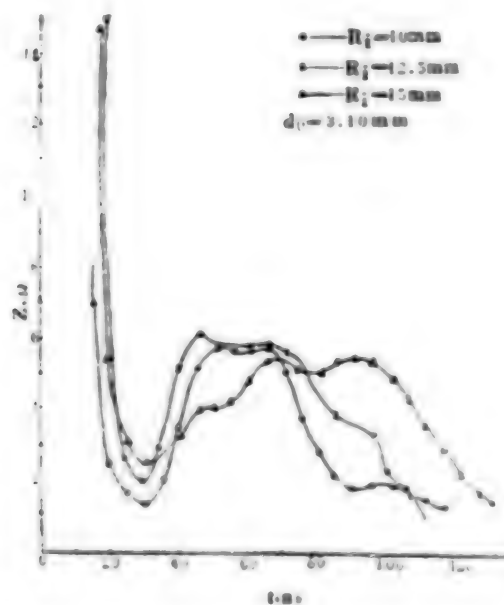


Figure 8. Impedance curve of three hollow cathodes with different inner diameters



Table 2. Diode parameters

Item	Voltage kV	Current kA	$M \frac{di}{dt}$ kV	Anode focal spot mm	Beam energy kJ	Pinch velocity mm/ns
Measuring device	Capacitive voltage divider	coil (current divider)	Differential ring	X-ray pinhole camera	Graphite calorimeter	Optical fiber- photo- multiplier
Cathode shape	planar	260	75	60	--	--
	needle	~630	~120	300	φ 1.2	0.58
	hollow cone	~450	~120	120	φ 3.8	2.10
	conic	~480	~120	190	φ 3.0	0.72

Ye Jinxiang [0673 6855 4382] has diagnosed the electron beam characteristics. Using a graphite differential calorimeter,<sup>5</sup> he measured a total beam energy of 0.58 kJ for the stainless steel cathode diode, 2.1 kJ for the hollow graphite conical cathode and 0.72 kJ for the stainless steel cone cathode. Using an X-ray pinhole camera,<sup>6</sup> he measured a focal spot size of 1.2 mm diameter for the stainless steel needle cathode, 3.8 mm diameter for the hollow graphite conical cathode and 3 mm diameter for the stainless steel conical cathode. Using a scintillator-optical fiber-photomultiplier system,<sup>7</sup> he measured an average pinching velocity of 1.3 mm/ns for the hollow graphite cone cathode. Using the calorimeter-pinhole camera-scintillator-optical fiber system,<sup>8</sup> he measured an average power density of  $1-2 \times 10^{11}$  W/cm<sup>2</sup> for the stainless steel cone cathode.

After operating the accelerator for two years, we found the accelerator to be a convenient high current pulsed electron beam source. By adjusting the charging voltage of the LC generator and the gas pressure in the switches, the diode voltage is continuously tunable in the 200-500 kV range and provides different electron beam parameters.

The authors thank Wang Shiji [3769 0013 4921] for advice and Peng Hansheng [1756 5060 3932], Liu Guoliang [0491 0948 5328], Xiong Riheng [3574 2480 1854], Hua Degen [5478 1795 2704] and He Yongwe [0149 3057 2976] for participating in this research.

#### FOOTNOTES

1. Peng Hangsheng, Design Plan for a Water Dielectric Pulsed Electron Beam Accelerator, 1978. Unpublished.
2. J.C. Martin, SSWA/JCM/704/49, AWRE, 4, 1970.

3. E.I. Baranchikov, et al., International Conference on Plasma Physics and Controlled Nuclear Fusion Research, 1, 185 (1976).
4. P. Spence, et al., Proceedings of the International Topical Conference on Electron Beam Research and Technology, 1, 346 (1976).
5. Ling Qiu [0407 3808], et al., Graphite Calorimeter for Measuring the Total Energy of a High Current Pulsed Electron Beam, 1980, unpublished.
6. He Shaotang [0149 4801 1016], Zhao Fengsheng [6392 7685 0581], et al., Focusing of a High Current Pulsed Electron Beam as Measured by Pinhole Photography, 1980, unpublished.
7. Ye Jingxiang, Measuring the Pinch Velocity of a High Current Electron Beam with a Scintillator-Optical Fiber-Photomultiplier System, 1980, unpublished.
8. Ling Qiu, et al., Measuring the Average Power Density of a High Current Pulsed Electron Beam Using a Calorimeter-Pinhole Camera-Scintillator-Optical Fiber System, 1980, unpublished.

9698

CSO: 4008/286

MICRO-DEFORMATION OF QUARTZ UNDER DYNAMIC ACTION AND ITS APPLICATIONS

Beijing DIQIUHUAXUE [GEOCHEMISTRY] in Chinese No 4, 1982 pp 403-411

[Article by Zhu Lin [2612 2651] and Meng Guangkui [1322 1639 7608] of the Twenty-First Institute]

[Text] Under the action of large stress, rocks and minerals undergo a series of deformation. By studying the micro-deformation of specimens in controlled impact experiments, one can determine the relationship between micro-deformation and pressure and thereby estimate the shock wave pressure endured by rocks in a underground nuclear explosion and use the data as a basis for classifying the damage zones in a free-field explosion medium.

There are two experimental methods of inducing micro-deformation in rocks: static pressurization and dynamic shock. A number of techniques exist in the dynamic shock method. The plane wave shock method<sup>1</sup> is a good technique for simulating underground nuclear explosion. In this paper we discuss the plane shock wave experiment in granite medium at China's underground nuclear test site. We also describe the observation results of micro-deformation of quartz under petrographic microscopes and preliminary applications of distinguishing the rock damage zones in the free field after a underground nuclear explosion.

### 1. Shock Experiment

The pressure source used in the experiment was a plane wave generator consisting of high-explosive lenses, charge column and detonator. The plane shock wave produced by the high explosive lenses pushed an impactor to hit the specimens in an impact container. The pressure provided by this set-up was experimentally calibrated. By varying the material, thickness and other properties of the impactor, we obtained 15 data points in the pressure range of 30 kbar to 380 kbar. The errors are respectively within 8 percent and 18 percent for the low end and the high end of the pressure range.

The specimens were test ground media. One type of sample is a black mica granite (henceforth referred to as medium 1) and the other type of sample is a black mica plagioclastic granite (henceforth referred to as medium 2). The rock samples were polished to form circular disks with plane and parallel faces 35mm in diameter and 4mm thick. Samples were loaded into the container and shock loaded with the calibrated pressure source. Specimens were then taken out of the container on a lathe.

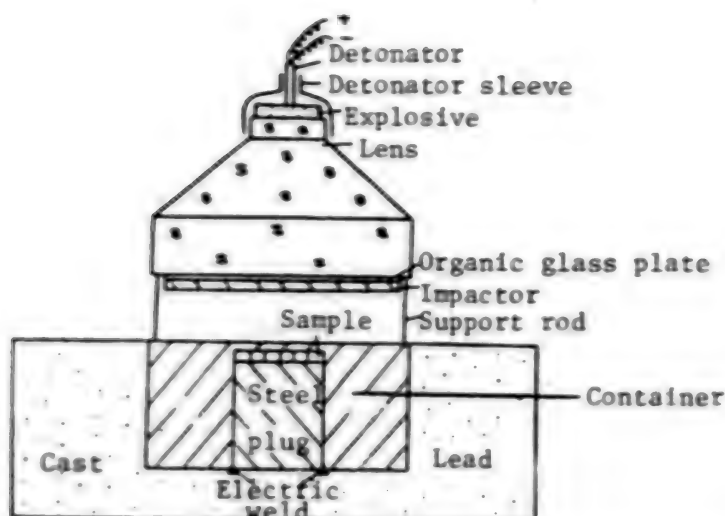


Figure 1. Cross-section of the  $139.4 \pm 2.9$  kbar device

## II. Petrographic Microscopic Observation of the Shock Samples

### 1. Microcrack statistics

Microcracks are the main characteristic deformation of quartz under a low pressure shock. As the pressure increases the number of microcracks also goes up. Microcrack statistics were obtained using a polarized light microscope fitted with a 6-axis planimeter. The number of microcracks in the quartz grains extending vertically over one half the field of view were counted in each measuring line. The same crack in two adjacent halves of field of view was counted as one crack. The length of the measuring line in each sample was generally a few hundred millimeters. By dividing the total number of cracks by the number of measuring lines, we have a value called the "crack index," i.e., the average number of microcracks in one millimeter. The crack index is an indication of the density of microcrack growth for a given pressure<sup>2</sup>. Statistics were collected for the two groups of samples at 7 low pressure points (including zero pressure). Table 1 shows the statistical results and Figure 2 shows the relationship between the crack index and pressure based on the data in Table 1.

Table 1. Crack index in medium 1 and medium 2 at different pressure

Medium	1							2						
Pressure (10 <sup>4</sup> bar)	0	3*	5*	7*	7.4	8.7	10.8	0	2.82 $\pm 0.49$	5.57 $\pm 0.44$	6.93 $\pm 1.23$	8.55*	9.97 $\pm 1.38$	11.63*
Crack index	2.2	4.4	8.2	11.2	11.8	14.9	19.3	9.1	10.8	13.5	20.9	28.3	35.8	44.8

\*uncalibrated pressure

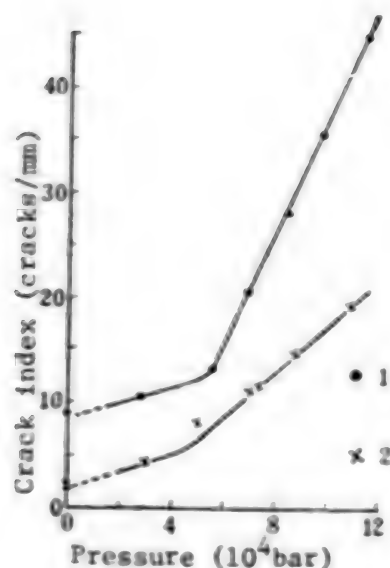


Figure 2. Crack index of quartz as a function of pressure

Key:

1. Medium 1 data
2. Medium 2 data

## 2. Micro-lamellae statistics

When the peak pressure of the shock wave reaches a certain value, a set of parallel and closely spaced ( $2-5 \mu\text{m}$ ) deformation lines with a thickness of  $1-2 \mu\text{m}$  or less begin to appear in the quartz crystal along certain crystalline planes. We shall call one set of parallel lines with one orientation as a group. At low pressure a crystalline grain often grows one group of lamellae consisting of 5 sets or more. At high pressure there may be several groups and the number of sets in each group also increases<sup>3</sup>. These deformation lines are given different names in the literatures. We prefer the term "shock-induced micro-lamellae." The method of collecting statistical data of the micro-lamellae<sup>4</sup> is to place a wafer of standard rock on a (Feishi) rotation stage installed on a polarized light microscope and use a Wolff net plate for the analysis. The angles between the poles of the shock lamellae and the c-axis of quartz are obtained graphically. From the values of these angles, one can determine (by looking up a table) the crystalline plane parallel to the lamellae growth. Generally 100-200 sets of statistical data were collected for each sample. The results are listed in Table 2 and Table 3 and plotted as histograms in Figure 3. In Figure 3 the abscissa is the angle between the micro-lamellae pole and the c-axis of quartz and the ordinate is the growth frequency of the micro-lamellae expressed in percentage. Figure 4 shows the micro-lamellae ratio in quartz as a function of pressure for different orientations in medium 2.

Our observations showed that micro-lamellae in quartz began to grow at a pressure of 87 kbar for medium 1 specimens. For medium 2, the pressure was

69.3  $\pm$  12.3 kbar. We therefore believe that micro-lamellae in quartz in granite samples subjected to a plane shock wave began to grow at a pressure between 70 and 90 kbar.

Table 2. Micro-lamellae of quartz in medium 1 after shock

Freq Crystal plane	P(10 <sup>4</sup> bar)								
	8.7	10.8	11*	14*	17*	18	20*	25.7	CA $\perp$
$\omega\{10\bar{1}3\}$	48.3	21.2	27.3	16.7	17.8	13.5	24.6	23.5	22°
$\pi\{10\bar{1}2\}$	14.6	13.4	17.1	15.2	13.9	18.1	26.3	24.7	32°
$\xi\{11\bar{2}2\}$	12.5	17.3	15.9	15.9	18.8	14.8	14.3	17.1	47°
$\tau\{10\bar{1}1\}$	8.3	25.0	13.0	21.7	18.8	16.7	11.4	11.8	52°
$i\{11\bar{2}1\}$	4.2	2.0	8.0	10.1	15.0	19.4	6.3	10.6	64°
$\pi\{51\bar{6}1\}$	2.0	2.0	0	2.9	3.0	0	0.6	1.2	82°
$\{22\bar{4}1\}$	0	4.0	1.1	2.1	2.0	1.3	3.4	1.8	77°
$\{21\bar{3}1\}$	0	0	1.1	1.5	3.0	5.2	2.3	1.2	71°
$c\{0001\}$	0	0	2.3	1.5	1.0	0	1.7	0	0°
$m\{10\bar{1}0\}$	2.5	0	1.1	0.7	0	2.6	0.6	0	90°
Misc	12.5	15.4	13.6	11.6	6.9	7.7	8.6	8.8	
$\omega/\pi$	3.00	1.58	1.60	1.10	1.28	0.75	0.94	0.95	
$\frac{\xi + \tau + i + \dots}{\omega + \pi}$	0.05	1.45	0.95	1.77	1.94	1.92	0.80	0.89	

### 3. Ordinary light refractive index changes in quartz

When quartz is subjected to high pressure shock, both its principal refractive indices will change. In our observations, we only made statistical study of the changes in the ordinary light refractive index  $N_o$  of quartz. Because the forces experienced by the shock specimens is nonuniform, the changes of the principal refractive index  $N_o$  in different crystalline grains of the same specimen are not all the same. Even in the same crystal grain the changes in  $N_o$  may still vary with location. Therefore, the pressure dependence can be obtained only after the maximum change in  $N_o$  is found for a specific pressure. The method we used was to select single-crystal grains 100  $\mu$ m (0.1mm) in size or smaller and compare their refractive indices with oils of known index until the maximum  $N_o$  was found. This is the immersion comparison method.



Table 3. Micro-lamellae of quartz in medium 2 after shock

Freq P(10 <sup>4</sup> bar)	9.97±1.36	11.6*	13.94 ±0.29	16.12*	17.30 ±0.41	20.70*	23.74 ±1.71	C/A ⊥
Crystal plane								
$\omega\{10\bar{1}3\}$	59.2	53.0	58.0	37.3	31.1	31.1	29.4	22°
$\pi\{10\bar{1}2\}$	9.6	12.1	21.0	21.2	24.8	31.1	29.4	32°
$\xi\{11\bar{2}2\}$	15.2	13.6	16.4	16.9	15.0	9.9	11.2	47°
$r\{10\bar{1}1\}$	5.6	9.1	9.9	11.0	9.7	8.0	5.9	52°
$r\{1\bar{1}21\}$	3.2	3.0	1.2	3.4	2.9	2.8	2.7	64°
$r\{51\bar{8}1\}$	1.6	0	1.8	1.7	1.5	2.4	3.2	82°
$\{22\bar{4}1\}$	0.6	0	0.6	0	4.4	1.4	2.7	77°
$\{21\bar{3}1\}$	0	1.5	0.6	1.7	1.5	1.9	0	71°
$c\{0001\}$	2.4	4.5	0.6	0	0	0.5	0	0°
$m\{10\bar{1}0\}$	0.8	0	0	0	0	1.4	2.1	90°
Misc	1.6	3.2	9.8	6.8	9.2	9.4	13.4	
$\omega/\pi$	6.17	4.38	1.81	1.76	1.25	1.00	1.00	
$\frac{\omega + r + \xi + \dots}{\omega + \pi}$	0.42	0.40	0.55	0.61	0.63	0.45	0.45	

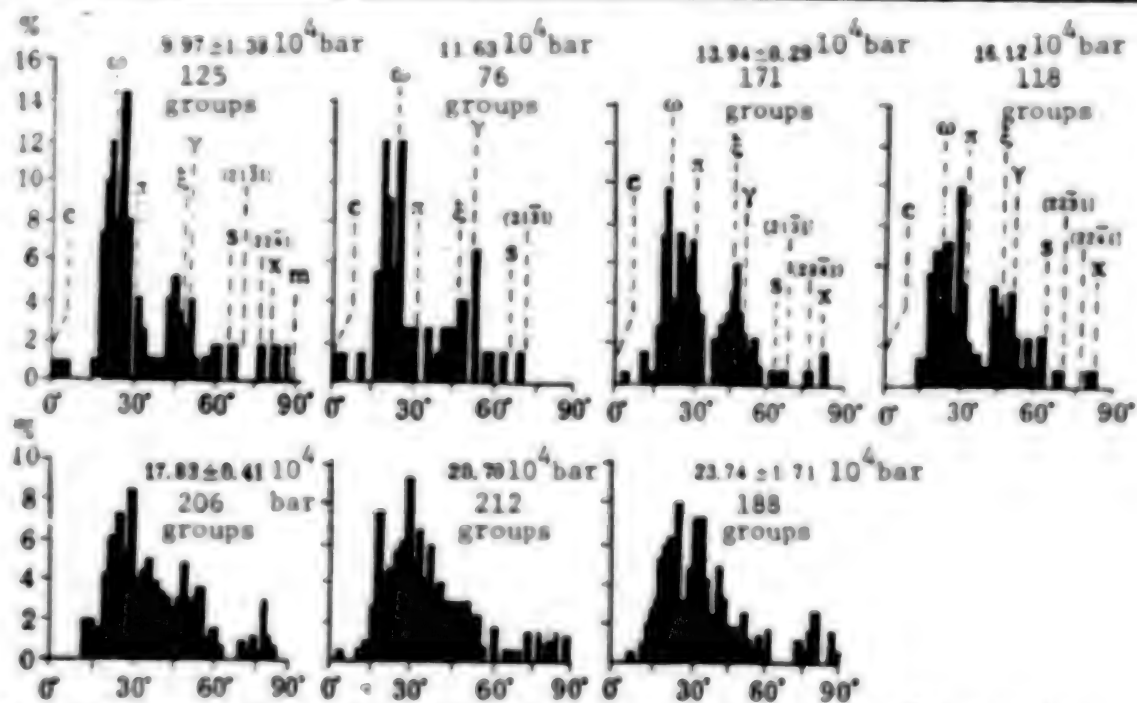


Figure 3. Histogram for medium 2 specimens as a function of the angle between the micro-lamellae pole and the c-axis of quartz



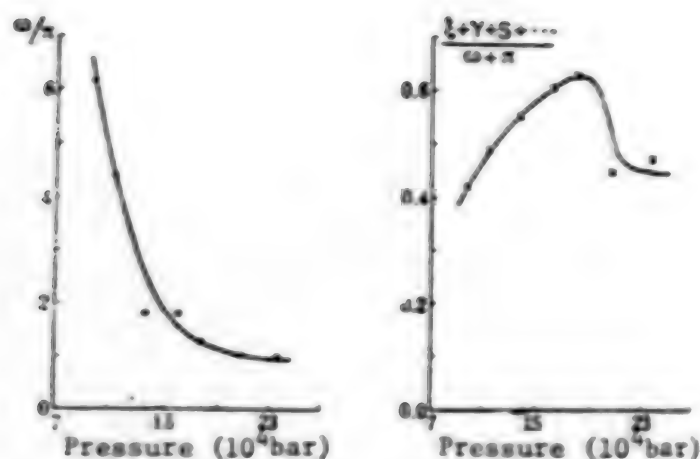


Figure 4. Micro-lamellae ratio of quartz as a function of pressure for medium 2

For each sample we used at least 50 grains in the comparison. The measurement results showed that  $N_0$  of quartz for the two media showed no change for pressures up to 140 kbar. After 140 kbar the refractive index  $N_0$  showed systematic change. The higher the pressure, the lower the  $N_0$ . In a 273.2 kbar medium 2 specimen some of the crystal grains began to homogenize. Its refractive index was about 1.460 and the pressure for total homogenization was about 300 kbar. Table 4 shows the observation results for the two media and Figure 5 shows the decreasing refractive index as a function of pressure.

Table 4. Changes in refractive index  $N_0$  of quartz after shock

Sample P(10 <sup>4</sup> bar)	Medium 1					Medium 2					
	14*	17*	18	20*	25.7	13.94 ±0.29	16.13*	17.83 ±0.41	20.7*	23.74 ±1.71	27.32*
Minimum $N_0$	1.544	1.540	1.539	1.537	1.512	1.544	1.541	1.539	1.535	1.521	1.460
Decrease in $N_0$	0	0.004	0.005	0.007	0.032	0	0.003	0.005	0.009	0.023	0.084

Based on the discussion above, we may draw the following conclusions:

(1) For quartz in granite specimens under controlled shock loading, the principal deformation characteristics at lower pressure is microcracking. 50 kbar is the critical point for the crack index, from a few thousand bar to 50 kbar, the crack index increases slowly, beyond 50 kbar, it increases rapidly.

(2) The shock lamellae begin to develop at a pressure less than 70-90 kbar. In the pressure range from 7 kbar to 12 kbar, the shock lamellae are parallel to the  $\{10\bar{1}3\}$  planes, for pressures greater than 200 kbar [sic],

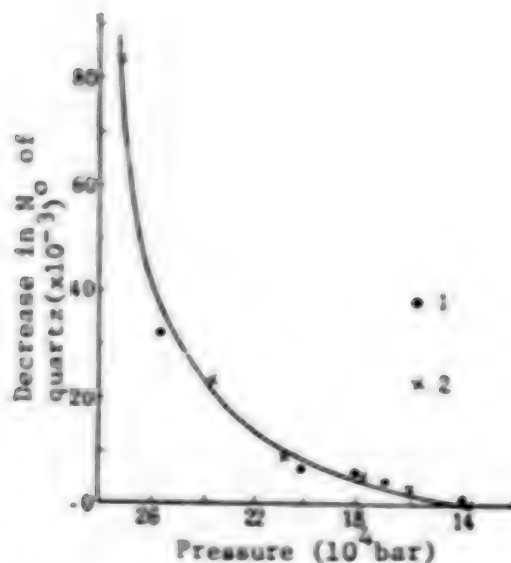


Figure 5. Refractive index of shocked quartz as a function of pressure

Key:

1. Medium 1 results
2. Medium 2 results

the lamellae growth is parallel to the  $\pi \{10\bar{1}2\}$  planes, between 140 and 180 kbar the growth parallel to  $\xi \{11\bar{2}2\}$  and  $\zeta \{1121\}$  dominates. As pressure increases,  $\omega/\pi$  gradually decreases, at medium pressure,  $(\xi + \zeta + \dots)/(\omega + \pi)$  is relatively large and greater than 200 kbar, the two ratios above are independent of pressure, see Figure 4.

(3) At a pressure 150 kbar or so, the ordinary light refractive index  $N_o$  of quartz begins to decrease and the amount of decrease becomes greater as the pressure increases. At the vicinity of 270 kbar, some of the quartz grains begin to homogenize and at 300 kbar all the quartz grains become homogenized.

(4) The petrological properties of the two types of granites are somewhat different, but the shock-induced changes of the quartz in the granite are quite similar and their pressure dependence are also basically the same.

Based on the results just described, we may use the microscopic deformation of quartz in the granite to obtain the peak shock wave pressure experienced by the granite medium in a nuclear explosion. Microcracks may be used in the evaluation of pressures below 100 kbar. Shock lamellae may be used to determine the pressure in the 70 kbar to 200 kbar range. The change in the refractive index  $N_o$  may be used for estimating the pressure from 150 kbar to the pressure that produces homogeneous glass states.

### III. Preliminary Observation of Micro-deformation in Quartz Caused by Nuclear Explosion Shock Wave

An underground nuclear explosion causes damages to the rocks in the peripheral of the cavity. Rock damage is usually divided into the ruptured compact

zone, the cracked loose zone, and the residual stress zone<sup>5</sup>. After one underground nuclear explosion, a probe hole was drilled through the cavity and research specimens were taken from the rock core of the hole. Studies were made using the methods described above. A lamprophyric rock core with a quartz content of only 5 percent was obtained from the section immediately adjacent to the bottom of the cavity. The micro-deformation of quartz should be greatest in the section adjacent to the cavity wall, but difficulties were encountered in the microscopic statistical measurement because of differences in the rock properties and insufficient sample.

In the space below we shall describe the observation results of various deformations and the application to the classification of rock damages in the free field of the explosion.

### 1. Preliminary observation of microcracks

Since the quartz content in the lamprophyre was too low to satisfy the statistical requirements, we only made statistical measurements of quartz microcracks in granites located slightly farther away from the explosion center and experienced weaker shock waves. Table 5 shows the measurement results and Figure 6 shows the quartz crack index as a function of the radial distance from the cavity wall with the origin taken at the cavity wall.

Table 5. Statistical results of quartz crack index obtained after a underground nuclear explosion

Sample No	Radial distance from cavity wall (m)	Forecast pressure ( $10^4$ bar)	Crack index
19	9.94—10.15	1.70—1.58	3.4
21	11.15—11.75	1.45—1.38	3.6
23	12.00—13.65	1.30—1.18	3.3
25	16.40—17.55	0.96—0.90	2.8
28	22.40	0.68	2.4
29	25.15	0.60	2.4
30	28.15	0.52	2.2
32	33.65	0.40	2.3
35	40.15	0.33	2.4
37	47.28	0.25	2.0

As can be seen in Figure 6, the quartz crack index monotonically decreases as the radial distance from the cavity wall increases. The background value 2.2 is reached at a distance of 33.65m from the cavity wall. Because specimens of 30 kbar or less were unavailable in the experiment, we did not obtain the pressure at which the quartz crack index exceeded the background. Based on quartz microcrack statistics in the American "Hardhat" explosion medium granodiorite obtained by N. M. Short<sup>6</sup>, the quartz crack index began to exceed the preexplosion background at 3 kbar. Because both black mica granite and granodiorite are granites, we used the results of Short and assumed the peak pressure of the shock wave at 33.65m from the cavity wall

to be 3 kbar. This is very close to the 4kbar pressure forecasted for that location, see Figure 7.

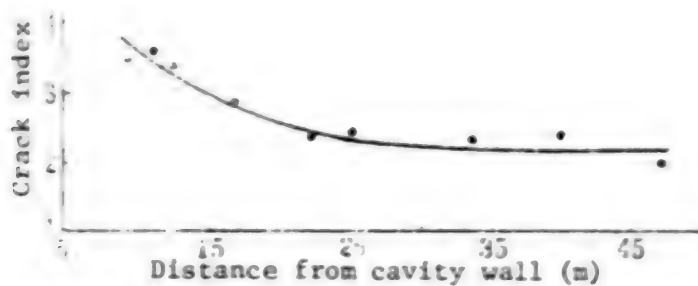


Figure 6. Quartz crack index as a function of radial distance from the cavity wall

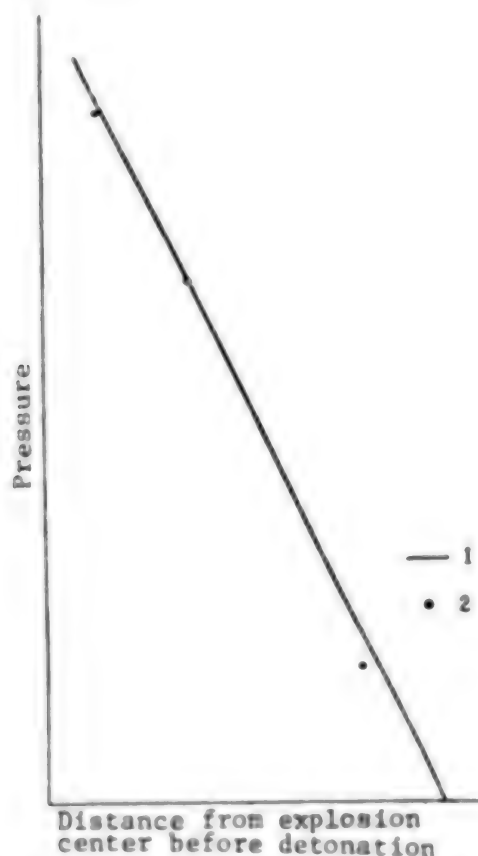


Figure 7. Comparison of calculated pressure and forecasted pressure

Key:

1. Forecasted pressure versus distance
2. Pressure deduced from quartz deformation after the explosion

## 2. Preliminary observation of the shock micro-lamellae

The growth shock micro-lamellae was observation in quartz in the lamprophyre specimens located within 1.65 m from the cavity wall but not outside this range. Since the quartz content was very low in such specimens, a statistical functional study was difficult to make. As described earlier, the pressure at which shock lamellae began to grow in our experiment was 70-90 kbar and the results of Short's study of Hardhat explosion medium<sup>6</sup> showed that shock lamellae began to grow in quartz at a pressure of 50-75 kbar. Even though the shock conditions of these hard intrusions were different and the rock properties were not exactly the same, the pressures at which shock lamellae began to grow in quartz were relatively close. We therefore accept 70 kbar as the pressure at which the growth of shock lamellae began in quartz contained in the lamprophyre. The forecasted pressure at 1.65m from the cavity wall for this particular explosion was also 70 kbar, consistent with the pressure deduced from shock micro-lamellae in quartz.

## 3. Preliminary observation of the change in ordinary light refractive index in quartz

This study was made using the lamprophyre specimens (No 1-4) taken from the vicinity of the cavity wall. The radial distances were 0-0.65m for specimens No 1 and No 2 and 1.15-1.65m for specimens No 3 and No 4. Studies of these specimens showed that only specimen No 1 had homogenized grain with a refractive index of 1.460. In a large single crystal homogenization occurred only locally and the rest of the crystal grain showed shock lamellae growth. This not only showed the inhomogeneity of pressure within a crystal grain but also gave the pressure for the onset of homogenization. As described earlier, the pressure was 273.2 kbar for partial homogenization and 300 kbar for total homogenization, we therefore conclude that the shock wave peak pressure was 270-300 kbar at the location of specimen No 1. Specimen No 1 was closer to the cavity wall than specimen No 2; in terms of color specimen No 1 has changed from the original grayish green to grayish white. The radial distance from the cavity wall to specimen No 1 was estimated to be 20 cm. Therefore, the shock wave peak pressure at 20 cm from the cavity wall in this explosion as deduced from refractive index study was 270-300 kbar, close to the theoretical forecast value of 310 kbar.

The examples given above are applications of controlled shock experiments in the deduction of shock wave peak pressure after nuclear explosions. Table 6 gives a comparison of the pressure deduced from deformation studies and the forecasted pressure. Limited by the number of available specimens, we gave the pressure at only three points. The comparison in Table 6 shows good agreement between the deduced pressure and the forecast pressure.

As already discussed, the shock wave of a underground nuclear explosion causes rock deformation and damage in the free field outside the cavity. The results of Short's study showed that at 3 kbar the microcracking in feldspar and quartz contained in granodiorite exceeded the background. The microcracking increased slowly from 3 kbar to 40 kbar. Above 40 kbar, microcracking increased noticeably. As pointed out by Short, 3 kbar is

Table 6. Comparison of the forecasted pressure and the pressure deduced from quartz deformation in a nuclear explosion medium

Quartz deformation	Radial distance from cavity wall (m)	Pressure ( $10^4$ bar)	
		Deduced	Forecast
Grain homogenization	0.20	27-30	31
Lamellae growth	1.65	$7.0 \pm$	7.0
Crack index approaching background	33.65	$0.3 \pm$	0.4

close to the limit of the dynamic tensile strength determined by R. Butkovich and 40 kbar is the dynamic elastic limit<sup>6</sup>. In fact, Short used these two values as the standard for the classification of the rock damage zones in the free field, 40 kbar is the outer boundary of the compact ruptured zone and 3 kbar is the outer boundary of the loose cracked zone. The dynamic elastic limit of the medium 1 granite is 55.4 kbar, close to the 50 kbar pressure at which the quartz crack index made a sudden jump as described earlier. We therefore take 50 kbar as the outer boundary of the compact ruptured zone and the quartz deformation indicator is the pronounced increase in microcracking. We take 3 kbar as the outer boundary of the loose cracked zone and the quartz deformation indicator is that the microcracking begins to exceed the background value. According to our study of the post-explosion specimens, the pressure at a distance of 33.65 m from the cavity wall was 3 kbar and the pressure at a distance of 2.65 m from the cavity wall was 50 kbar<sup>a)</sup>. The free field rock damage zones of the underground nuclear explosion studied can be expressed with the following empirical formulae:

$$\text{Cavity radius} \quad R_{\text{cavity}} = 11.2 W^{1/3} \quad (1)$$

$$\text{Radius of the compact fractured zone} \quad R_{\text{compact}} = 12.7 W^{1/3} \quad (2)$$

$$\text{Radius of the loose cracked zone} \quad R_{\text{loose}} = 30.3 W^{1/3} \quad (3)$$

$$\text{Radius of the residual stress zone} \quad R_{\text{residual}} = 58.2 W^{1/3} \quad (4)$$

where  $W$  is the equivalent explosive in kilotons and  $R$  is the distance measured from the explosion center. Equations (1) and (4) are determined from interrogation drilling.

#### IV. Conclusions

In this paper we described the controlled shock experiments in two types of granites using plane waves and presented analysis results of petrographic microscope studies of samples recovered immediately after the explosion. As an example of application, we have also described a study of quartz microdeformation in a underground nuclear explosion and the classification of free

a) The distances given are after the explosion.



field rock damage zones. It should be pointed out that the pressure calculations in the simulation experiments were made using the low pressure equation of state data<sup>7</sup> on the same type of granite in the United States. As discussed earlier, we only deduced the pressure at three points for the actual underground nuclear explosion because of the limited number of available specimens. Of the three points, the 3 kbar pressure at which microcracking exceeded the background was obtained on the basis of Short's conclusion. The other two pressures were deduced from the quartz deformation in the lamprophyre. Even though the quartz deformation in the several types of rocks discussed in this paper are not strong functions of pressure, the conclusions do show a certain degree of similarity. Further research are needed to improve the understanding.

The authors thank Ouyang Ziyuan [2962 7123 5261 6678], Wang Daode [3769 6670 1795] and Xie Xiande [6200 0341 1795] for valuable consultation on the experimental method and Liu Changtai [0491 7022 3141] and Li Shizhang [2621 1102 2222] of the Twenty-First Institute for their contribution to the pressure calibration experiments.

1. N. M. Short, "Experimental Microdeformation of Rock Minerals by Shock Pressures From Laboratory Scale Impacts and Explosion," in Shock Metamorphism of Natural Materials, B. M. French and N. M. Short, editors, 1968, p 219.
2. N. M. Short, *J. Geophys. Res.* 71, 1195 (1966).
3. F. Horz, "Statistical Measurements of Deformation Structures and Refractive Index in Experimentally Shock Loaded Quartz," in Shock Metamorphism of Natural Materials, B. M. French and N. M. Short, editors, 1968, p 243.
4. He Zuolin [0149 0155 7207], "Application of Stereographic Polar Projection in Geosciences," Science Press, 1965.
5. Lu Yan [7130 1484], *Hydrological Geology and Engineering Geology*, 5, 36 (1980).
6. N. M. Short, "Nuclear-explosion-induced Microdeformation of Rocks: An Aid to the Recognition of Meteorite Impact Structures," in Shock Metamorphism of Natural Materials, B. M. French and N. M. Short, editors, 1968, p 185.
7. A. J. Chabai and R. C. Bass, "Measurements on a Spherical Shock Wave in a Granite Medium," SC-4741-RR, 1963.

9698

CS0: 4008/52

## LIFE SCIENCES

### FORUM DISCUSSES BIOENGINEERING IN SICHUAN

Chengdu SICHUAN RIBAO in Chinese 7 Feb 84 p 2

[Article by Shen Longyi [3088 7893 0181]: "The Prospects for Biotechnical Research Are Bright: A Summary of a Panel Discussion among Some of Sichuan's Experts"]

[Text] On 24 January, experts from Sichuan University, the Sichuan Medical College, the Chengdu Technical University, the Chengdu Institute of Biology, the Sichuan Institute of Antibiotics, the Sichuan Foods Fermenting Institute and the Sichuan Soil and Fertilizer Institute participated, at the invitation of the Sichuan Science and Technology Commission, in a panel discussion of how to accelerate the development of biotechnology in the province. The experts surveyed the future and raised ideas.

According to these experts, biotechnical engineering includes genetic engineering, cytoengineering, fermentation engineering and enzymatic engineering and forms an important component of the new technological revolution. Bioengineering enjoys much potential for application in Sichuan's economic development, agriculture, animal husbandry, aquatic production, medicine, environmental protection and silk, leather goods, textile, brewing and chemical industries.

Wu Yanyong [0702 5888 1661], associated researcher at the Chengdu Institute of Biology, noted that Sichuan is a leading producer of famous wines, yet output thereof remains low, and the ratio of fine-wine production at Luzhou's old wine cellars is only 10 percent. Thus, if we emphasize microbial fermentation engineering, we can increase taxable profits in fine-wine production by 100 million yuan. Li Zelin [2621 3419 2651], an engineer at the Foods Fermentation Institute, and Huang Guanglin [7806 0342 3829], an associate professor at Sichuan University, stressed the importance of the development of enzyme engineering, stating that enzymatic preparations, simulation and fixation technology enjoy widespread applicability in all fields and that detergents with enzyme additives possess great developmental value. If we employ enzyme technology to effect amylofermentation, we can achieve a general renovation of traditional alcohol production technology. Liu Fangxiu [0491 2455 4423], assistant researcher at the Sichuan Soil and Fertilizer Institute, believes that bioengineering should be utilized in isolating, fermenting and domesticating prized edible fungi and in studying the biological nitrogen fixation of crops. His institute has collected,

isolated and is currently conducting simulated tests of the "gray-tree flower," the "fungus of the immortals" and the "yellow cap," rare fungus species that may prove cultivatable. His institute has also isolated effective soybean nodule bacterial strains that can increase soybean yields by 20 to 30 percent with only 15 fen worth of bacterial manure. Yue Yilun [2867 0110 0243], professor at the Chengdu Technical University, and Hu Xiaosu [5170 1321 4790], associate researcher at the Sichuan Medical College, stressed the importance of bioengineering in medicine. They emphasized the organization of key-task development of artificial heart valves, which efforts can greatly promote research on the cardiovascular system, improve medical treatment and, with some new products, directly yield substantial economic results.

These experts believe that, while Sichuan may have started later than developed countries and continues to lag behind some provinces in China in bioengineering, Sichuan nevertheless possesses many favorable conditions and much potential in this field. First, Sichuan enjoys rich material resources. Our province has more than 10,000 species of higher plants alone, ranks first nationally in terms of gymnosperms and second in angiosperms, produces one-half of China's wild edible fungi and thus is a rich, natural genetic storehouse. We can use biotechnology to develop this storehouse and promote Sichuan's economic development. Secondly, Sichuan possesses considerable technological strength, which is distributed among universities, research units and productive sectors and can be organized into a unified key-task force. Sichuan has 40 institutions of higher learning, disciplines and specialized basic support structures; several tens of central, local and departmental research institutes; and much talent and equipment. Thirdly, bioengineering has already established a foundation in some areas, achieved some progress and produced substantial results in application. If we proceed from Sichuan's actual conditions and organize for the development of bioengineering, we will certainly achieve even greater results in the next few years.

These experts believe that in the short-term Sichuan should focus on providing the things needed in the development of agriculture, light industry, foods and medicine; strengthen technological development in fermentation and enzyme engineering; closely integrate basic research, applied research, extension and application; and strive for economic results. Meanwhile, the province should also organize research and technological development in genetic and cytoengineering at qualified universities and colleges, strengthen inter-provincial and international contact and cooperation, be attentive to the import of technology and equipment and require that colleges and universities strengthen related specialties and curricula so that talent can be trained as soon as possible.

12431

CSO: 4008/205

## LIFE SCIENCES

### MODERN CONTRACEPTIVE DRUG PLANT COMPLETED IN SHANGHAI

Shanghai JIEFANG RIBAO in Chinese 6 Dec 83 p 1

[Article by Wang Yinhua [3769 6892 5478]: "The Contraceptives Plant of the Huaihai Pharmaceutical Factory Is Completed; China's First Modern Contraceptive Drug Plant"]

[Text] Assisted by the UN Fund for Population Activities, China's first modern contraceptive drug plant, the Injectable Contraceptives Plant of the Huaihai Pharmaceutical Factory in Shanghai, has been completed after 17 months of construction. Yesterday (5 December), the Shanghai Pharmaceutical Administration convened a national conference at the site to check and accept the plant and initiate trial production.

This new contraceptives plant meets international pharmaceutical production and quality-control standards and was designed by Shanghai Municipality. The entire project, which includes two large sections for producing drug materials and injection devices as well as auxiliary facilities, covers 26 mu and has a building area of over 10,000 square meters. Primary production equipment and precision instruments were imported from abroad and financed by the United Nations, but the rest of the support components were funded and supplied domestically. Since the plant will employ advanced technology and scientific management, worker safety and waste disposal problems can basically be handled internally.

The plant is designed annually to produce 9.5 tons of such drugs as delalutin and estradiol valerate and 32.5 million multiuse contraceptive injection devices, which can supply the needs of 2.5 million childbearing-aged women for 1 year. Once production formally begins, the plant will double the present supply of such devices and thus will play an important role in controlling population growth in the municipality and in supplying the drug needs of family planning programs in fraternal provinces and municipalities.

Attending yesterday's conference were representatives from the State Pharmaceutical Administration, the China Pharmaceutical Industry Co, the Shanghai Planning and Capital Construction Commissions and other related departments. After careful evaluation, the representatives determined that construction quality meets design specifications and gave approval to commence trial production.

12431

CSO: 4008/205

BRIEFS

**SHANGHAI CONTRACEPTIVES PLANT**--Dedication ceremonies were conducted yesterday (21 February) for the Injectable Contraceptives Plant of the Huaihai Pharmaceutical Factory, construction of which was assisted by the UN Fund for Population Activities. This project, which includes two large sections for producing drug materials and injection materials as well as auxiliary facilities, covers 26 mu and has a building area of 10,000 square meters. Primary production equipment and precision instruments were financed by the United Nations and imported from abroad, but the rest of the support components were funded and supplied domestically. The plant is designed annually to produce 9.5 tons of such drugs as delalutin and estradiol valerate and 32.5 million multiuse injection devices, which can supply the needs of 2.5 million child-bearing aged women for 1 year. Since commencing trial production last year, the plant has already produced 3 tons of drug materials and 3-plus million injection devices. The quality of this output meets national standards, and the project has satisfied design requirements. At yesterday's dedication ceremonies, Li Xiaodong [2621 2556 2639], deputy director of the State Pharmaceutical Administration; Sun Rentong [1327 0088 0681], director of the Shanghai Pharmaceutical Administration; (Baiweila), China-based representative of the UN Fund for Population Activities; and (Boken), administrative director of the International Contraceptive Technology Extension and Application Center, each delivered speeches congratulating the completion of the project and the plant's commencement of production. [Text] [Shanghai JIEFANG RIBAO in Chinese 22 Feb 84 p 1] 12431

**NEW ANTIVENINS**--The JIANKANG BAO [HEALTH] reports that new specific drugs have been added to the treatment of poisonous snake bites. The Shanghai Vaccine and Serum Institute under the Ministry of Public Health, the Pharmacology Teaching and Research Section of the Guangzhou Medical College and other units have cooperated to develop six new antivenins. These drugs include refined antivenins for the Pallas pit viper, the long-nosed pit viper, the many-handed krait and the cobra, which preparations have already been appraised by the state and put into production by the Shanghai Vaccine and Serum Institute; and antivenins for the banded krait and the daboia, which drugs are now undergoing trial use clinically. These drugs neutralize snake venom very effectively. Relevant medical units in Guangxi, Guangdong, Fujian, Anhui and Jiangxi have employed the antivenins to save as many as 1,000 snake-bite victims, and the drugs have shown distinct curative effect. In most minor and grave cases, blood tests are conducted to diagnose the type

of snake bite; and once the appropriate antivenin is administered, the patients' general symptoms disappear within 12 hours and local swelling is basically alleviated. The cure rate is more than 95 percent. [Text]  
[Beijing RENMIN RIBAO in Chinese 15 Mar 84 p 3] 12431

CSO: 4008/205



## SCIENTISTS AND SCIENTIFIC ORGANIZATIONS

### ELECTRONICS, COMPUTER SOCIETIES 1984 ACTIVITIES

Beijing JISUANJI YANJIU YU FAZHAN [COMPUTER RESEARCH AND DEVELOPMENT] in Chinese No 2, 1984 pp 64-65

[Table: "China Electronics Society and China Electronic Computer Society 1984 Activity Plan"]

[See table on following page]

[Text]

<u>Name of Activity</u>	<u>Time &amp; Place</u>	<u>Host Units</u>	<u>Cooperating Units</u>	<u>Scale</u>	<u>Notes</u>
1. First International Conference on Computers and Their Applications	June 1984, Beijing				Jointly sponsored by China Electronics Society, China Electronic Computer Society and the U.S. Institute of Electrical and Electronics Engineers; Note: domestic preparatory meeting to be held in April, 1984 and to be attended by domestic authors and programmers
2. Exhibit of Achievements in Micro-computer Applications	1984, Xi'an	Microcomputer Branch and Shaanxi Science Committee	Shaanxi Micro-computer Branch		
3. Exhibit of New Microcomputer Products and Technology	1984, Guangzhou	Microcomputer Branch	Guangdong Science Committee and South China Normal University, Microcomputer Institute		

<u>Name of Activity</u>	<u>Time &amp; Place</u>	<u>Host Units</u>	<u>Cooperating Units</u>	<u>Scale</u>	<u>Notes</u>
4. Microcomputer Applications and Development Training Class	1984	Computer Society and Wuhan Zhonghua Electronic Instrument Plant	Local Units concerned		
5. Third Exchange Meeting on Use and Maintenance Technology of Peripheral Equipment	March 1984, Wuxi	Peripheral Equipment Study Group	Wuxi Electronic Computer Plant	150 persons	Jointly sponsored by China Electronics Society, China Electronic Computer Society and the U.S. Institute of Electrical and Electronics Engineers.
6. Second Computer Maintenance Technology Conference	First Quarter 1984, Wuhan	Maintenance Study Group	Wuhan Institute 709	150 persons 6 days	Notice soliciting articles already issued
7. Second Microcomputer Program Design and Distributed Systems Conference	October 1984, Guilin	Microcomputer Program Design and Distributed Systems Study Group	Wang Shulin [3769 2885 2651] Chinese Academy of Sciences, Computer Institute	150 persons 7 days	"
8. Conference on Design Automation of Digital Systems [CAD]	August 1984, Yantai	Specialization Group on Design Automation of Digital Systems	He Chengwu [0149 2052 2976] East China Computing Institute	100 persons 5 days	
9. Computer Education and Personnel Training Conference	September 1984, Hefei Industrial University	Education Specialization Group, Training Specialization Group	Research Institute of Hefei Industrial University, Beijing Univ. 2nd Branch School	200 persons	

<u>Name of Activity</u>	<u>Time &amp; Place</u>	<u>Host Units</u>	<u>Cooperating Units</u>	<u>Scale</u>	<u>Notes</u>
10. Software Engineering Conference	Fourth Quarter, 1984	Software Branch	Zhu Sanyuan [2512 0005 0337] Shanghai Computing Institute	150 persons	Precise date will be set in mid-year when papers have been reviewed and preparations have been made.
11. Meeting of the Editorial Committee of Science Books Popularization	First Quarter 1984, Beijing	Popularization Committee		25 persons 3 days	
12. Second Exchange Meeting on Configuration Technology	October 1984, Changsha	Configuration Technology Specialization Group	National Defense University of S&T, Research Institute	100 persons 7 days	
13. Industrial Control-Computer Conference	Third Quarter 1984, Chongqing	Chongqing Institute of Automation		100 persons 5 days	Preparation group already set up
14. Computer Management System (Ministry and Commission 1 Level) Academic Exchange and Proposal Forum	1984, Beijing	Ministry of Electronics Industry, Bureau 6		70-80 persons	To accelerate bureau and ministry network applications work and to promote ministry, bureau and enterprise automated management.
15. Fourth Micro-computer Technology Conference	Second Quarter 1984, Wuhan	Microcomputer Branch	Wuhan Institute 709		On the basis of present situation in terms of articles, it has been proposed to delay the meeting requests for articles have already been issued.
16. Second China Computer Diagnosis and Treatment Conference	March 1984, Wuhan	Shanghai Computer Institute and the Hubei Academy of Chinese Medicine	Central China Industrial College, Department of Computers	100 persons 6 days	105 articles have been received, and the review committee issued abstracts of the articles on 9 Dec 1983.

<u>Name of Activity</u>	<u>Time &amp; Place</u>	<u>Host Unit</u>	<u>Cooperating Unit</u>	<u>Scale</u>	<u>Notes</u>
17. Conference on Data Base System Technology	July 1984 Tianjin	Be Shikuan (5446 1387 3031) Software Branch			
18. Second Conference on Nonlinear Applications	Third Quarter, 1984	Shu Fuzong (2612 1331 1073) Chinese Academy of Sciences, Chengdu Inst. of Computers		100 persons 5 days	
19. Second Conference on Application of Microprocessors in Peripheral Systems	October 1984, Nanjing	Peripheral Equipment Group	Plant 734, Institute 52	100 persons 5 days	May be postponed until end of 1984 or early 1985, will deal with application of microprocessors in printers.
20. Conference on Triple April and Multiple Value Logic	April 1984, Guangzhou		South China Industrial College	13 persons 5 days	
21. Exchange Conference on Artificial Intelligence Technology	1984	Artificial Intelligence Study Group		100 persons 5 days	
22. Colloquium on Information Storage Technology	Late June 1984, Dalian	Information Storage Technology Study Group	Wei Baslin (2614 1405 2631) Shenyang Institute of Computers		To investigate the present state of information storage technology in China and abroad, discuss future directions
23. Colloquium on Local Networking of Microcomputers	August 1984, Chengdu	Microcomputer Branch, System Structure Group, Configuration Group	Shanghai Institute of Optics, Qinghua University	100 persons 5 days	
24. Colloquium on Computer Operations (User) Management		Maintenance Specialization Study Group			Self-supporting

<u>Name of Activity</u>	<u>Time &amp; Place</u>	<u>Host Units</u>	<u>Cooperating Units</u>	<u>Scale</u>	<u>Notes</u>
25. Conference on Disk Use and Maintenance Management Experience		Maintenance Specialization Study Group			Self-supporting
26. First National Conference on Computer Technical Training	April 1984, Suzhou	Technical Training Specialization Group	Suzhou Computer Plant	100 persons	
27. Colloquium on Computer System Performance Evaluation	Fourth Quarter, 1984	System Configuration Study Group	Su Dongzhuang [5685 2639 5445] Northwest Telecommunications Engineering College, Computer Dept.	40 persons 4 days	Place yet to be determined
28. Exhibit of Achievements in Microcomputer Applications	October 1984, Xi'an	Microcomputer Branch, Shaanxi Science Committee	Shaanxi Microcomputer Branch	300 persons 10-15 days	exhibit Shanghai is also planning an exhibit, time to be determined
29. Exhibit of New Microcomputer Products and Technology	Second Quarter 1984, Guangzhou	Microcomputer Branch	Guangdong Science Committee, South China Normal University, Microcomputer Institute	300 persons 10-15 days	
30. Network Technical Training Class	Second Quarter 1984, Taiyuan				
31. Training Group will hold several training classes in 1984					Plans to be announced



AUTHOR: BODDINGTON, T.  
FENG Changgen [7458 7022 2704]  
GRAY, P.

ORG: BODDINGTON and GRAY both of the School of Chemistry, University of Leeds, Leeds, U.K.

TITLE: "Thermal Explosion and Times to Ignition in Systems with Distributed Temperatures. I. Reactant Consumption Ignored"

SOURCE: Beijing BINGGONG XUEBAO [ACTA ARMAMENTARII] in Chinese No 2, May 84 pp 1-14

TEXT OF ENGLISH ABSTRACT: This paper studies the time dependence of spatially distributed temperature profiles in an exothermically reacting system under marginally supercritical conditions (reactant consumption ignored). The earlier results for uniform-temperature systems ( $\beta = 0$ ) have been extended and the quantitative mathematical formula for non-uniform temperature systems ( $0 < \beta \leq \infty$ ),  $t/t_{ad} = M/(\delta/\delta_0 - 1)^{1/2}$ , is derived. The proportionality constant  $M$  is provided and its variation with geometry and the Biot number ( $\beta$ ) is discussed. The geometry studies are the infinite slab, infinite cylinder and sphere and the reaction rate law discussed is Arrhenius' law; however, our results are readily applicable to further geometry studies and rate laws. Our results are also compared with an exact (numerical) solution: the agreement close to criticality is very good and, surprisingly, remains fair up to  $\delta \approx 2$  cr.

AUTHOR: YANG Daren [2799 1129 0117]

ORG: None

TITLE: "The Design of the K $\theta$  Lens Used on a Laser Scanning for Automatic Inspection of Object Size"

SOURCE: Beijing BONGGONG XUEBAO [ACTA ARMAMENTARII] in Chinese No 2, May 84 pp 15-22

TEXT OF ENGLISH ABSTRACT: This paper describes the basic concept, working principle and design process of the K $\theta$  lens to be used on a laser beam scanning system for automatic inspection of object size. Under proper conditions of the pupil and wavelength, the K $\theta$  lens can be optically designed with simple construction, at low cost and satisfactory for practical usage. With an accuracy of  $\pm 3 \mu\text{m}$ , the measuring region stretches to  $47 \times 1000 \text{ mm}^2$ .

AUTHOR: ZHANG Hongming [1728 7703 7686]  
YUN Guobao [0061 0948 1405]  
XU Chengdong [1776 2052 2639]  
et al.

ORG: None

TITLE: "The Crystal and Molecular Structure of 1,3,5-Trinitro-1,3,5-Triazopetane"

SOURCE: Beijing BINGGONG XUEBAO [ACTA ARMAMENTARII] in Chinese No 2, May 84  
pp 43-48

TEXT OF ENGLISH ABSTRACT: The crystal structure of 1,3,5-Trinitro-1,3,5-Triazopetane ( $C_2H_6O_6N_6$ ) has been determined by the X-ray single-crystal diffraction technique. The space group is  $P_{6CN}$ , with  $a = 8.674 (3) \text{ \AA}$ ,  $b = 6.346 (2) \text{ \AA}$ ,  $c = 13.420 (4) \text{ \AA}$ ,  $Z = 4$ . The crystal structure was solved by the direct method, and the hydrogen atom positions were obtained by means of the difference Fourier synthesis technique. The final  $R = 0.048$  for 904 unique observed reflections after least-squares refinement. The shape of the molecule of the compound is a chain configuration having diad axis. The N-N, N-C bond lengths are shorter than those in a normal molecule, and some short intermolecular and intramolecular distances exist. The electronic charge distribution in the molecule is also calculated using the CNDO/2 method.

9717

CSO: 4009/111

AUTHOR: LIU Jiamo [0491 0857 6206]

ORG: Southwestern Institute of Physics

TITLE: "Design of Preliminary Testing of a Particle Injector Beam Transport System"

SOURCE: Chongqing HEJUBIAN YU DENG LIZITI WULI [NUCLEAR FUSION AND PLASMA PHYSICS] in Chinese Vol 3, No 3, 15 Sep 83, pp 180-187

ABSTRACT: First, the beam transport system of a particle injector was described in detail and a photograph of the particle injector was shown. Then, the design considerations and equations for the transport system were given. In order to choose the optimum aperture, the envelop equations were introduced to directly find a solution matching the beam parameters. It was followed by a description of the computation method of the envelop equation. Finally, the tolerance of the system was discussed. The system just underwent preliminary testing. Using a 100 keV arc source with a 40 mA maximum  $H_2^+$  beam, it was already capable of passing a 12 mA  $H_2^+$  beam through a  $4 \times 6 \text{ cm}^2$  limiting aperture to hit a  $\phi 7 \text{ cm}$  target in the capture chamber 175 cm behind the aperture. The effective brightness of the injecting beam was  $4.5 \times 10^6$ , which is comparable to that of  $4.9 \times 10^6$  for OGRA - I.

The manuscript was received on 9 Aug 81. The author wished to acknowledge that the system was fabricated by the Xianfeng Electrical Plant in Shanghai and system testing was performed with the cooperation of the comrades in the ionic source group. He wished to express his gratitude to the relevant people.

12553

CSO: 4009/89

AUTHOR: HUANG Jinhua [7806 6930 5478]

ORG: Southwestern Institute of Physics

TITLE: "Importance of Fusion Neutron to Reactor First Wall"

SOURCE: Chongqing HEJUBIAN YU DENGGLIZITI WULI [NUCLEAR FUSION AND PLASMA PHYSICS] in Chinese Vol 3, No 3, 15 Sep 83, pp 129-134

ABSTRACT: Due to the high neutron flux through the first wall, radiation damage and heat accumulation became one of the problems of most concern in studying the design of a fusion reactor. In a spherical geometry, corresponding to an inertially confined reactor, neutron flux could not be accurately calculated by the  $S_n$  method using a point source because of the extreme anisotropy of the uncollided fusion neutron. Heating and radiation damage thus estimated were found to be excessively high. The simplest way was to treat it as a shell source located on the inner surface of the first wall and  $S_{16}$  could provide results with sufficient accuracy. For a cylindrical geometry such as in the case of a magnetically confined fusion reactor, it was possible to estimate the neutron flux with a point source because the anisotropy of the fusion neutron was much weaker. Wide discrepancies were discovered in calculating the power density of the first wall for a specific reactor design. It was identified as due to the difference in the Kerma factor of the iron neutron in various data banks. This effect was further confirmed by the information supplied by Mr Robert Seamon of LANL in Jun 82. Since the Kerma factor is important in determining the behavior of the first wall in the high energy region, it is obvious that further investigation is needed.

The work was completed in November 82 in the Nuclear Engineering Department at University of Wisconsin. The author wished to thank Professor Maynard for the beneficial discussion, Mr Robert Seamon for providing the information, and Comrade Li Shupeil [2621 3359 8951] for translating the English manuscript.

12553

CSO: 4009/89

AUTHOR: DAI Chuanzeng [2071 0278 2582]

ORG: Institute of Atomic Energy, Chinese Academy of Sciences

TITLE: "Nuclear Safety of PWR System"

SOURCE: Beijing HE KEXUE YU GONGCHENG [CHINESE JOURNAL OF NUCLEAR SCIENCE AND ENGINEERING] in Chinese Vol 4 No 2, Jun 84 pp 97-104

TEXT OF ENGLISH ABSTRACT: The status of nuclear safety of the PWR system is reviewed. The "defense in depth" concept and intensive research and development have made the nuclear power industry one of the safest industries in the modern world.

Both mechanistic and probabilistic methodology have been shown to be powerful analytical tools for foreseeing the accident sequence and its probability of occurrence. They are used in further improving the safety of reactor systems.

Important safety measures for preventing severe core damage of the PWR and ensuing serious consequences are discussed for typical cases.

Finally, recent efforts toward further improvements in safety are reviewed.



AUTHOR: LING Shi [0407 1395]

ORG: Shanghai Institute of Nuclear Research, Chinese Academy of Sciences

TITLE: "The Critical Assembly of the Shanghai Institute of Nuclear Research Division of Reactor Technology"

SOURCE: Beijing HE KEXUE YU GONGCHENG [CHINESE JOURNAL OF NUCLEAR SCIENCE AND ENGINEERING] in Chinese Vol 4 No 2, Jun 84 pp 111-116

TEXT OF ENGLISH ABSTRACT: A general description of the slightly enriched uranium fueled and light water moderated critical assembly of the Shanghai Institute of Nuclear Research, Chinese Academy of Sciences, is given. Some experimental works carried out with it are also briefly presented.

The main task of this facility is the research for PWR power plants. The core design is to simulate the clustered fuel assembly structure without a box and the whole lattice arrangement of PWR's. It is also possible to simulate the chemical control of the reactivity by putting soluble boron poison into the light water moderator and reflector. In addition, the following advantages are available: fairly good flexibility of the core structure for the application of pluggable fuel assemblies and improved physical conditions for the application of a pneumatic transportation system of the neutron source.

Most results of the experiments are provided for the designers of the PWR for their reference.

AUTHOR: ZHANG Senru [1728 2773 1172]

ORG: Southwest Institute of Nuclear Reactor Engineering

TITLE: "Some Special Safety Problems of the High Pressurized Intermediate Water Loop of a Nuclear Heat Power Plant"

SOURCE: Beijing HE KEXUE YU GONGCHENG [CHINESE JOURNAL OF NUCLEAR SCIENCE AND ENGINEERING] in Chinese Vol 4 No 2, Jun 84 pp 117-122

TEXT OF ENGLISH ABSTRACT: A nuclear heat power plant adopts a three-loop system power installation. This paper presents a preliminary analysis of some possible accidents associated with the high pressurized intermediate water loop scheme, namely, boric acid dilution, second loop pressure decrease out of the external power supply, etc. The installation not only supplies the steam safely, but also can assure safety during these accidents.

AUTHOR: WANG Jiafeng [3769 1367 0023]

ORG: Southwest Institute of Nuclear Reactor Engineering

TITLE: "Natural Convection in the HFETR Core"

SOURCE: Beijing HE KEXUE YU GONGCHENG [CHINESE JOURNAL OF NUCLEAR SCIENCE AND ENGINEERING] in Chinese Vol 4 No 2, Jun 84 pp 123-128, 104

TEXT OF ENGLISH ABSTRACT: A natural convection experiment has been performed at the beginning of the first cycle in the HFETR. This paper analyzes theoretically the natural convection heat transfer in the HFETR core. For the case of non-uniform wall temperature, non-uniform heat flow and steady and fully developed laminar flow in the multi-annular type fuel element, the heat transfer coefficient for natural convection is well represented by the equation:  $Nu_f = 1.05(RePr)_f^{0.25}$ .

AUTHOR: MAO Zongqiang [3029 1350 1730]  
SUN Shiren [1327 0013 0088]  
MA Xuquan [7456 2700 3123]  
ZHANG Chengqun [1728 2052 5028]

ORG: All of Qinghua University

TITLE: "Influence of Pulse on Mass Transformation in Extraction Column  
(30 percent TBP-Kerosene/ $\text{HNO}_3$ - $\text{UO}_2(\text{NO}_3)_2$  System)"

SOURCE: Beijing HE KEXUE YU GONGCHENG [CHINESE JOURNAL OF NUCLEAR SCIENCE  
AND ENGINEERING] in Chinese Vol 4 No 2, Jun 84 pp 129-135

TEXT OF ENGLISH ABSTRACT: A pulsed column is a kind of important extraction equipment. At present, studies of mass transfer in extraction columns require consideration of the effect of longitudinal mixing. Some authors have engaged in such studies and a number of calculation methods for the pulsed extraction column have been established.

This paper represents the characteristics of mass transfer for low concentration uranium-nitric acid-water/TBP-kerosene system in an air-pulsed nozzle plate extraction column of a two-inch diameter. Stable concentration profiles under different pulsed conditions were determined by separately sampling each phase from the extraction column. Data obtained were treated by a simple approximation method using a diffusion model. The relation between pulse intensity and true height of the mass transfer unit in which the effect of longitudinal mixing has been deducted is obtained.

AUTHOR: WANG Kuiwu [3769 7608 2976]  
WANG Changyin [3769 7022 7113]  
LIU Mingzhe [0491 2494 0772]  
WANG Enyue [3769 1869 6460]

ORG: All of Southwest Institute of Physics

TITLE: "Progress in Engineering Studies of a Steady-state Superconducting Mirror Machine"

SOURCE: Beijing HE KEXUE YU GONGCHENG [CHINESE JOURNAL OF NUCLEAR SCIENCE AND ENGINEERING] in Chinese Vol 4 No 2, Jun 84 pp 143-152

TEXT OF ENGLISH ABSTRACT: A steady-state superconducting mirror machine is outlined. The results obtained during 1977-1982 are given for separate adjustments on its vacuum system, electrosystem, ion injector, physical alignment of particle beam, carbon arc neutralizer and cryogenic superconducting system of the magnetic trap, and for whole system adjustment.

After adjustments of separate parts and the whole system, the engineering goal of this machine, as the first step, has been achieved: the energy of the ion source is 100 keV; the total ion current is 0.7 A, the current of  $H_2^+$  is 120 mA and 26 mA at the access of magnetic lenses for focus and at the trap center respectively; the equivalent current of a neutral beam at the trap center is 7.2 mA; the operation of superconducting magnets has lasted for 9 hours at 4.2 K, and 21.7 kGs of the magnetic field at the trap center has been obtained when the magnet current is 133 A; and by using cryopumps, the background vacuum in the magnetic trap is  $4.8 \times 10^{-9}$  Torr and  $3.5 \times 10^{-8}$  Torr with beam injection.

9717

CSO: 4009/121

END

**END OF**

**FICHE**

**DATE FILMED**

19 Oct 1984